INVESTIGATION OF HOMOTYPIC PYD AND CARD DOMAIN INTERACTIONS IN ASC SPECK ASSEMBLY

by

Hasan Ozan Otaş

B.S., Molecular Biology and Genetics, Izmir Institute of Technology, 2016

Submitted to the Institute for Graduate Studies in
Science and Engineering in partial fulfillment of
the requirements for the degree of
Master of Science

Graduate Program in Molecular Biology and Genetics
Boğaziçi University

2019

ACKNOWLEDGEMENTS

Firstly, I'd like to offer my gratitude to Prof. Nesrin Özören for her supports and contributions to my thesis work. In the lab, I have tasted scientific freedom from start to end. Thanks to her contributions, I significantly improved my scientific thinking skills. I would also like to thank Prof. İ. Halil Kavaklı and Assoc. Prof. Umut Şahin for their efforts on evaluation of this thesis.

I want to thank Prof. Amitav Sanyal for allowing me to use their spectrofluorometer each time that I need in my experimental setup. I thank to Assoc. Prof. Stefan H. Fuss for his help in confocal microscopy training. I'd like to thank past and present Apoptosis and Cancer Immunology Laboratory (AKİL) members especially Aylin Alkan, B.Sc., Davod Khalafkhany, M.Sc., Gizem Olay Artık, B.Sc., Hafize Özen Kaya, M.Sc., İlke Süder, M.Sc. and Efe Elbeyli, M.Sc. They always helped me with their friendship and knowledge. I also thank to SUMO Lab for supporting me when I needed any chemicals or solutions.

I'd like to thank Hulusi Onur Kuzucu for all his help in this project. I thank to Aylin Alkan, for her supports not only in lab, but also in my life. I want to thank Duran Emre Kanacı and Yusuf Tunahan Abacı for their support and for being both my kind lab mates and roommates. I'd like to thank Rumeysa Ermiş for her contributions.

Last but not least, I'd like to express my special thanks to my beloved parents; Serpil Otaş and Osman Otaş, my sister and her family; Feride Gülşah Kuzucuk, Zeynep Derin Kuzucuk and Şerafettin Kuzucuk for all of their supports for me throughout my life and scientific career.

We stand in the presence of riddles, but not without the hope of solving them. And riddles with the hope of solutions- what more can a scientist desire?

Hans Spemann (Nobel Prize, 1935)

ABSTRACT

INVESTIGATION OF HOMOTYPIC PYD AND CARD DOMAIN INTERACTIONS IN ASC SPECK ASSEMBLY

Apoptosis-associated speck-like protein containing a CARD (ASC) is a 22 kDa protein containing conserved PYD and CARD domains that belong to death-fold superfamily. Homotypic interactions between the domains occur via providing at least three certain surfaces of contact (Type I, II and III). ASC has an adaptor role between receptor and effector proteins in the inflammation process having the ability to form a supramolecular globular complex called ASC speck through PYD and CARD homotypic interactions. When expressed in truncated form as PYD and CARD separately, these domains form filamentous structures. Apparently, these fibers compact onto each other during the wild type ASC polymerization. In this study, our aim was to elucidate the importance of specific locations on PYD-PYD and CARD-CARD interaction surfaces during the polymerization process. Effects of 19 single and 22 double mutations were observed introducing them on important residues such as E13A, D48A, Y60A, E130A, Y146A, R150A and M159A to hit one and/or two interaction surfaces at the same time. Effects of the mutations were visualized using fluorescence and confocal microscopy to qualify the change in the level of organization of the phenotype from filamentous to soluble. Next, we analyzed rate of homooligomerizations in mutant sets using FRET technique to quantify the interaction efficiencies in presence of disruptive mutations. Our results showed that PYD mutants, which've been known to disrupt homooligomerization, are able to provide multimeric filamentous structures when expressed together with their wild type counterparts although CARD mutants have less tolerance to mutations in the interaction surfaces. We identified certain mutations that increase, decrease or block FRET signal. Our study provides better explanation and new insights about the oligomerization dynamics of the inflammasome complex.

ÖZET

ASC ZERRESİ OLUŞUMUNDA YER ALAN PYRIN VE CARD BÖLGELERİNİN HOMOTİPİK ETKİLEŞİMLERİNİN İNCELENMESİ

Apoptoz-ilişkili zerrecik-benzeri CARD içeren protein (ASC), ölüm bölgesi ailesine ait korunmuş PYD ve CARD alanlarını içeren 22 kDa büyüklüğünde bir proteindir. Alanlar arasındaki homotipik etkileşimler, en az üç belirli temas yüzeyinin (Tip I, II ve III) etkileşimiyle meydana gelir. PYD ve CARD homotipik etkileşimleri yoluyla ASC zerreciği oluşur. ASC, enflamasyon sürecinde reseptör ve efektörler arasında adaptör role sahiptir. Kesilmiş olarak PYD ve CARD şeklinde ayrı ayrı ifade edildiğinde, bu alanlar filamentli yapılar oluşturur. Bu filamentler, yabanıl tip ASC polimerizasyonu sırasında birbirlerine yakınlaşmaktadır. Bu çalışmada amacımız, polimerizasyon sırasında önemli noktaların PYD-PYD ve CARD-CARD etkileşim yüzeyleri üzerindeki etkilerini ortaya koymaktır. 19 tekli, 22 ikili mutasyonun, E13A, D48A, Y60A, E130A, Y146A, R150A ve M159A gibi önemli noktalara tanıtılarak, aynı anda bir veya iki etkileşim yüzeyinin zarar görmesinin etkileri gözlemlendi. Mutasyonların etkileşim fenotipinde meydana getirdiği etkiler, organizasyon seviyesindeki değişikliklerin floresan ve konfokal mikroskopi kullanılarak gözlemlenmesi ile değerlendirildi. Yıkıcı mutasyonların varlığında etkileşim oranlarındaki değişimleri ölçmek için, mutant setler FRET tekniği ile analiz edildi ve homooligomerizasyon miktarlarındaki değişiklikler hesaplandı. Sonuçlarımız, CARD bölgesinin, etkileşim yüzeylerindeki mutasyonlara daha az tolerans göstermesine rağmen, homooligomerizasyonu bozduğu bilinen PYD mutantlarının, yabanıl tipteki varyantlarıyla birlikte ekspres edildiğinde multimerik filamentli yapılara katıldığını gösterdi. FRET sinyalini artıran, azaltan veya bloke eden bazı mutasyonlar belirlendi. Çalışmamız, enflamazom kompleksinin oligomerizasyon dinamikleri hakkında daha net açıklamalar ve yeni görüşler sağlamaktadır.

TABLE OF CONTENTS

LIST OF FIGURES

LIST OF TABLES

LIST OF SYMBOLS

A.U.	Arbitrary Units
B_n	Intensity of blank samples at n wavelength.
bp	Base Pairs
°C	Centigrade / Degree Celcius
g	Grams
G	Gravity
I_A	Intensity of acceptor fluorescence at acceptor excitation.
I_D	Intensity of donor fluorescence at donor excitation.
I_F	Intensity of acceptor fluorescence at donor excitation.
I_n	Intensity of sample at n wavelength.
IR_n	Intensity of sample at n wavelength, corrected for total protein.
kDa	Kilodaltons
L	Liters
m	Meters
M	Molars
min(s)	Minutes
ml	Milliliters
mm	Millimeters
mM	Millimolars
mW	Milliwatt
N	Newtons
N_{FRET}	Calculated FRET efficiency
ng	Nanograms
nm	Nanometers
pH	Power of Hydrogen
pmoles	Picomoles
pN	Piconewtons
Q	Protein quantity of sample measured in $\mu g/ml$.

rpm	Revolutions per Minute
sec(s)	Seconds
V	Volts
α	Proportionality constant relating acceptor fluorescence at the acceptor excitation to the donor excitation.
β	Proportionality constant relating donor fluorescence at the acceptor emission to that detected at donor emission.
μg	Micrograms
μl	Microliters
μm	Micrometers
μM	Micromolars

LIST OF ACRONYMS/ABBREVIATIONS

aa	Amino Acid(s)
Abs	Absolute
AFM	Atomic Force Microscopy
AIM2	Absent In Melanoma 2
ALR	AIM2-Like Receptors
ANOVA	ANalysis Of VAriance
apFRET	Acceptor Photobleaching FRET
APS	Ammonium PerSulfate
Ar	Argon
ASC	Apoptosis-associated Speck-like protein containing a CARD
ATP	Adenosine TriPhosphate
bb	Backbone
BCA	BiCinchoninic Acid
BSA	Bovine Serum Albumin
$CaCl_2$	Calcium Chloride
CARD	Caspase Activation and Recruitment Domain
CFP	Cyan Fluorescent Protein
CQ	Chloroquine
DAMP	Danger-Associated Molecular Patterns
DAPI	4′,6-DiAmidino-2-PhenylIndole
DD	Death Domain
ddH_2O	Double Distilled Water
DED	Death Effector Domain
DISC	Death-Inducing Signaling Complex
DMEM	Dulbecco's Modified Eagle Medium
DMSO	DiMethyl SulfOxide
DNA	DeoxyriboNucleic Acid
dsDNA	Double-Stranded DeoxyriboNucleic Acid

E. coli	*Escherichia coli*
EB	Elution Buffer
EDTA	EthyleneDiamineTetraacetic Acid
EF	Endotoxin Free
ECFP	Enhanced CFP
EGFP	Enhanced GFP
EtBr	Ethidium Bromide
EtOH	Ethanol
EYFP	Enhanced YFP
FADD	Fas-Associated Death Domain protein
FBS	Fetal Bovine Serum
FP	Fluorescent Proteins
FRET E	FRET Efficiency
FRET	Förster Resonance Energy Transfer
FWD	Forward
GFP	Green Fluorescent Protein
HBS	HEPES Buffered Saline
HEK	Human Embryonic Kidney
HeNe	Helium Neon
HEPES	4-(2-HydroxyEthyl)-1-PiperazineEthaneSulfonic acid
HI	Heat Inactivated
HP	High Performance
HRP	HorseRadish Peroxidase
IgG	ImmunoGlobulin G
IL	InterLeukin
IPTG	IsoPropyl β-D-1-ThioGalactopyranoside
KCl	Potassium Chloride
KH_2PO_4	Potassium Phosphate Monobasic
LB	Lysogeny Broth
mCh	mCherry
MEM NEAA	Minimum Essential Medium Non-Essential Amino Acids

MHC	Major Histocompatibility Complex
MWCO	Molecular Weight Cut-Off
Na_2HPO_4	Sodium Phosphate Dibasic
NaCl	Sodium Chloride
NF-κB	Nuclear Factor Kappa-light-chain-enhancer of activated B cells
NH_4Cl	Ammonium Chloride
NLR	Nod-Like Receptors
NLRP3	NACHT, LRR and PYD domains-containing Protein 3
NMR	Nuclear Magnetic Resonance
NTA	NitriloTriacetic Acid
OD	Optical Density
OVA	OVAlbumin
PAGE	PolyAcrylamide Gel Electrophoresis
PAMP	Pathogen-Associated Molecular Patterns
PBS	Phosphate Buffered Saline
PCR	Polymerase Chain Reaction
PEG	PolyEthylene Glycol
Pen-Strep	Penicillin-Streptomycin
PIC	Protease Inhibitor Cocktail
PIDD	p53-Induced protein with a Death Domain
PRR	Pattern-Recognition Receptors
PVDF	PolyVinyliDene Fluoride
PYD	PYrin Domain
RAIDD	RIP-Associated ICH-1/CED-3 homologous protein with a Death Domain
REV	Reverse
RFP	Red Fluorescent Protein
RIG-I	Retinoic acid-Inducible Gene I
RIP	Receptor-Interacting Protein
RIPA	RadioImmunoPrecipitation Assay buffer
RLR	RIG-I-Like Receptors

RNA	RiboNucleic Acid
SDM	Site-Directed Mutagenesis
SDS	Sodium Dodecyl Sulfate
seFRET	Sensitized Emission FRET
SMFS	Single-Molecule Force Spectroscopy
SMOC	SupraMolecular Organizing Centers
TAE	Tris-Acetate-EDTA
TBS-T	TBS-Tween
TEMED	TEtraMethylEthyleneDiamine
TGS	Tris-Glycine-SDS
TLR	Toll-Like Receptors
UV	UltraViolet
YFP	Yellow Fluorescent Protein
wt	Wildtype

1. INTRODUCTION

1.1. Immune System

The immune system regulates a huge network of cellular and metabolic processes in organisms which have been evolved in parallel with the immune system. The immune system provides a defense line against all pathogenic microorganisms which are taken up by the human body. Innate immunity and adaptive immunity are two essential components of the immune system [8]. The reaction times and reaction speeds of arms of the immune system differ from each other. Fast responding and simpler form of the system is innate immunity, which provides an early line of defense against the pathogens and found in all multicellular organisms. Physical, chemical and microbiological barriers are key components of the innate immunity. Basophiles, eosinophiles, neutrophiles, monocytes, mast cells and complement system are also major players of innate immunity and provide initial host defense system against pathogens [9]. Second component of the immune system is adaptive immunity which provides more antigen-specific defense and reaction upon activation. The reaction time of adaptive immunity is relatively slower than innate immunity but the specificity of adaptive immunity provides highly specific immune responses via T and B lymphocytes. Adaptive immunity has also the capability to memorize previous immune responses which provides fast activation upon exposure to the same pathogen in the future [10].

1.2. Innate Immunity

Innate immunity is regulated by specific immune cells, which travel to the region upon sensing stimuli coming from pathogens or damages [11]. There are two important factors in initiation and control of the innate immune response. First one is pathogen-associated molecular patterns (PAMPs), which have commonly shared features such as lipopolysaccharides or mannans between most of the types of fungi, bacteria and viruses.

The second factor is danger-associated molecular patterns (DAMPs), which have been formed when host cells undergo stressful conditions, the inner homeostasis is disrupted or imbalance conditions occur in metabolism. These signals are sensed by pattern recognition receptors (PRRs) in cells of myeloid lineage. If the host cells die or are injured, host-derived molecules are secreted to the outside and can be recognized by PRRs. The main players of PRRs are Nod-like receptors (NLRs), Toll-like receptors (TLRs), AIM2-like receptors (ALRs), RIG-I-like receptors (RLRs), C-type lectin receptors (CLRs) and some DNA sensors [12]. Once PRRs are activated through these receptors, a signaling cascade which initiates expression of pro-inflammatory genes is activated then, the process continues with inflammatory caspases, which are further activated proteolytically [3].

1.2.1. Nod-Like Receptors

Nod-like receptors are a large family of sensor proteins which are intracellularly activated and their structures are composed of a central nucleotide-binding oligomerization domain (NOD or NACHT), a variable N-terminal effector domain and C-terminal leucine-rich repeat (LRR) region (Figure 1.1) [13]. There are three structurally conserved regions which NLRs carry; a receptor, an adaptor and a regulator domain. Pyrin domain (PYD), caspase activation and recruitment domain (CARD) and baculovirus inhibitor of apoptosis protein repeat (BIR) domains are components of the effector domain of NLRs. Sensor regions consist of Nod1 and Nod2 have role in sensing PAMPs through which activation of NF-κB pathway occurs. Also, NLRP (Nod-like receptor family with N-terminal PYD) proteins come together in order to form inflammasome to react upon activation and control the secretion of IL-1β and IL-18 [14].

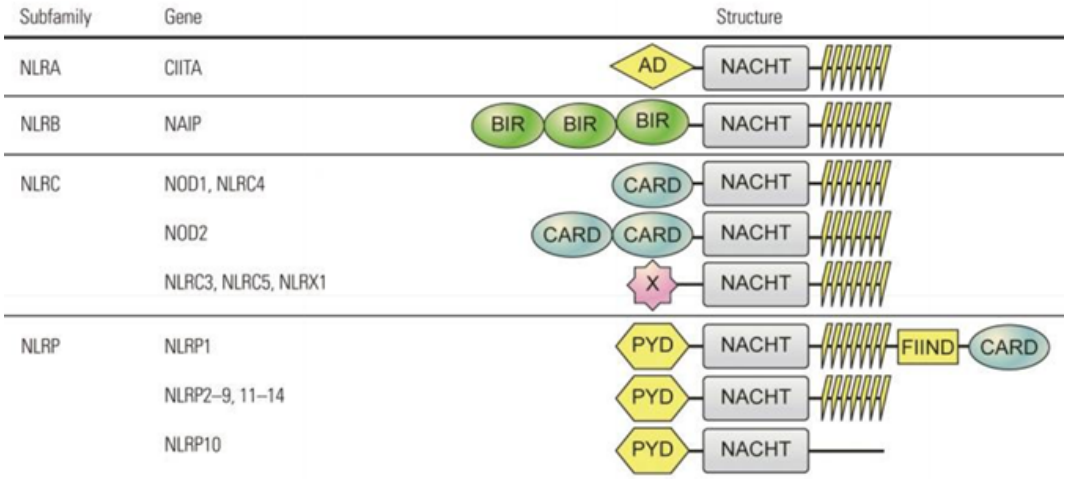

Figure 1.1. Classification of NOD-like receptors. AD = acidic transactivation domain; X = unidentified; (Adapted from Kim, 2016.) [1]

1.2.2. Inflammasomes

The inflammasome is a supramolecular organizing center (SMOC) which is a large assembly of heterogeneous immune signaling molecules formed in order to transduce or amplify the immune signals. The inflammasome is a multimolecular complex that promotes activation of pro-caspase-1 by proteolytic cleavage and it allows pro-inflammatory cytokines IL-1β and IL-18 to be matured and secreted (Figure 1.2). Inflammasome complex has the three types of components and the first one is receptors of NLR or ALR family, second is ASC adapter protein, third component is effector caspase-1 or caspase-5 [15].

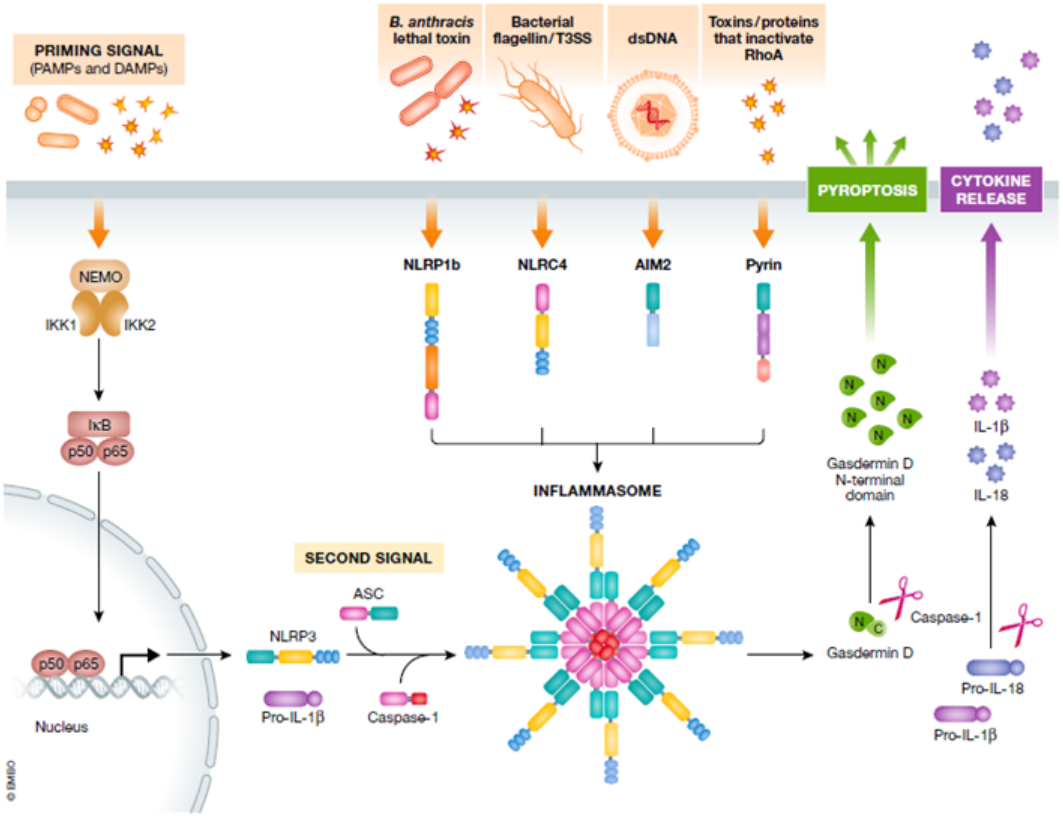

Figure 1.2. Formation and downstream effects of inflammasome complex in which NLRP3 is receptor. (Adapted from Voet, 2019.) [2]

1.2.3. Pyroptosis

Inflammasomes have direct role in pyroptosis which is caspase-1 dependent cell death. Pyroptotic cell death occurs especially in dendritic cells and macrophages when membrane integrity is lost upon stimulation of inflammasome [16]. Pyroptotic cell death mechanism is also defined as clearing of bacterial infections by macrophages. Processing of cytokines is important factor and ASC protein has a key role in formation of the inflammasomes in pyroptotic cell death [17].

1.3. Structure and Formation of Inflammasomes

Intracellular receptors normally stay in resting state when there are no external signals. When they encounter DAMPs and PAMPs which can be extra cellular ATP, lipoproteins, flagellin or dsDNA, conformations of the receptors change which stops auto-inhibition process. When receptor proteins which have PYD domain are activated, PYDs start to form a base which further recruits ASC proteins [15] to the base. Once ASCs are recruited to the base site, PYDs of ASC and receptor homooligomerize to form clusters into long filaments. When ASC proteins form long filaments via the PYD domains, CARDs of ASCs are positioned outward of the complex. Pro-caspase-1 protein has a CARD domain on it and CARDs on pro-caspase-1 starts to interact with CARDs of ASC protein (Figure 1.3). Further recruitment of several pro-caspase-1 proteins allows the enzyme to auto-cleave themselves to cut pro- forms in order to be matured. Then, mature caspase-1 enzymes cleave pro-IL-1β and pro-IL-18 to transform them into the mature forms as IL-1β and IL-18 inducing their secretion [6].

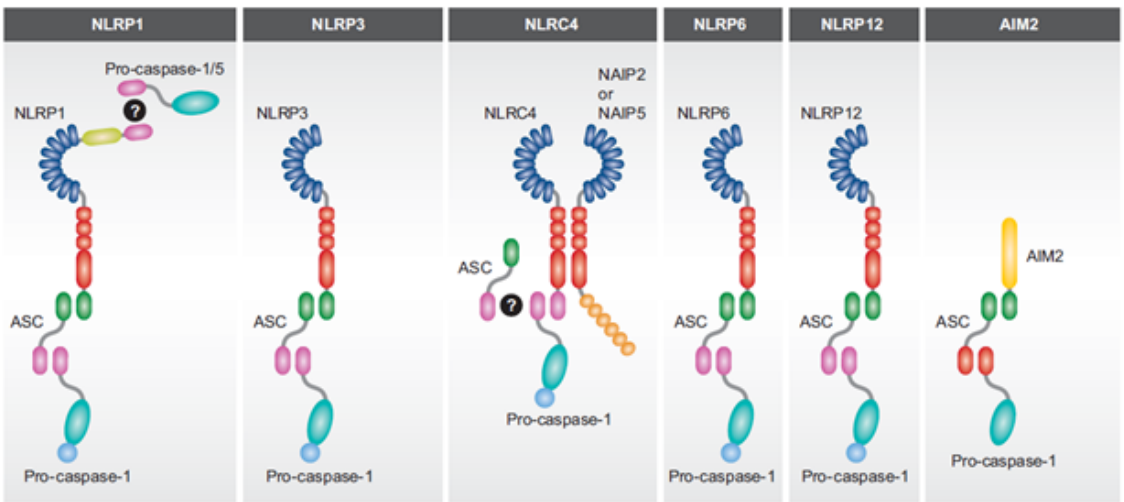

Figure 1.3. Inflammasome assembly. ASC has the adaptor role between receptor and effector proteins. (Adapted from Bauernfeind, 2013.) [3]

1.4. Death-Fold Superfamily

Death-fold superfamily is a group of protein family which consists of DD (Death Domain), DED (Death Effector Domain), PYD (Pyrin Domain) and CARD (Caspase Activation and Recruitment Domain). There are some features shared between members of the family. Firstly, all the members show homotypic interactions between only identical domains and the different members do not interact with each other heterotypically. The members have important roles in signal transduction pathways in immune system especially in the inflammation process and other cell death pathways. Also, they have similar 3D structures having six amphipathic α-helices which are arranged in an anti-parallel α-helical bundle making the structure as globular. Charge distribution and hydrophobicity of some residues differ in these members [4].

1.4.1. Multimeric Formations of Death-Fold Superfamily Proteins

Cell death signals are propagated by death-fold superfamily members via assembly of multimeric structures. Fas-associated death domain protein (FADD) acts an adaptor role in death receptor-induced apoptosis pathway which is triggered by death-inducing signaling complex (DISC). Death Domains (DDs) of FADD protein facilitate the protein to be recruited to the site of DISC formation via homotypic DD interactions (Figure 1.4). Recruitment of DED-only proteins such as pro-caspase-8 is promoted by exposed DEDs. When recruited, activation platform of pro-caspase-8 which is based on DED chain is initiated by interactions of DEDs [18].

p53-induced protein with a death domain (PIDD) is another protein which interacts with receptor-interacting protein-associated ICH-1/CED-3 homologous protein with a death domain (RAIDD). When activated, RAIDD and caspase-2 proteins are recruited to PIDD facilitating the formation of PIDDosome complex. Also, if the oligomeric structure is disrupted, caspase-2 processing may become damaged [19]. Structural features of the death-fold superfamily members provide them to form multimeric complexes in order to be propagated upon death signals.

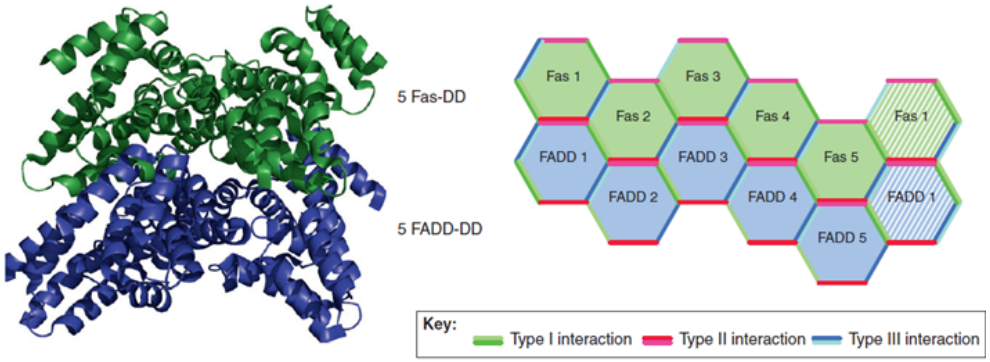

Figure 1.4. Alignment of Fas/FADD-DISC and representation of possible interaction types. (Adapted from Kersse, 2011.) [4]

1.4.2. Molecular Interactions of Death-Fold Superfamily Proteins

Three distinct interaction types mediate the homotypic interaction between death-fold domains providing them to form the higher order multimeric structures.

Type I interaction is occurred in homooligomerization of two domains, first domain with residues on helices 1 and 4 (patch Ia), the other domain with residues on helices 2 and 3 (patch Ib).

Type II interaction is occurred in homooligomerization between domains where residues from helix 4 and the loop between helices 4 and 5 (patch IIa) of a domain interacts with loop between helices 5 and 6 (patch IIb) of another domain.

Type III interaction is occurred via homooligomerization between helix 3 (patch IIIa) of first domain and loops between helices 1 and 2 and between helices 3 and 4 (patch IIIb) of second domain. There are totally six possible interaction surfaces on death-fold domains facilitating them to interact using different interaction modes (Figure 1.5).

The interaction modes are not fully conserved so, they show particular changes between death-fold domains [4].

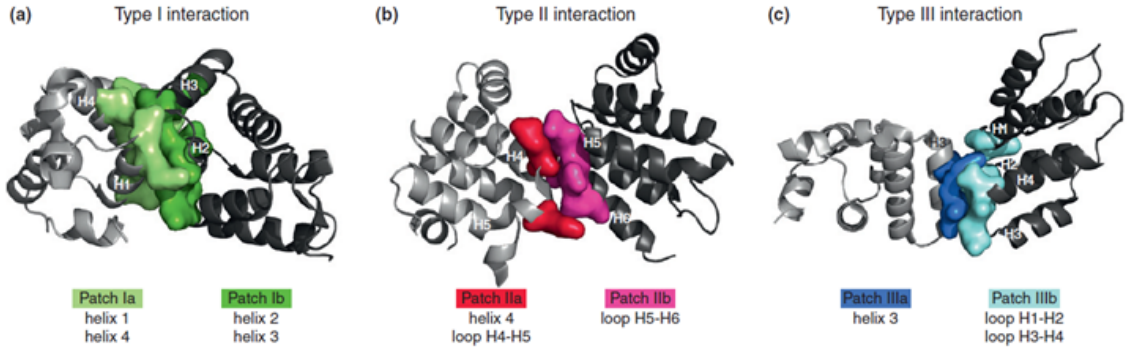

Figure 1.5. (a) Type 1, (b) Type 2 and (c) Type 3 interaction surfaces with two sub-types for each in DDs of PIDD (dark gray) and RAIDD (light gray)(Adapted from Kersse, 2011.) [4]

1.5. Apoptosis-Associated Speck-Like Protein Containing a CARD

Apoptosis-Associated Speck-Like Protein Containing a CARD (ASC) is an adaptor protein which has 195 amino acids and weighed at 22 kDa. ASC has crucial role in formation of inflammasome complex [6]. There are two conserved death-fold superfamily member domains on ASC; PYD and CARD each with six amphipathic α-helices. These two domains are connected with a linker which is 23 aa long, behaves very flexible and unstructured (Figure 1.6) [20]. Both PYD and CARD domains homooligomerize with the homotypic interactions. In the conditions of normal cellular process, ASC stays as monomer and soluble form as non-activated because there is a thermodynamic energy barrier which prevents spontaneous homooligomerization of ASC. On the other hand, if a PYD cluster is formed, it acts as a base for further recruitment and facilitates filament formation lowering the energy barrier and propagation of helical filaments in prion-like manner [21]. Low pH and chaotropic agents mediate ASC to stay soluble in a solution.

On the other hand, ASC initiates long filament formations upon increase in pH or decrease in potassium concentrations [22].

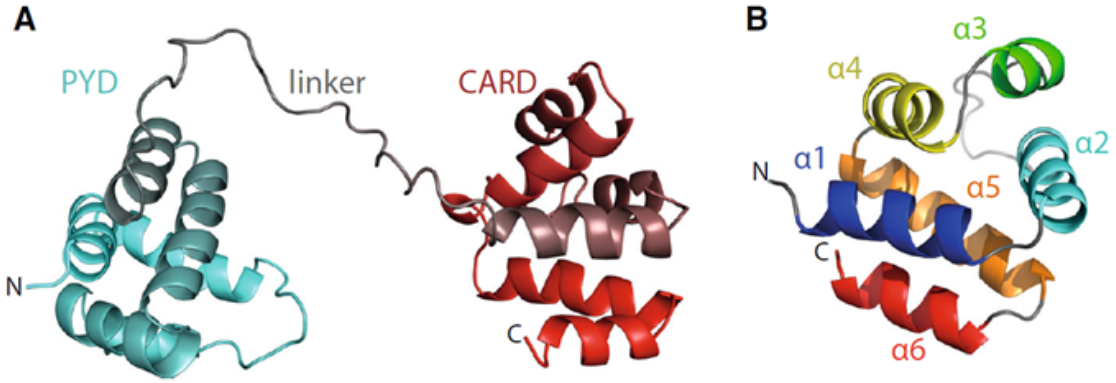

Figure 1.6. Structure of (A) ASC protein (PDB ID: 2KN6 [5]), (B) Typical death-fold superfamily member. (Adapted from Hoss, 2016.) [6]

1.5.1. Structure and Polymerization Dynamics of ASC

PYD of ASC shows highly polar features having positive charged amino acids on helices 2 and 3, negative charged amino acids on helices 1 and 4 [23]. The charge difference between helices 1-4 and 2-3 provides type I interaction surface through which filament formation is initiated. Type I interaction surface has not only been as the largest surface area, but also the most conserved site among three types. Type III surface has been the smallest area while type II has been in intermediate range of the two. All the three types of interaction surfaces are required for a proper homooligomerization for PYD and CARD domains. PYD has some differences in terms of its structure over other death-fold members because type III interaction in the domain is formed via patch IIIa and IIIb in slightly different way [24]. Also, some conformational changes occur in the region of variable loop between helices 2 and 3 [6].

1.5.2. ASC Speck

ASC speck is defined as clustering of multiple filamentous structures together in order to form higher order supra-molecular globular complex [25]. Cross-link between CARD-CARD interactions provides ASC filaments to become compacted.

When ASC-CARDs homooligomerize, a filament compaction occurs which further facilitates pro-caspase-1-CARDs to be recruited onto the oligomerization site [26]. ASC-CARD has more unfolded structure comparing to ASC-PYD in order to prevent too strict homotypic interactions between ASC-CARDs providing pro-caspase-1-CARD to reach and join ASC-CARD filaments [6, 22]. ASC speck has different levels of compaction as in Figure 1.7. In this figure, (A) Confocal microscopy of mCherry-ASC speck formation, (B) High-resolution emission depletion image of ASC speck, (C, D) Compaction levels of ASC speck with NLRP3 inflammasome, (E) ASC-PYD helix in polymerization process and (F) Type I, type II and type III interfaces on the interaction were shown [6].

ASC speck polymerization was stated for taking up to 100 s in HeLa and THP-1 cells which express ASC protein tagged with fluorescent labels [27]. Once the PYD base is initiated, it continues until all ASC monomers come to the region of the speck assembly [21].

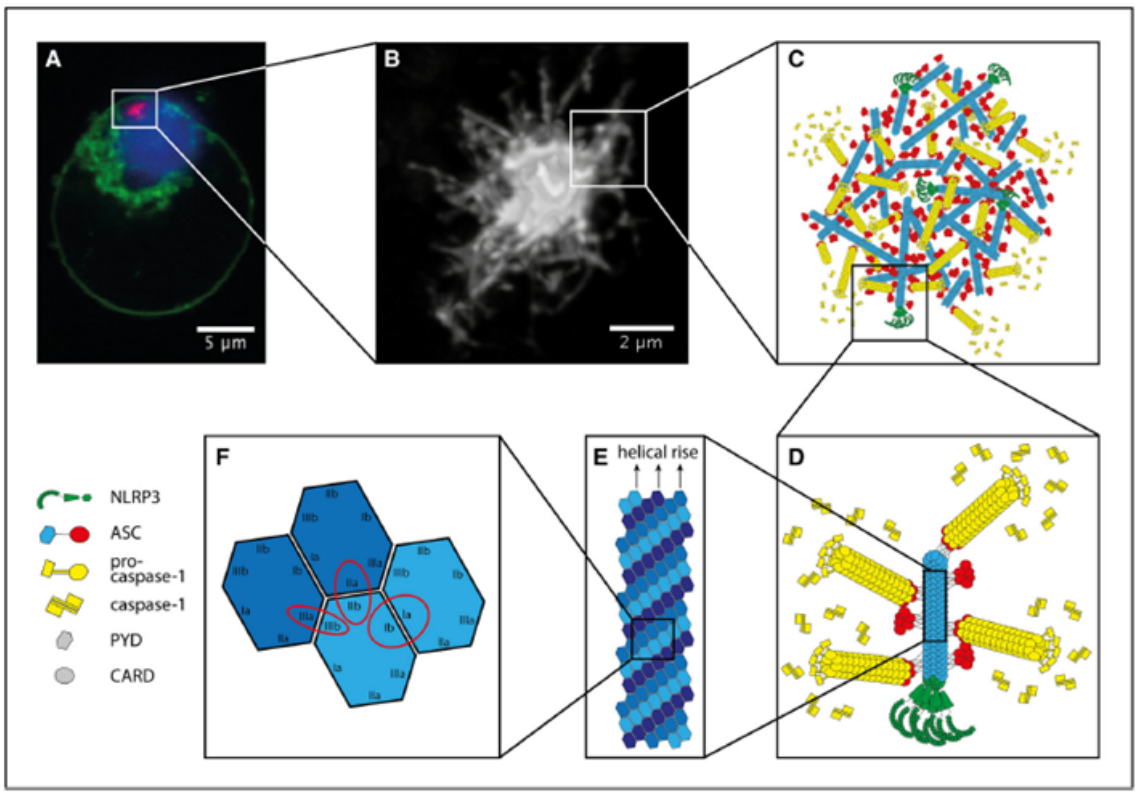

Figure 1.7. Structure of ASC speck and its complexity at different levels. (Adapted from Hoss, 2016.) [6]

1.5.3. Artificial Loading of ASC Specks with Cytosolic Antigens

Formation of ASC speck can cause cells to undergo caspase-1 dependent cell death (pyroptosis). When cells are disrupted and their intracellular contents were released, ASC specks can also be exposed out of cells and can be engulfed by THP-1 cells. The engulfment continues with pinching-off process of ASC specks leading the degradation inside of the cell. ASC specks are shown as useful antigen carriers which increase immune responses as well as carrying the antigens loaded on. Also, it was investigated that, whether ASC can carry H5 and OVA antigens increasing immune responses. Increase in IgG levels were shown upon administration of H5-ASC and OVA-ASC in mice [28, 29].

1.6. Fluorescence Resonance Energy Transfer

Fluorescence (or Förster) Resonance Energy Transfer System (FRET) is a natural phenomenon where emission of excited fluorophore (FP) is transferred to nearby FP whose excitation wavelength is higher than the donor. After excitation of the acceptor FP, secondary emission is given as a FRET signal [30]. Range of the energy transfer is limited to maximum 10 nm so, close proximity is required for FPs to transfer the energy. The energy transfer system is widely used in biophysical studies as well as determination of protein-protein interactions and their interaction efficiencies. [7].

Energy transfer requires two fluorophores each having a substantial overlap between their excitation and emission spectra [31]. The rate of energy transfer given to the acceptor from the donor was calculated as efficiency (FRET E). Fluorescence characteristics of the proteins are important factors in the determination of FRET E. In order to show whether donor and acceptor FPs are proper for energy transfer, acceptor photobleaching FRET (apFRET) is used as a useful method in determination of the proper pairs. Sensitized emission FRET is another method in which interaction amounts can be measured and efficiencies can be calculated in more precise way.

1.6.1. Acceptor Photobleaching FRET

apFRET works as bleaching the acceptor fluorophore which normally quenches the emission of donor FP [32]. apFRET also shows if the FP pair is useful in seFRET studies. When the acceptor FP is photobleached, emission of donor FP is not being quenched so, intensity of donor emission is increased upon photobleaching of acceptor FP. In apFRET, it is assumed that, emission and absorption is destroyed by bleaching the acceptor FP [33].

1.6.2. Sensitized Emission FRET

seFRET is used to measure changes in the efficiency of FRET. One of the current methods used in determination of change in FRET is N_{FRET} where, rates of donor emission at donor excitation, acceptor emission at acceptor excitation and acceptor emission at donor excitation was employed to calculate the change [33]. Correction is done for the calculation for basal expression emission levels of FPs providing N_{FRET} as a useful method [34].

1.6.3. FRET Biosensors

There are two types of FRET biosensors. First type is intramolecular FRET in which acceptor and donor FPs are located on same protein and FRET is occurred due to conformational changes on the molecule. Second type is intermolecular FRET in which acceptor and donor FPs are located on two separate molecules and if they come to a close proximity nearly 10 nm, energy transfer occurs indicating the possible interactions between these two molecules on which FPs are located (Figure 1.8) [7,33].

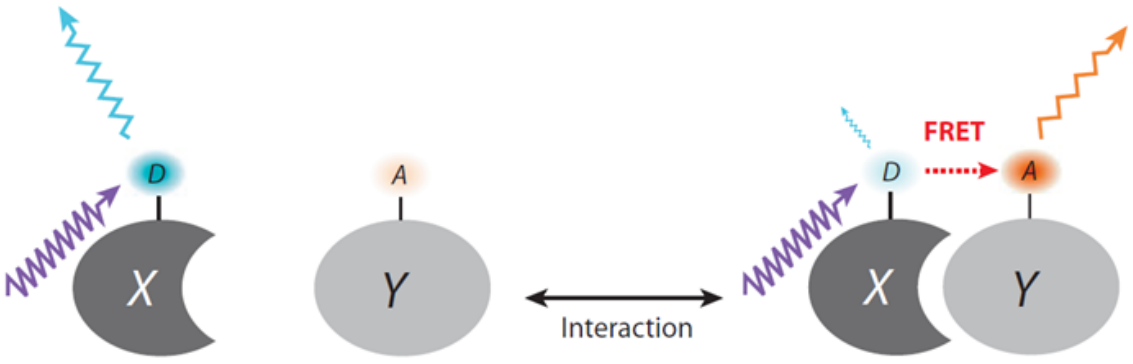

Figure 1.8. Cartoon representation of intermolecular FRET sensor. D, donor; A, acceptor. X and Y are host proteins (Adapted from Miyawaki, 2011.) [7]

2. PURPOSE

Innate immunity acts on first line of defense and has evolutionary conserved processes. Inflammation is one of the major component of innate immune system taking place by activation of intracellular receptors upon danger and pathogen signals. Large complexes such as inflammasomes, pyroptosomes, PIDDosomes and other higher order multimeric assemblies are key factors in cell signaling, cell death and survival pathways. Our research group initially revealed the polymerization dynamics of ASC speck in a pioneering study [20]. In the previous studies in our research group, requirement of three interaction types especially on PYD domains were shown by single mutant analyses. In this thesis, we aimed to analyze importance of these three types of interaction surfaces on homooligomerization process of PYD and CARD domains separately.

In first step, we aimed to analyze effects of single amino acid mutations which are designed to disrupt essential residues on interaction surfaces of PYD and CARD domains.

In second step, we combined single mutations to obtain double amino acid mutations disrupting different interaction types at same time on PYD and CARD domains. For each case, we designed experiments to understand the importance, disruption and compensation abilities of interaction types individually. We also aimed to reveal new interaction modes upon inhibition of interactions between the domains.

For these purposes, we employed both qualification and quantification methods in same time in order to measure and specify the interaction rates for each combinational single/double mutation conditions.

3. MATERIALS

3.1. Cell Lines

Table 3.1. Cell lines used in this study.

	Catalog Number	**Main Source**	**Provider**
HEK293(F)T	R700-07	Invitrogen, USA	Kindly Provided by Prof. Maria Soengas

3.2. Chemicals, Plastics and Glassware

Laboratory chemicals which were used in the study were purchased from either Merck (Germany), Sigma-Aldrich (USA) or AppliChem (Germany). Serological pipettes and cell culture dishes were purchased from either TPP (Switzerland) or VWR (USA). Micropipette tips and tubes were purchased from Axygen (USA). All glassware, tubes and micropipette tips were autoclaved at 121°C for 20 minutes for sterilization prior to use.

3.3. Buffers and Solutions

3.3.1. Cell Culture

FBS was heat inactivated at 56°C for 60 mins in order to disable proteins of complement system in the serum, aliquoted to 50 ml falcon tubes and kept at -20°C for storage. Before the usage, FBS was thawed at 4°C. 500 ml DMEM was completed with 50 ml FBS, 5.5 ml Pen-Strep and 5.5 ml MEM NEAA. Before the usage, complete DMEM was heated to 37°C in a water bath. All steps of the cell culture process were done inside a laminar flow tissue culture hood which was sterilized by UV irradiation after each usage.

Table 3.2. Buffers, solutions and media used in cell culture.

Dulbecco's Modified Eagle Medium (41966-029) MEM Non-Essential Amino Acids (11140-050) Penicillin Streptomycin (Pen-Strep) (15140-122) Fetal Bovine Serum (10270-106)	Gibco, Thermo Fisher Scientific, USA
Complete DMEM	500 ml DMEM 50 ml FBS-HI 5.5 ml Pen-Strep 5.5 ml MEM NEAA
10X PBS (pH 7.4) (Diluted to 1L and filter-sterilized before use)	80 g NaCl 2 g KCl 2.4 g KH_2PO_4 14.4 g Na_2HPO_4 1 L ddH_2O
0.05% Trypsin (pH 8.0) (Filter-sterilized and aliquoted to 50 ml falcon tubes prior to use)	0.154 g EDTA 0.5 g Trypsin 8 g NaCl 0.4 g KCl 0.06 g KH_2PO_4 1 g Glucose 0.048 g Na_2HPO_4 0.35 g $NaHCO_3$ 1 L ddH_2O
DMSO	AppliChem, Germany
Freezing Medium	Complete DMEM 10% DMSO
VectaShield Mounting Medium H-1000	Vector Laboratories, UK

3.3.2. Calcium Phosphate Transfection

Table 3.3. Buffers and solutions used in calcium phosphate transfection. All solutions were filter-sterilized using a 0.22 μm filter prior to use.

2X HBS Buffer (pH 7.0)	50 mM HEPES 280 mM NaCl 1.5 mM Na_2HPO_4
10 mM Chloroquine	0.051 g Chloroquine Diphosphate 10 ml ddH_2O
2 M $CaCl_2$	2,22 g $CaCl_2$ 10 ml ddH_2O

3.3.3. Agarose Gel Electrophoresis

Table 3.4. Buffers and solutions used for agarose gel electrophoresis.

50x Tris-Acetate-EDTA (TAE) Buffer (pH 8.5)	242 g Tris-base 57.1 ml Acetate (Abs. Acetic Acid) 14.62 g EDTA 942.9 ml ddH_2O
Agarose	Merck, Germany
Gel Loading Dye Purple (6X)	New England Biolabs, USA
GeneRuler DNA Ladder Mix	Thermo Fisher Scientific, USA
Ethidium Bromide (EtBr)	Merck, Germany

3.3.4. Bacterial Culture

Liquid and solid culture solutions were autoclaved at 121°C for 15 minutes prior to use. Antibiotics were filter-sterilized using a 0.22 μm filter and stored as 1 ml aliquots at -20°C. Antibiotics were added to LB Agar when the solution is cooled down to 50°C before solidification.

Table 3.5. Solutions used in bacterial culture.

LB Agar Solid Culture (per 1 L ddH_2O)	15 g Agar 5 g NaCl 10 g Tryptone 5 g Yeast Extract
LB Medium Liquid Culture (per 1 L ddH_2O)	5 g NaCl 10 g Tryptone 5 g Yeast Extract
Kanamycin (1000X)	0.5 g Kanamycin Sulfate 10 ml ddH_2O
Chloramphenicol (1000X)	0.34 g Chloramphenicol 10 ml Ethanol (Abs.)

3.3.5. SDS-PAGE, Coomassie Blue Staining and Western Blotting

Table 3.6. Buffers and solutions used in SDS-PAGE, Coomassie Blue staining and Western blotting.

SDS	AppliChem, Germany
Ammonium Persulfate	10% APS (w/v)
Tetramethylethylenediamine	Merck, Germany
30% Acrylamide/Bis-acrylamide	30 g acrylamide 0.8 g bisacrylamide 100 ml ddH_2O

Table 3.6. Solutions used in SDS-PAGE (cont.).

15% Resolving Gel Stock	50 ml 30% Acrylamide 1 ml 10% SDS 20 ml 1.875 M Tris pH 8.8 29 ml ddH_2O
4% Stacking Gel Stock	3.3 ml 30% Acrylamide 250 μl 10% SDS 6.3 ml 0.5 M Tris pH 6.8 15 ml ddH_2O
15% Resolving Gel (for 1.5 mm gel thickness)	4 ml Resolving Gel Stock 40 μl 10% APS 4 μl TEMED
4% Stacking Gel (for 1.5 mm gel thickness)	1 ml Stacking Gel Stock 10 μl 10% APS 1 μl TEMED
10X TGS Running Buffer (Diluted to 1X prior to use)	10 g SDS 30.3 g Tris Base 144.1 g Glycine 1 L ddH_2O
Laemmli Sample Buffer (5X)	500 μl 1.25 M Tris-HCl (pH 6.8) 5.9 ml Glycerol 500 μl 1% Bromophenol Blue 0.5 g SDS 500 μl β-Mercaptoethanol 2.6 ml ddH_2O
Coomassie Blue Staining Solution	0.1% Coomassie Blue 10% Acetic acid 50% Methanol in ddH2O
Coomassie Blue Destaining Solution	10% Acetic acid 40% Methanol in ddH2O

Table 3.6. Solutions used in SDS-PAGE (cont.).

PageRuler Prestained Protein Ladder	Thermo Fisher Scientific, USA
10X TBS (per 1 L ddH_2O)(pH 7.5)	90 gr NaCl 121.14 gr Tris base
Tween-20	Merck, Germany
TBS-Tween	1X TBS 0.1% Tween-20
Blocking Solution	5% BSA in TBS-T
10X Tris-Glycine Buffer (per 0.5 L ddH_2O)	15 gr Tris-Base 72 gr Glycine
ECL Western Blotting Substrate	Thermo Fisher Scientific, USA

3.4. Fine Chemicals

3.4.1. Plasmids

Table 3.7. Plasmids used in this study.

pEGFP-C3	AKİL, Boğaziçi University, Turkey
pEGFP-C3-PYD	AKİL, Boğaziçi University, Turkey
pEGFP-C3-PYD-E13A	AKİL, Boğaziçi University, Turkey
pEGFP-C3-PYD-L25A	AKİL, Boğaziçi University, Turkey
pEGFP-C3-PYD-Y60A	AKİL, Boğaziçi University, Turkey
pEGFP-C3-PYD-E67A	AKİL, Boğaziçi University, Turkey
pEGFP-C3-CARD	AKİL, Boğaziçi University, Turkey
pEGFP-C3-CARD-E130A	AKİL, Boğaziçi University, Turkey
pEGFP-C3-CARD-E152A	AKİL, Boğaziçi University, Turkey
pEGFP-C3-CARD-W169A	AKİL, Boğaziçi University, Turkey
pmCherry-C3-PYD	AKİL, Boğaziçi University, Turkey

Table 3.7. Plasmids used in this study. (cont.)

pmCherry-C3-PYD-S29A	AKİL, Boğaziçi University, Turkey
pmCherry-C3-PYD-T53A	AKİL, Boğaziçi University, Turkey
pmCherry-C3-CARD	AKİL, Boğaziçi University, Turkey
pmCherry-C3-CARD-E130A	AKİL, Boğaziçi University, Turkey
pmCherry-C3-CARD-M159A	AKİL, Boğaziçi University, Turkey
pET30a-CARD	AKİL, Boğaziçi University, Turkey
pET30a-CARD-E130A	AKİL, Boğaziçi University, Turkey
CFP-pro-Caspase-1	AKİL, Boğaziçi University, Turkey

Table 3.8. Plasmids constructed by introducing single aminoacid mutations for this study.

pEGFP-C3-PYD-E67A	pmCherry-C3-PYD-Y60A
pEGFP-C3-CARD-R150A	pmCherry-C3-PYD-E67A
pEGFP-C3-CARD-E152A	pmCherry-C3-PYD-L85A
pEGFP-C3-CARD-K158A	pmCherry-C3-CARD-Y146A
pEGFP-C3-CARD-W169A	pmCherry-C3-CARD-R150A
pEGFP-C3-CARD-R182A	pmCherry-C3-CARD-E152A
pEGFP-C3-CARD-E183A	pmCherry-C3-CARD-P156A
pEGFP-C3-CARD-Q185A	pmCherry-C3-CARD-K158A
pmCherry-C3-PYD-E13A	pmCherry-C3-CARD-W169A
pmCherry-C3-PYD-L25A	pmCherry-C3-CARD-R182A
pmCherry-C3-PYD-D48A	pmCherry-C3-CARD-Q185A

Table 3.9. Plasmids constructed by introducing double aminoacid mutations for this study.

pEGFP-C3-PYD-E13A-S29A	pmCherry-C3-PYD-E13A-S29A
pEGFP-C3-PYD-E13A-D48A	pmCherry-C3-PYD-E13A-D48A
pEGFP-C3-PYD-E13A-Y60A	pmCherry-C3-PYD-E13A-Y60A
pEGFP-C3-PYD-E13A-L85A	pmCherry-C3-PYD-E13A-L85A
pEGFP-C3-PYD-L25A-S29A	pmCherry-C3-PYD-L25A-S29A
pEGFP-C3-PYD-L25A-T53A	pmCherry-C3-PYD-L25A-T53A
pEGFP-C3-PYD-T53A-Y60A	pmCherry-C3-PYD-T53A-Y60A
pEGFP-C3-PYD-E67A-L85A	pmCherry-C3-PYD-E67A-L85A
pEGFP-C3-CARD-E130A-Y146A	pmCherry-C3-CARD-E130A-Y146A
pEGFP-C3-CARD-E130A-R150A	pmCherry-C3-CARD-E130A-R150A
pEGFP-C3-CARD-E130A-E152A	pmCherry-C3-CARD-E130A-E152A
pEGFP-C3-CARD-E130A-P156A	pmCherry-C3-CARD-E130A-P156A
pEGFP-C3-CARD-E130A-K158A	pmCherry-C3-CARD-E130A-K158A
pEGFP-C3-CARD-E130A-M159A	pmCherry-C3-CARD-E130A-M159A
pEGFP-C3-CARD-E130A-W169A	pmCherry-C3-CARD-E130A-W169A
pEGFP-C3-CARD-E130A-R182A	pmCherry-C3-CARD-E130A-R182A
pEGFP-C3-CARD-E130A-Q185A	pmCherry-C3-CARD-E130A-Q185A
pEGFP-C3-CARD-Y146A-E152A	pmCherry-C3-CARD-Y146A-E152A
pEGFP-C3-CARD-R150A-K158A	pmCherry-C3-CARD-R150A-K158A
pEGFP-C3-CARD-E152A-W169A	pmCherry-C3-CARD-E152A-W169A
pEGFP-C3-CARD-E152A-M159A	pmCherry-C3-CARD-E152A-M159A
pEGFP-C3-CARD-W169A-R182A	pmCherry-C3-CARD-W169A-R182A

3.4.2. Primers

Table 3.10. Primers used in this study.

Primer Name	**Sequence**
E13A FWD	GGATGCGCTGGCGAACCTGACCG
E13A REV	CGGTCAGGTTCGCCAGCGCATCC
L25A FWD	CAAGAAGTTCAAGGCGAAGCTGCTGTC
L25A REV	GACAGCAGCTTCGCCTTGAACTTCTTG
S29A FWD	GCTGAAGCTGCTGGCGGTGCCGCTGCGC
S29A REV	GCGCAGCGGCACCGCCAGCAGCTTCAGC
D48A FWD	CTGCTGTCCATGGCCGCCTTGGACCTC
D48A REV	GAGGTCCAAGGCGGCCATGGACAGCAG
T53A FWD	GACGCCTTGGACCTCGCGGACAAGCTGGTCAG
T53A REV	CTGACCAGCTTGTCCGCGAGGTCCAAGGCGTC
Y60A FWD	GCTGGTCAGCTTCGCCCTGGAGACCTACGGC
Y60A REV	GCCGTAGGTCTCCAGGGCGAAGCTGACCAGC
E67A FWD	CCTACGGCGCCGCGCTCACCGCTAAC
E67A REV	GTTAGCGGTGAGCGCGGCGCCGTAGG
L85A FWD	GGCCGGGCAGGCGCAGGCGGCCAC
L85A REV	GTGGCCGCCTGCGCCTGCCCGGCC
E130A FWD	GAGGGTCACAAACGTTGCGTGGCTGCTGGATGCTC
E130A REV	GAGCATCCAGCAGCCACGCAACGTTTGTGACCCTC
Y146A FWD	GACGGATGAGCAGGCCCAGGCAGTGCGGG
Y146A REV	CCCGCACTGCCTGGGCCTGCTCATCCGTC
E152A FWD	CAGTGCGGGCCGCGCCCACCAACC
E152A REV	GGTTGGTGGGCGCGGCCCGCACTG
P156A FWD	GCCGAGCCCACCAACGCAAGCAAGATGCGGAAG
P156A REV	CTTCCGCATCTTGCTTGCGTTGGTGGGCTCGGC
K158A FWD	CCCACCAACCCAAGCGCGATGCGGAAGCTCTTC
K158A REV	GAAGAGCTTCCGCATCGCGCTTGGGTTGGTGGG
M159A FWD	CCACCAACCCAAGCAAGGCGCGGAAGCTCTTCAG

Table 3.10. Primers used in this study. (cont.)

M159A REV	CTGAAGAGCTTCCGCGCCTTGCTTGGGTTGGTGG
W169A FWD	CAGTTTCACACCAGCCGCGAACTGGACCTGCAAGG
W169A REV	CCTTGCAGGTCCAGTTCGCGGCTGGTGTGAAACTG
R182A FWD	CCTCCAGGCCCTAGCGGAGTCCCAGTCC
R182A REV	GGACTGGGACTCCGCTAGGGCCTGGAGG
E183A FWD	CAGGCCCTAAGGGCGTCCCAGTCCTAC
E183A REV	GTAGGACTGGGACGCCCTTAGGGCCTG
Q185A FWD	CCCTAAGGGAGTCCGCGTCCTACCTGGTGG
Q185A REV	CCACCAGGTAGGACGCGGACTCCCTTAGGG
EGFP-CF	AGCACCCAGTCCGCCCTGAGC
mCherry FWD	ACATCAAGTTGGACATCACC

3.4.3. Antibodies

Table 3.11. Antibodies used in this study.

anti-EGFP	Santa Cruz, USA
anti-gamma Tubulin	Santa Cruz, USA

3.5. Kits

Table 3.12. Kits used in this study.

NucleoBond® Xtra Midi EF NucleoSpin® Plasmid NucleoSpin® Gel and PCR Clean-up	Macherey-Nagel, Germany
HisTrap™ HP Column	GE Healthcare, UK
Pierce™ BCA Protein Assay Kit	Thermo Fisher Scientific, USA

3.6. Equipment

Table 3.13. Equipment used in this study.

Agarose Gel Electrophoresis	Thermo Scientific, USA
Agarose Imaging	Gel Doc XR System, Bio Rad, USA
Autoclaves	AMA260BT, Astell Scientific, UK ASB270N, Astell Scientific, UK
Centrifuges	Allegra X-22R, Beckman Coulter, USA himac CT15E, Hitachi Koki, Japan J2-21, Beckman Coulter, USA MiniStar, VWR, USA
Data Acquisition and Control	PXI-based System, National Instruments, USA
Electronic Scales	BJ 4100D, Precisa, Switzerland XT 4200C, Precisa, Switzerland
Freezers	UFR370 SD, Uğur, Turkey 2020 ND, Arçelik, Turkey TS 368, Thermo Fisher Scientific, USA
Incubator	Forma Series II 3111, Thermo Fisher Scientific, USA
Heat Block	VWR, USA
Horizontal Electrophoresis	Mini gel electrophoresis kit, IO Rodeo, USA MP-1015, IBI Scientific, USA

Table 3.13. Equipment used in this study. (cont.)

Laminar Flow Cabinet	Class II A, Tezsan, Turkey Bio II Advance, Telstar, Spain
Magnetic Stirrer	Yellowline MSH Basic, USA
Microscopes	Eclipse TS100, Nikon Corporation, Japan TCS SP8, Leica Microsystems, Germany
Microwave Oven	MD-555 S, Arçelik, Turkey
Oscilloscope	TBS1000B, Tektronix, USA
Peristaltic Pump	LabN1, Baoding Shenchen, China
pH Meter	pH2700, Oakton Instruments, USA
Pipettes	Acura 826 Series, Socorex, Switzerland Axygen Axypet Series, Corning, USA Finnpipette F2, Thermo Fisher Scientific, USA Accurpette, VWR, USA
Pipettors	Greiner-bio one, UK-RatioLab acupetta, Germany
Refrigerators	USS 374 DTKY, Uğur, Turkey S1150A, Vestel, Turkey
Power Supplies	Electrophoresis PSU Kit, IO Rodeo, USA PowerPac Basic, Bio Rad, USA
Thermal Cyclers	C1000, Bio Rad, USA OpenPCR, Chai Biotechnologies, USA
Thermal Shakers	Forma 420, Thermo Fisher Scientific, USA CTS-1, Inovia Teknoloji, Turkey
SDS-PAGE Electrophoresis System	Mini-PROTEAN 4-Cell, BIO-RAD, USA
SDS-PAGE Transfer System	Mini Trans-Blot Electrophoretic Transfer Cell BIO-RAD, USA
Shakers	Orbitron, Infors HT, Switzerland
Sonicator	Sonoplus, Bandelin, Germany
Spectrofluorometer	Cary Eclipse, Agilent Technologies, USA

Table 3.13. Equipment used in this study. (cont.)

Spectrophotometer	NanoDrop ND-100, Thermo Fisher Scientific, USA
Vortex Shaker	Vortexer, Heathrow Scientific, USA
Vertical Electrophoresis	Mini PROTEAN Tetracell, Bio-Rad, USA
Water Baths	1002, GFL, Germany WB 14, Memmert, Germany
Western Blot Visualization	G:BOX Chemi XRQ, Syngene, UK

4. METHODS

4.1. Plasmids

4.1.1. Plasmid DNA Isolation

Instructions of manufacturer were applied during the plasmid DNA isolation. 5 ml of sterile LB medium for mini-scale (miniprep) and 200 ml of sterile LB medium for midi-scale (midiprep) were used in the plasmid DNA isolation process. Before the plasmid isolation, a bacterial stock was obtained by adding 500 μl filter-sterilized glycerol to 500 μl of the bacterial liquid culture. The bacterial stock was kept in a -80°C freezer for long term storage. NucleoSpin® Plasmid (Macherey-Nagel, Germany) kit was used for miniprep, NucleoBond® Xtra Midi EF kit (Macherey-Nagel, Germany) was used for midiprep.

Elution step was completed adding 50 μl elution buffer for miniprep or 1 ml EF-H_2O for midiprep. Concentration and purity of the eluted plasmid was checked using Nanodrop (Thermo Fisher Scientific, USA). Plasmids having the concentration more than 1000 $ng/\mu l$ were diluted to have final concentration of 1000 $ng/\mu l$.

4.1.2. Site-Directed Mutagenesis

Site-Directed Mutagenesis (SDM) was used in order to introduce mutations on plasmids. Protocol of QuikChange II Site-Directed Mutagenesis Kit (Agilent, USA) modified by insights of Xia *et al.* [35] was used during SDM. In the method, forward and reverse oligonucleotide primers which carry the desired mutation were mixed with template plasmids and PCR reaction was done. In the PCR reaction, Q5 High-Fidelity DNA polymerase (New England Biolabs, USA) which can do proof-reading and create nicked circular strands was used. PCR reaction conditions and protocol for SDM are summarized in Table 4.1 and Table 4.2.

Table 4.1. PCR program of Site-Directed Mutagenesis using Q5 DNA Polymerase.

Step #	**Description**	**Temperature (°C)**	**Duration**
1	Initial denaturation	98	30 secs
2	Denaturation	98	10 secs
3	Annealing	T_m-6	30 secs
4	Elongation	72	3 mins
5	Return to step 2 (24x)		
6	Final Elongation	72	2 mins

Table 4.2. PCR mixture for Site-Directed Mutagenesis.

Reagent	**Concentration**	**Volume (μl)**
Q5 Reaction Buffer	1X	10
Q5 High-Fidelity DNA Polymerase	1X	1
Primer Mix	10 $pmoles/\mu l$	4
dNTPs	200 $\mu M/\mu l$	1
DMSO	1X	3
Template	100 $ng/\mu l$	1
ddH_2O		30
Total		50

4.1.2.1. Primer Design for SDM. SDM primers were designed to have length of 21 - 45 base pair, containing desired mutation site at the center of the primer with a minimum GC content of 40%. It was aimed for primers to have at least one G or C bases at both ends in order to anneal stronger. Primers were designed to have at least 10-12 bases in complementary region, the desired mutation in the middle and 10-12 bases after the mutation in 5' to 3' direction. Forward and reverse primers which contain same mutation were designed to have maximum 24 bases for complementarity. Primer dimerization and hairpin formation was prevented as much as possible on the other hand, nature of SDM primers cause self-annealing and hairpin formations in most cases. SDM primer design was represented in Figure 4.1.

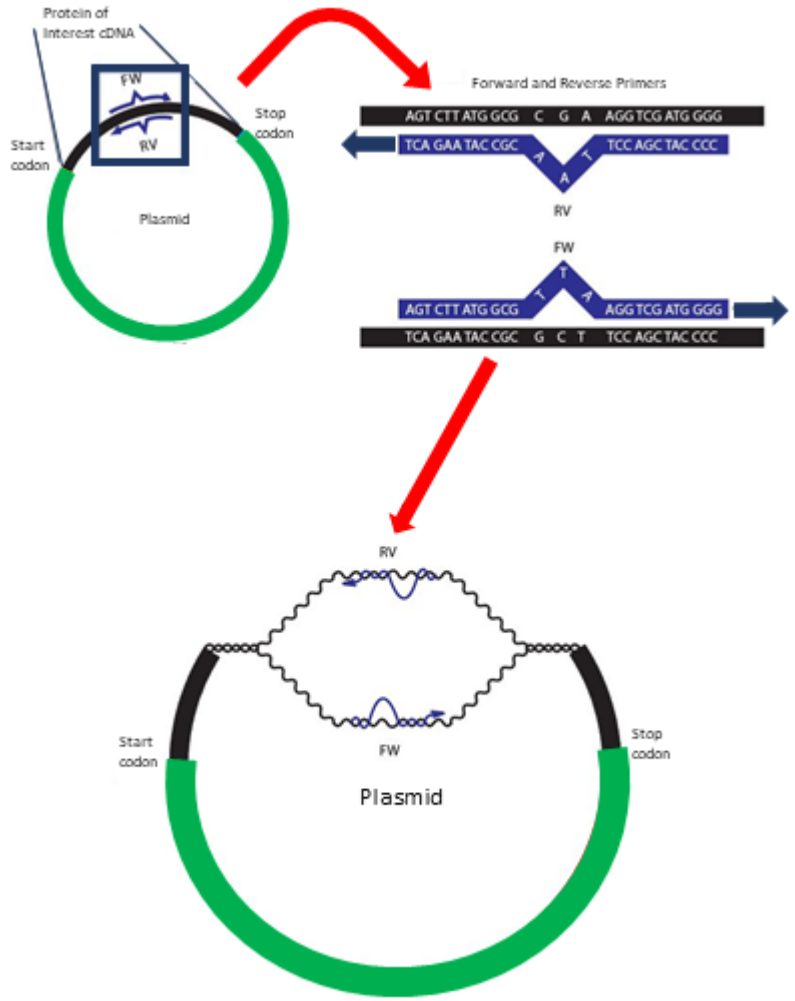

Figure 4.1. Design and annealing principle of SDM forward and reverse primers.

Forward and reverse primers were added 10 $pmoles/\mu l$ for each, respectively. DMSO was used as a GC enhancer for GC rich primers. PCR protocol stated in Table 4.1 was performed achieving totally 24 cycles. Strategy was to provide clear annealing between primers and template DNA preventing primer dimerization as much as possible. Thus, first 10 cycle was done while forward and reverse primers were in separated tubes with half amounts of the total mix for each. After first 10 cycle, the tubes containing forward and reverse primers were combined in one tube and the next 14 cycle was performed while forward and reverse primers are in same tube. After completion of the PCR reaction, the methylated template DNA which has the non-mutant original sequence was digested with Dpn I enzyme.

After the digestion, PCR products were run on agarose gel as described in Section 4.1.4. The products were either extracted from the gel as described in Section 4.1.5 or directly transformed into competent *E. coli* cells as described in Section 4.1.6. After transformation, random three colonies were selected, minipreps of the selected colonies were done and the isolated plasmids were sent to sequencing as described in Section 4.1.7.

4.1.3. Restriction Enzyme Digestion

PCR products of SDM were digested with Dpn I enzyme which cuts DNA at methylated and hemimethylated sites. Dpn I digestion was carried out adding 6 μl CutSmart Buffer (New England Biolabs, USA) and 1 μl Dpn I (New England Biolabs, USA) enzyme into the PCR tube which has 50 μl reaction mixture. Digestion was performed at 37°C for 3 hours, then the mixture was incubated at 80°C for 20 mins in order to inactivate the enzyme to prevent its star activity on plasmids.

4.1.4. Agarose Gel Electrophoresis

PCR products were run on 0.8% agarose gel for either diagnostic purposes or purification of the products using gel extraction protocol was done as described in Section 4.1.5. Agarose gel solution was made by dissolving 400 mg of agarose in 50 ml 1X TAE buffer. The solution was placed in microwave and heated until the agarose is completely dissolved in the buffer without any swimming particles. The solution was swirled in order to provide homogenous heating and dissolving without boiling of the solution. For one of mini-agarose gel, 3 μl of EtBr was added into 50 ml of the dissolved agarose solution in TAE buffer under fume hood. The solution was then poured onto casting tray preventing any air bubble formation. Combs were placed with desired depth of wells and the gel was allowed for cooling and hardening for 20 mins. SDM products either directly from the PCR reaction or agarose gel extraction were firstly mixed with 6X Purple Gel Loading Dye (New England Biolabs, USA) to obtain final dye concentration as 1X then, the mixture was loaded into the wells on the gel.

Power supply was set to 100 V for 70 mins. Electrical current was applied to the gel in the tank which was filled with 1X TAE buffer. The DNA samples were allowed to run until the loading dye reaches to the bottom of the gel. After the run, gels were imaged using UV source.

4.1.5. Agarose Gel Extraction

PCR products which were run on agarose gel were separated by their size that enabled us to differentiate different DNA fragments from each other. Region of the gel at size of the interest was cut using a scalpel on UV source. While the gel is being cut, it is aimed to exclude as much non-specific agarose gel pieces as possible in order to increase the ratio of obtained DNA/gel. NucleoSpin® Gel and PCR Clean-up (Macherey-Nagel, Germany) kit was used to extract desired sized DNA from the gel according to the manufacturer's instructions. Washing steps of the sample were done two times. Elution buffer was preheated to 70°C in order to provide the highest yield from the column.

4.1.6. Transformation of Plasmids into Competent *E. coli* Strains

SDM products either directly from the PCR reaction or agarose gel extraction after the run were transformed into competent Stbl3^{TM} (Invitrogen, USA) *E. coli* strain. 50 μl of frozen Stbl3^{TM} aliquot was taken from -80°C freezer and thawed on ice for 15 mins. 5 μl of plasmid DNA was added to the aliquot and the mixture was incubated on ice for 20 mins. Heat-shock was applied to the bacteria by putting the tube in pre-warmed water bath at 42°C for 45 secs. The tube was removed from the water bath after 45 secs, incubated on ice for 5 mins. 1 ml of sterile LB media was added in the tube and incubated at 37°C for 1 hour while being swirled at 200 rpm. After 1 hour of incubation, the tube was centrifuged at 11000 rpm for 1 min. Supernatant was removed and the pellet was dissolved with 200 μl LB media and spread on LB Agar plates containing necessary antibiotics. After the spread, agar plates were incubated at 37°C for 16 hours. Kanamycin antibiotic was used for selection of positive colonies which were transformed with either pEGFP or pmCherry plasmids.

4.1.7. Sequencing of Plasmids

After the transformation, random 3 colonies were selected and seeded in 5 ml LB liquid media for 16 hours in order to obtain the plasmids using miniprep. Each of the isolated plasmid DNA constructs obtained in this study were checked using Sanger sequencing. Sequence verification was done purchasing the sequencing service from Macrogen Europe in Netherlands. EGFP-CF primer was used to sequence pEGFP plasmids in forward direction and the primer is available as universal primer in the company. pmCherry plasmids were sequenced using primer order named mCherry FWD in order to sequence the plasmids in forward direction.

4.1.8. pEGFP and pmCherry Mutant Constructs

pEGFP-C3-PYD and pEGFP-C3-CARD plasmids were used as template in construction of single and double mutants with EGFP sequence, pmCherry-C3-PYD and pmCherry-C3-CARD plasmids were used as template in construction of single and double mutants with mCherry sequence in SDM reactions. PCR for SDM was done as described in Section 4.1.2 using forward and reverse primers specific for a particular SDM reaction listed in Table 3.10. After the mutagenesis, the mix was transformed into competent *E. coli* cells and plasmids were isolated using miniprep. All new constructs obtained through SDM were sent to sequencing. EGFP-CF and mCherry FWD primers were used to verify the sequences towards forward direction.

4.2. Cell Culture

4.2.1. Maintenance of HEK293FT Cells

HEK293FT cells were cultured using complete DMEM media supplemented with 10% FBS, 1X Pen-Strep and 1X MEM-NEAA.

For the passage of the cells, the culture media was removed by aspiration, 75 cm^2 flask was washed once with 5 ml of 1X PBS then, 2.5 ml 0.05% Trypsin was transferred and the flask was placed in incubator for 5-7 mins for detachment of the cells. When the cells are completely detached, 4-5 ml DMEM was added into the flask by pipetting and the mixture was transferred to sterile 50 ml falcon tube. Centrifugation was applied to tube at 1350 G for 2 mins, the supernatant was removed and the pellet was dissolved with 10-20 ml fresh DMEM. 15 μl of homogenous cell mixture was mixed with 15 μl Trypan blue in a 0.5 ml microcentrifuge tube and homogenization was obtained by pipetting. 10 μl of the mixture was loaded into each wells on the hemocytometer and the cells were counted. The cell mixture was diluted to have final concentration of 1 x 10^6 cells/ml and the cells were seeded to a new 75 cm^2 flask to have 1 x 10^6 cells in 10-15 ml fresh media. To provide homogeneity, the flask was shaken gently in horizontal and vertical directions immediately after the seeding process. The culture flasks were stored in an incubator at 37°C with 5% CO_2 conditions.

4.2.2. Calcium Phosphate Transfection

Calcium phosphate nanoparticles are widely used in gene transfer methods such as transfection of DNA and RNA. Calcium phosphate nanoparticles provide non-toxic environment and calcium provides not only nuclear uptake of transfected DNA via nuclear pore complex but also escape of nanoparticles from lysosomes and endosomes. In the calcium phosphate transfection method, $CaCl_2$ solution is mixed with DNA to be transfected, then HEPES-buffered solution was added resulting in the formation of calcium phosphate and DNA precipitates. After incubation of the mixture, it is transferred onto cells as a dropwise manner [36].

HEK293FT cells which will be transfected were firstly seeded onto 6-cm dishes with 4 ml fresh media. After 24 hours, plasmid DNA was transferred into ddH_2O in a 2 ml sterile centrifuge tube. Then, 2 M $CaCl_2$ solution was added to the tube in drop-wise manner. Lastly, 2X HBS solution was added to the tube by creating bubbles in the mixture via pipetting or dragging the tube on a micro-centrifuge tube rack.

The amounts of solutions mixed for the method was summarized in Table 4.3.

Table 4.3. Ingredients used in calcium phosphate transfection for a 6 cm cell culture dish.

Reagent	**Amount**
ddH_2O	300 μl (up to)
Plasmid DNA	4 μg
2 M $CaCl_2$	30.5 μl
2x HBS	250 μl

After addition of 2X HBS, creation of bubbles is a very important process because the process provides precipitation of calcium phosphate and DNA homogeneously. Mixing the solution through vortexing or shaking will lower the transfection efficiency. Also, dragging the tube onto plastic micro-centrifuge tube rack gives the best efficiency comparing to violent pipetting. After the transfection solution was prepared, the mixture was incubated at room temperature for 7-8 mins. The incubation time affects the transfection efficiency, if time is lowered the precipitate formation will not be large enough, if the incubation time is longer then the precipitates will be larger so, the optimum time is determined as 7-8 mins for the incubation. After the incubation, the transfection solution was directly transferred onto cells in drop-wise manner as dropping the mixture in a spiral path starting from the outermost side of the dish to the middle covering all the cells homogeneously. The dishes were placed in an incubator at 37°C with 5% CO_2.

To increase the transfection efficiency, Chloroquine (CQ) solution was used before the dispersal of the transfection mixture on cells. First, CQ was added onto cells to have 25 μM final concentration in media. Next, the transfection mixture was added. CQ prevents the lysosomal degradation of transfected DNA in cells increasing the effect of transfection in a short time. CQ is a toxic reagent for cells so, the culture medium was completely removed and freshened after 8 hours of CQ addition.

4.2.3. Fluorescence Microscopy

After 24 hours of DNA transfection, the cells were imaged under fluorescent microscope using 5X and 20x objectives per condition. Images were taken once capturing bright field as white balanced, then using B-2A blue excitation filter (Nikon, Japan) and lastly, using G-2A green excitation filter (Nikon, Japan) on manual exposure ranging from 300-600 milliseconds. In the imaging process, standardization was obtained by taking the photos from random regions of dishes and setting similar exposure and gain intervals for the dishes.

4.3. Spectrofluorometry

4.3.1. Collection of Transfected Cells

After 24 hours of transfection, cells in a dish were firstly visualized under fluorescent microscope described in Section 4.2.3 then, same cells were collected. Initially, medium of the dish was removed, cells were washed with 1X PBS and Trypsinized. After the detachment of the cells from the dish, fresh media was added and the mixture was transferred into 50 ml sterile falcon tube. Centrifugation was done applying 1350 G for 2 mins. Supernatant was removed and 4 ml 1X PBS was transferred for washing then, the tube was centrifuged under same conditions. Next, the PBS was removed and the cell pellet was dissolved with 1.5 ml 1X PBS then, the mixture was transferred into a 2 ml sterile micro-centrifuge tube. All the steps after transfection was done under low ambient light conditions because long exposure of the fluorophores to light partly bleaches them and decreases the efficiency for spectrofluorometric measurement. After the collection, samples were immediately brought to the spectrofluorometry device in a box filled with ice packs to ensure cold environment for the cells.

4.3.2. FRET Measurement

Samples in a closed and cold box were brought to spectrofluorometer device. Firstly, samples were transferred into a clean 4 ml quartz cuvette then the cuvette was put in spectrofluorometer by placing the bottom of the cuvette at the same bottom line of laser orifice.

Spectrofluorometric measurements were taken by exciting fluorophores at peak wavelengths of their excitation spectra. Cell samples having EGFP construct was excited at 488 nm and emission spectrum was recorded between 488-700 nm. Cell samples having mCherry construct was excited at 588 nm and emission spectrum was recorded between 588-700 nm. Rate of the sampling was set at 1 per nm. Excitation and emission slits were set as 5 and 10 nm, respectively. Each sample was measured two times first for EGFP condition, second for mCherry condition in this order. After measurement of each samples, the cuvette was emptied, once rinsed with 70% EtOH and then rinsed with ddH_2O. Untransfected samples were used for blank measurements.

4.3.3. Calculation of FRET Efficiency

After the spectrofluorometric measurements, each reading was standardized to show the measurements in similar concentration. Blank sample measurements were subtracted from each sample readings in order to avoid non-specific emissions.

$$IR_n = \frac{(I_n - B_n) * 1000}{Q} \tag{4.1}$$

N_{FRET} is an important indicator for showing the rates of FRET signal and the calculations were done as described by Hoppe *et al.* [34]. Base parameters of N_{FRET} are α and β which were calculated measuring cell samples only expressing mCherry and EGFP constructs respectively.

Emission spectra consist of I_A, I_D and I_F for each experimental setup was done as triplicate. Using the emission spectra of samples, α and β were calculated for mCherry and EGFP respectively as following:

$$\alpha = \frac{I_F}{I_A} \tag{4.2}$$

$$\beta = \frac{I_F}{I_D} \tag{4.3}$$

In this study, calculations resulted $\alpha = 0,0624$ and $\beta = 0,0326$. The α and β calculations were used to subtract basal mCherry and EGFP levels from emission spectra of the samples.

After the subtraction of basal levels of the fluorophores, N_{FRET} was calculated as follows:

$$N_{FRET} = \frac{I_F - \alpha I_A - \beta I_D}{\sqrt{I_A * I_D}} \tag{4.4}$$

When the sample was excited at donor excitation wavelength (488 nm), I_F was taken from arbitrary unit reading at 607 nm, I_D was taken from arbitrary unit reading at 508 nm. When the sample was excited at acceptor excitation wavelength (588 nm), I_A was taken from arbitrary unit reading at 608 nm. Maximum peaks of the emission spectra were observed in these wavelengths. All of the sample conditions were prepared as triplicate and the calculations were done for each replicates in the triplicate groups.

After calculations of N_{FRET} for each samples, the results were analyzed through one-way ANOVA followed by Dunnett's multiple comparisons test. Statistical significances of the samples were showed for each triplicate groups.

4.4. Confocal Laser Scanning Microscopy

4.4.1. Seeding of Cells on Coverslips

One 20 mm x 20 mm cover slip was placed in a 6 cm cell culture dish and was sterilized by UV irradiation in a biosafety cabinet at least half an hour. HEK293 cells were seeded onto the dish and plasmid DNA constructs were transfected by calcium phosphate transfection method as described in Section 4.2.2.

4.4.2. Fixation and Preparation of Samples

After 24 hours of transfection, the dishes containing the cover slips were washed with 1X PBS. Fixation of the cells on cover slips were done removing the PBS and adding 500 μl 4% PFA directly on top of the cells fixed on cover slips. The cells were incubated with PFA at room temperature for 5 mins. Next, PFA was removed and the cover slips were washed with 1X PBS, then the cover slips were grabbed using forceps, flipped carefully and put on microscope slides as upside down position with 20 μl of mounting medium in between the cover slips and slides. The slides were stored in a special closed box at 4°C.

4.4.3. DAPI Staining

1 mg/ml (200X) DAPI stock solution which was aliquoted and kept at -20°C was diluted in PBS to have final concentration of 1X. Diluted 1X DAPI solution was transferred onto fixed cells on cover slips in a drop-wise manner. Cells were incubated with DAPI at room temperature for at least 5 mins. Lastly, the cells were washed with 1X PBS before mounting on microscope slides.

4.4.4. Visualization by Confocal Laser Scanning Microscopy

Fixed cells were visualized using confocal laser scanning microscope (Leica TCS SP8, Germany). Setup settings of excitation and emission spectra of fluorophores were given in Table 4.4. Confocal images were taken using 40x-water immersion objective. A few amounts of ddH_2O was put between the objective and the sample to decrease refraction of light.

Table 4.4. Settings used in confocal laser scanning microscopy.

Fluorophore	**Laser**	**Excitation**	**Emission Range**
DAPI	Diode, 50 mW	405 nm	410 nm - 450 nm
EGFP	Ar, 65 mW	488 nm	493 nm - 578 nm
mCherry	HeNe, 1 mW	543 nm	601 nm - 748 nm

4.5. Western Blotting

4.5.1. Preparation of Samples

Cells were transfected with plasmid DNA constructs as described in Section 4.2.2. After 24 hours, media was removed and cells were collected in 200 μl of 1X Laemmli buffer by a scraper. After taking 40 μl of sample aliquots on ice, the sample to be used was denatured at 95°C for 5 mins. The remaining aliquots were kept in freezer at -20°C for future use.

4.5.2. Preparation of SDS-PAGE Gels

SDS-PAGE gels were prepared having 1.5 mm thickness and 15-well on them. In the preparation of one of the gel, 7.5 ml 15% gel solution was mixed with 7.5 μl TEMED and 75 μl 10% APS solutions, then the mixture was homogenized by pipetting and transferred in between casting glasses. Top of the poured gel was covered with 1 ml isopropanol in order to ensure a flat surface.

After polymerization of the resolving gel for 30 mins, the isopropanol at the top was removed and stacking gel was prepared by mixing 4 ml 4% gel solution with 4 μl TEMED and 40 μl 10% APS solutions. The mixture was homogenized by pipetting and immediately transferred on top of the polymerized resolving gel. Next, the comb was inserted and stacking gel was allowed for polymerization. After the polymerization process, the comb was removed and the gel in casting glasses was placed in gel tank which is full with 1X TGS Running Buffer.

4.5.3. Protein Gel Electrophoresis

Previously polymerized SDS-PAGE gel in electrophoresis tank was stayed in 1X TGS Running Buffer. Before the electrophoresis, all the samples were prepared as described in Section 4.5.1. 15 μl of each sample was loaded to separate wells of 1.5 mm 15 well gel. To prevent "smile effect", empty wells were loaded with black sample which consists of 1X PBS mixed with Laemmli. 80 V was applied to the samples until they pass the stacking gel and enter the resolving gel. After entering to the resolving gel, the voltage was increased to 120 V. The electrophoresis was stopped when the dye reaches to the bottom of the gel.

4.5.4. Semi-dry Transfer

Proteins run on SDS-PAGE gel were blotted onto PVDF membrane using the semi-dry transfer method. A sandwich of two filter papers, PVDF membrane, SDS-PAGE gel, and two filter papers were placed on semi-dry transfer apparatus in this order. To remove bubbles between the layers, roller was used after placing each of the layers. Cover of the transfer apparatus was closed in correct orientation to provide the proteins to run towards positive side. The blotting was completed under 10 V in 35 mins.

4.5.5. Membrane Blocking

The PVDF membrane was taken from the semi-dry system and placed in a plastic dish as the protein blotted side facing upwards for subsequent washing and incubation steps. The membrane was washed with TBS-T three times for 5 mins and blocked with 5% BSA for 1 hour at room temperature. After the blocking, the membrane was washed three times with TBS-T for 5 mins.

4.5.6. Antibody Incubation

After the blocking and washing, the membranes were incubated with primary antibody solutions at 4°C overnight. To prevent microbial growth, sodium azide solution was added to the primary antibody while it is been prepared. After the incubation, the primary antibody was transferred into a 50 ml falcon tube and kept at -20°C for future use. The membrane was washed with TBS-T three times for 5 mins. Next, the membrane was incubated with secondary antibody solution in room temperature for 1 hour. Because of the inhibitory effect of sodium azide on HRP of the secondary antibody, sodium azide was not added while the secondary antibody solution was being prepared. The secondary antibody was chosen against the host species of the primary antibody in order to direct them against each other. After the incubation of secondary antibody, the membrane was washed three times with TBS-T for 5 mins.

4.5.7. Visualization of Membrane

The ECL western blotting substrates (Thermo Fisher Scientific, USA) were mixed and transferred onto the membrane which was put on the clean surface of the visualization device (Syngene, UK). The air bubbles were removed and imaging was completed using the device.

5. EXPERIMENTS AND RESULTS

5.1. Introduction of Single and Double Mutations to EGFP-C3-PYD, EGFP-C3-CARD, pmCherry-C3-PYD and pmCherry-C3-CARD Plasmids

Initial process for observation of important residues between interaction surfaces started with introduction of single and double aminoacid mutations to EGFP-C3-PYD, EGFP-C3-CARD, pmCherry-C3-PYD and pmCherry-C3-CARD plasmid constructs whose plasmid maps are shown in Appendix B.1, B.2, B.3 and B.4. These plasmids were used as template and site-directed mutagenesis method were applied to create new constructs as described in Section 4.1.2. After design of forward and reverse primers, their annealing temperatures were optimized for each primer set and PCR reaction was performed. Dpn I enzyme was used for restriction digestion of template DNA in order to obtain only mutant constructs. After the digestion, PCR products were run on agarose gel (Figure 5.1). The products were either extracted from the agarose gel or directly used in transformation to obtain single colonies which have the desired plasmid construct. After obtaining the plasmids using mini-prep, all plasmids were sequenced in order to verify the sequences of constructs.

Totally 22 plasmids which carry new single mutations, 44 plasmids which carry double mutations were constructed as shown in Table 3.8 and Table 3.9 and their sequences were verified.

Forward and reverse primers were naturally prone to self-dimerize and to amplify non-specific regions on template plasmids so, selection of at least three colonies per mutant construct and sequencing provided to obtain plasmids which only carry desired mutations.

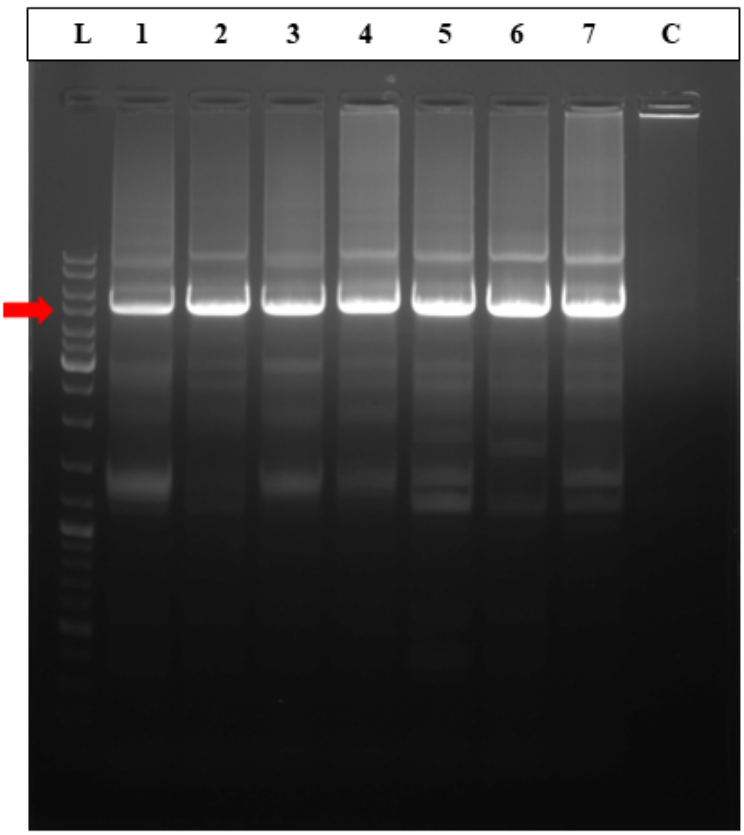

Figure 5.1. Agarose gel image of plasmids which were constructed by SDM in order to create desired mutations. Arrow shows 5000 kb. L = Ladder, C = Control for Dpn I digestion, 1 = mCherry-CARD-130-152, 2 = mCherry-CARD-130-156, 3 = mCherry-CARD-130-158, 4 = mCherry-CARD-130-159, 5 = mCherry-CARD-146-152, 6 = mCherry-CARD-150-158, 7 = mCherry-CARD-152-159

5.2. Full Length ASC Forms Supra-Molecular Globular Speck but PYD and CARD Domains Form Filaments When Expressed Individually

To show the nature of polymerization process, EGFP-hASC plasmid was co-transfected with mCherry-bb plasmid and supra-molecular globular speck formation was observed nearby perinuclear region (Figure 5.2A). Also, to show the polymerization of only PYD and only CARD domains, EGFP-PYD and EGFP-CARD plasmids were co-transfected with mCherry-bb separately. It was observed that, while full length ASC is able to make a speck, only PYD and only CARD domains can show the most filament formation and does not show further organization (Figure 5.2 B and C).

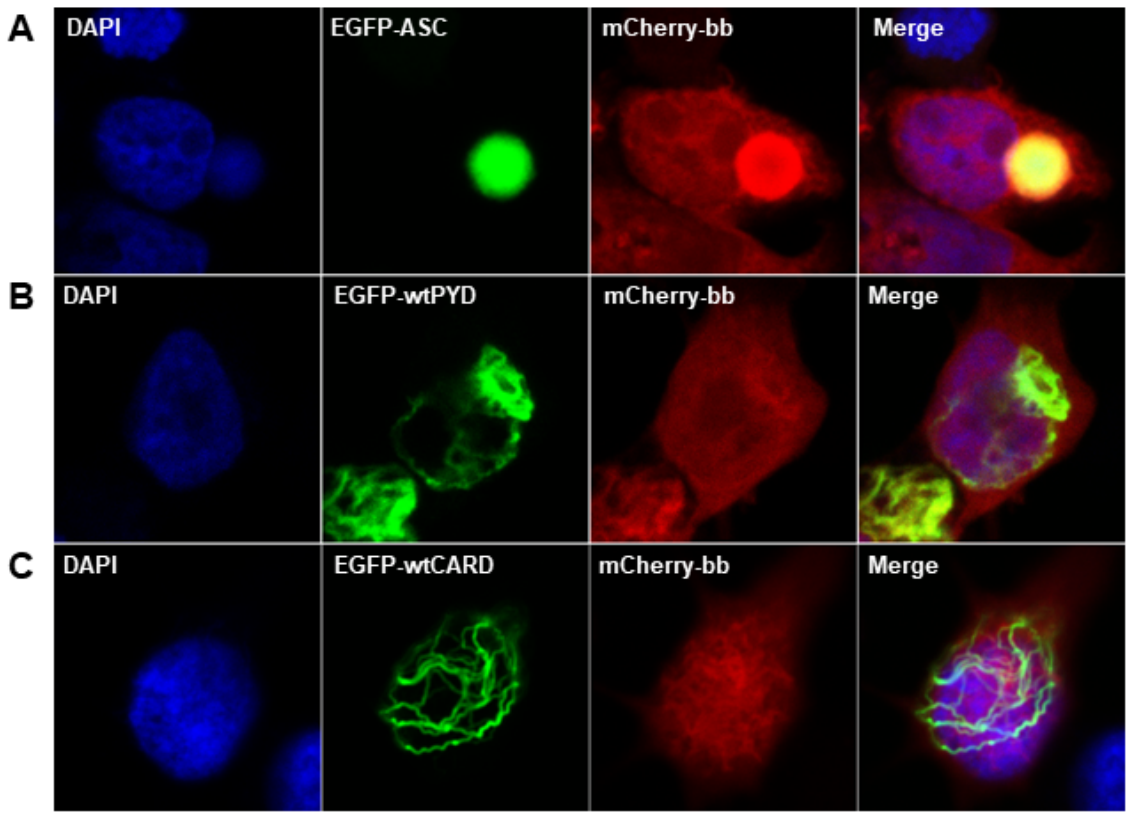

Figure 5.2. Confocal images of HEK293FT cells co-expressing (A) EGFP-hASC + mCherry-bb, (B) EGFP-wtPYD + mCherry-bb, (C) EGFP-wtCARD + mCherry-bb proteins.

5.3. EGFP and mCherry Tagged PYD-PYD and CARD-CARD Variants Show Co-localization by Homooligomerizations

To show the essential interaction points between PYD and CARD domains, at least two different labels were needed. EGFP and mCherry fluorophores which have excitation peaks of 488 and 588 nm, respectively and emission peaks of 508 and 608 nm, respectively were chosen. These fluorophores are soluble when expressed as only EGFP and only mCherry backbone (bb) and does not interfere with each other when their emission ranges were set as separately from each other.

EGFP-PYD was co-transfected with mCherry-PYD, also EGFP-CARD was co-transfected with mCherry-CARD and their results were shown (Figure 5.3) According to the observations, PYD-PYD and CARD-CARD homooligomerizations occurred as a natural process when these domains were expressed individually. Also, EGFP and mCherry fluorophores were in a synchrony without any blockage of the interactions.

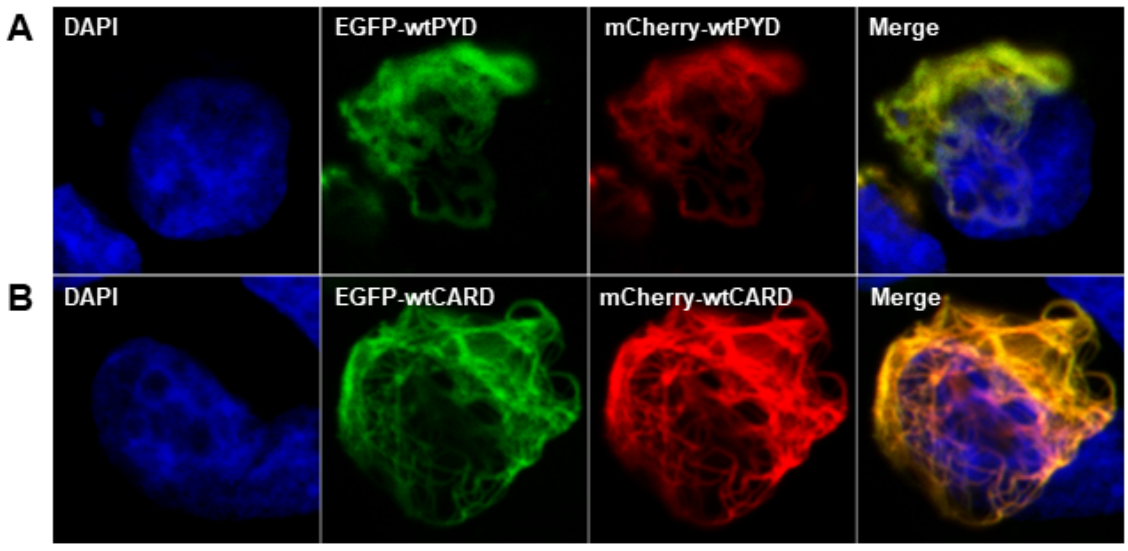

Figure 5.3. Confocal images of HEK293FT cells co-expressing (A) EGFP-wtPYD + mCherry-wtPYD, (B) EGFP-wtCARD + mCherry-wtCARD proteins.

5.4. Photobleaching of mCherry Shows an Increase in Emission of EGFP

To quantify the interaction rate between EGFP and mCherry fused domains, firstly, energy transfer range was determined by acceptor photobleach FRET (apFRET) method. HEK293FT cells were seeded on coverslips and either EGFP-wtPYD and mCherry-wtPYD, or EGFP-wtCARD and mCherry-wtCARD plasmid pairs were co-transfected respectively to different set of cells. After transfection, cells were fixed and photobleaching was done setting emission of EGFP channel to PMT (Photomultiplyer Tube) detector and mCherry channel to HyD (Hybrid Detector). Region of interest (ROI) was determined and the selected ROI was applied throughout the apFRET measurement. After taking first image (Figure 5.4 A), mCherry excitation power was increased to photobleaching range and mCherry fluorophore was photobleached. Second image was taken after photobleaching (Figure 5.4 B)

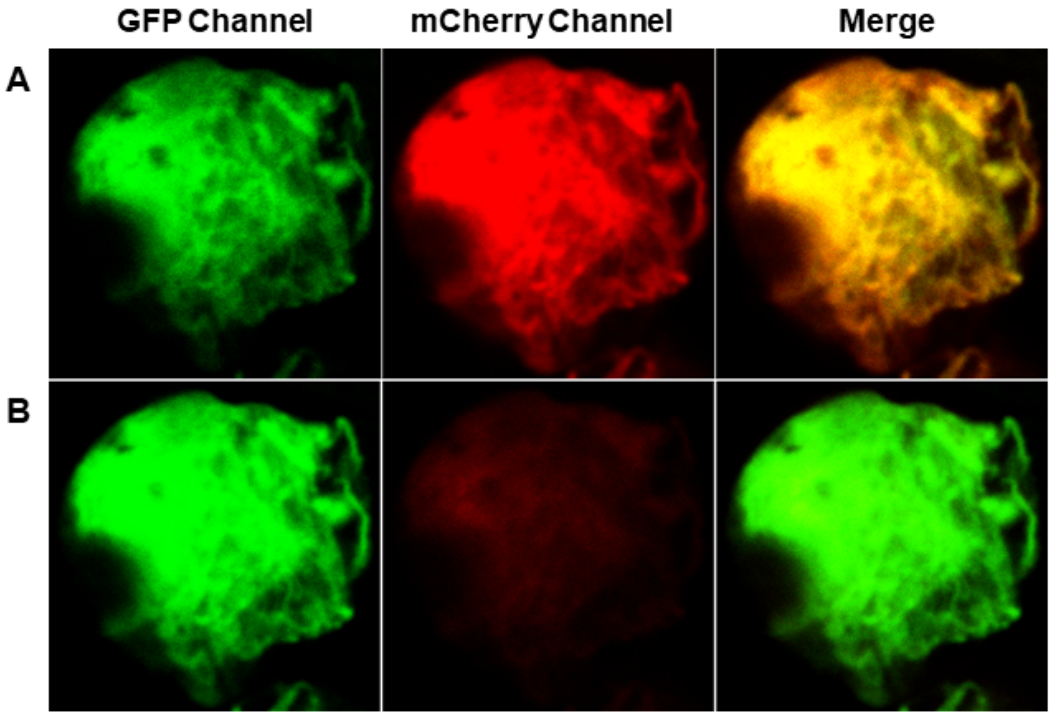

Figure 5.4. Confocal images of HEK293FT cells co-expressing EGFP-wtCARD + mCherry-wtCARD proteins (A) Before Photobleaching (B) After Photobleaching of mCherry protein.

In the photobleaching experiment, when mCherry fluorophore was bleached, emission intensity of the fluorophore was decreased 5-fold. Bleaching of the acceptor fluorophore resulted an increase in emission intensity of EGFP to 1.5 fold (Figure 5.5).

The increase in EGFP emission shows that, EGFP-mCherry pair is a powerful pair to show FRET ratios between them. FRET capability of the fluorophores showed that, homooligomerization dynamics of PYD-PYD and CARD-CARD variants can be determined using the energy transfer system between EGFP and mCherry pairs as a useful indicator for interaction.

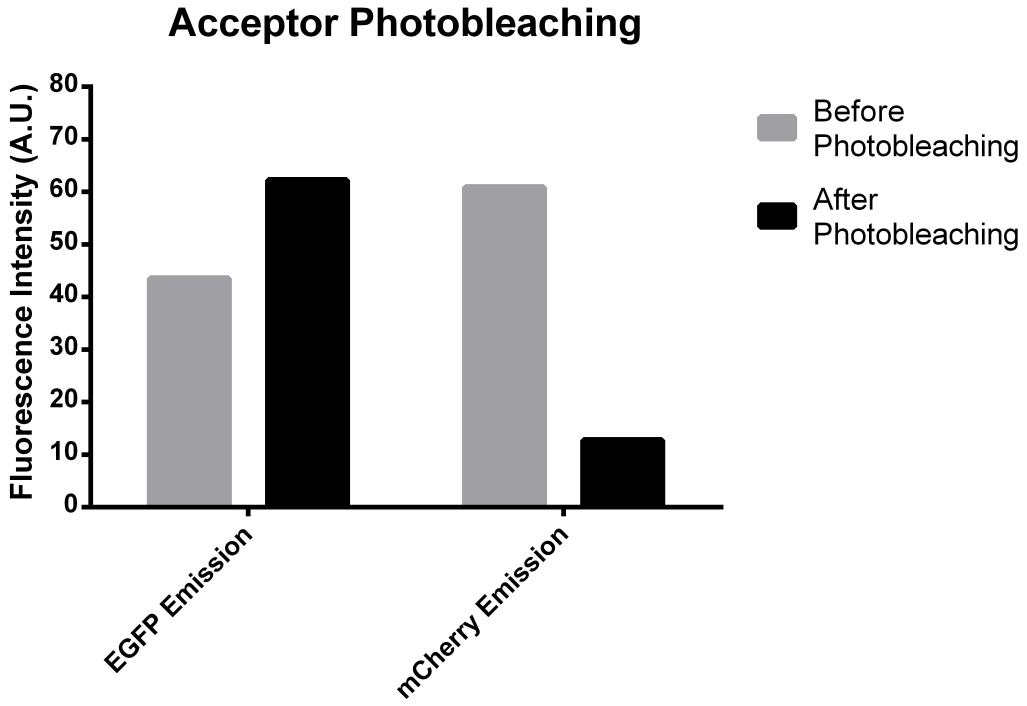

Figure 5.5. Fluorescence intensity graph showing before and after photobleaching of EGFP-wtCARD and mCherry-wtCARD proteins.

5.5. seFRET Measurements Show Interaction Efficiencies Between EGFP and mCherry Fused Domains

Determination of FRET pairs provided us to initiate the seFRET experiments starting with positive and negative controls. HEK293FT cells were seeded in 6-cm dishes and co-transfected with plasmids as described in Section 4.2.2. After transfection, cells were collected in 1.5 ml 1X PBS solution as described in Section 4.3.1 and fluorescence intensities of the samples were measured as described in Section 4.3.2. EGFP was excited at 488 nm and emission spectra was collected between 488 - 700 nm having emission maxima at 508 nm. mCherry was excited at 588 nm and emission spectra was collected between 588 - 700 nm having emission maxima at 608 nm. As the initial results showed that, EGFP-wtPYD and mCherry-wtPYD co-expression provides co-localization of the wt domains with the fluorescence tags (Figure 5.3) and the co-localization can be quantified using seFRET (Figure 5.6 A and B). When EGFP is excited at 488 nm, its emission excites nearby mCherry protein and causes secondary emission from mCherry if these fluorophores are in close proximity (¡10 nm). Our positive control results showed the secondary peak because wtPYD domains fused with both fluorophores are being interacted. Negative control showed no secondary emission peak because EGFP does not carry PYD domain to interact with mCherry-wtPYD. When EGFP emission peaks of positive and negative control results are compared, emission peaks caused by seFRET can be seen on acceptor (mCherry) emission wavelength at 608 nm (Figure 5.6 C).

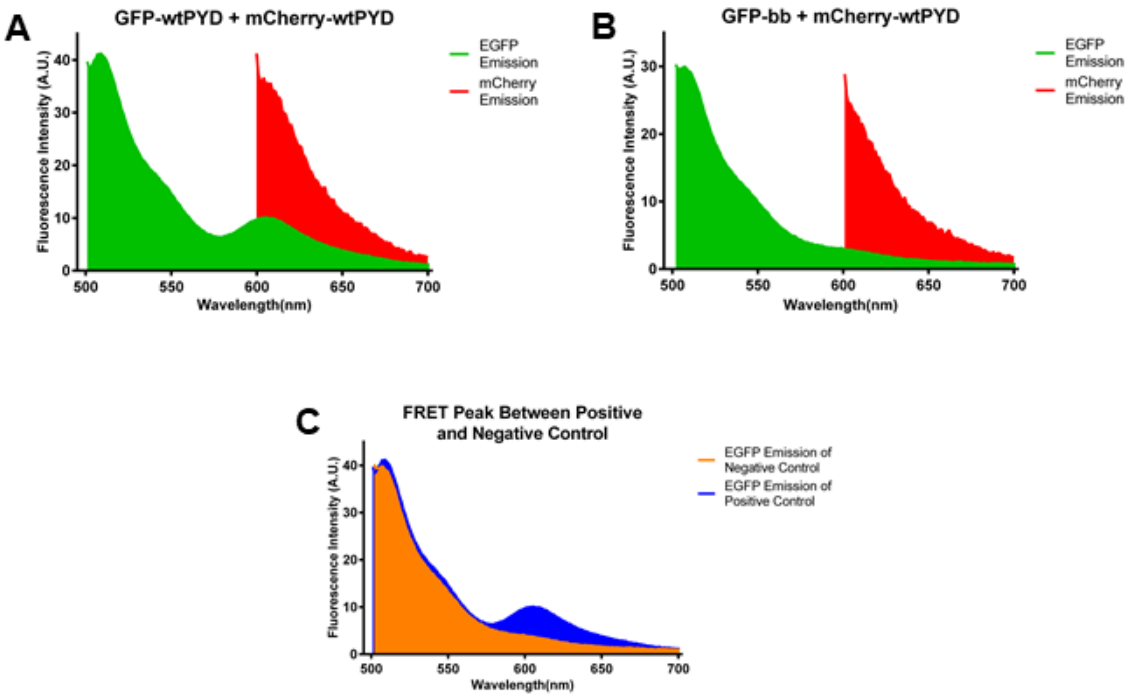

Figure 5.6. Emission spectra of HEK293FT cells which express (A) GFP-wtPYD + mCh-wtPYD as positive control, (B) GFP-bb + mCherry-wtPYD as negative control. Secondary peak comparison between positive and negative controls of GFP emission spectra (C) when excited at 488 nm.

FRET Efficiency is an important indicator to show interaction efficiencies not only between wt conditions, but also between wt-mutant and mutant-mutant conditions. FRET Efficiency was initially determined by a calculation from a mathematical formula as described in Section 4.3.3. Firstly, HEK293FT cells were seeded on 6-cm dishes, only EGFP-bb and only mCherry-wtPYD plasmids were transfected to different cells in order to obtain basal levels of these fluorophores. Transfected cells were collected and fluorometric measurement was done. Here, EGFP-bb only gave primary emission peak at 508 nm when excited at 488 nm because acceptor was not present to quench the primary emission of EGFP (Figure 5.7 A). Also, mCherry-PYD was used to obtain basal mCherry emissions upon excitation at 488 and 588 nm separately (Figure 5.7 B).

In N_{FRET} calculations, two proportional constants α, the basal fluorescence of mCherry at 608 nm upon excitation at 408 nm and β, the basal fluorescence of EGFP at 608 nm upon excitation at 588 nm was calculated. α was calculated by dividing fluorescence intensity of acceptor (mCherry) at 608 nm upon excitation at 488 nm to fluorescence intensity upon excitation at 588 nm. β was calculated by dividing fluorescence intensity of donor (EGFP) at 608 nm to intensity at 508 nm. All the calculations were done as described in Section 4.3.3. Using the α and β constants, N_{FRET} calculations were done for each experiment set as triplicate.

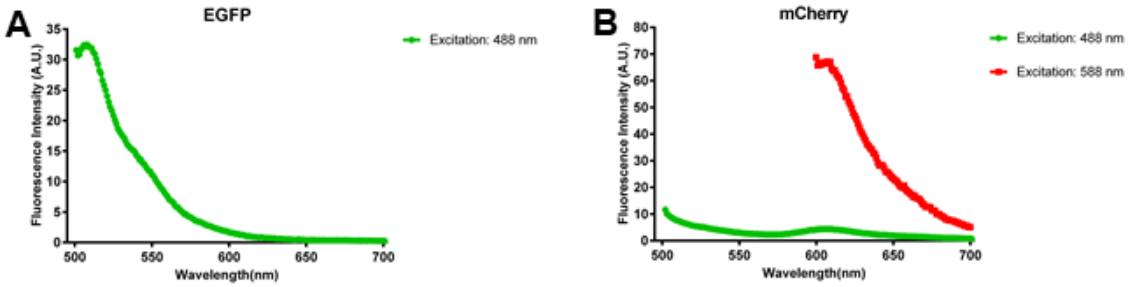

Figure 5.7. Emission spectra of HEK293FT cells which express (A) only GFP-bb excited at 488 nm and (B) only mCherry-wtPYD excited at 488 and 588 nm respectively.

5.6. Mutational Screening on PYD and CARD Constructs

Previous studies showed that, certain residues on PYD and CARD domains are essential for proper homooligomerization because some changes on these sites cause disruption of interaction between the domains [20,37,38]. To show the effects of disruption of interaction at important points, mutational screening was done by introducing Alanine amino acid at the site to be mutated. Alanine was chosen because it allowed us to predict roles of the side chains on the original residues because alanine has a methyl side chain lacking distinct backbone dihedral angle preferences. It also prevents to introduce extra conformational flexibility to protein back bone. Introduction of alanine amino acid is also one of the easiest substitutions because it requires just one or two nucleotide substitution on template DNA plasmid.

While using a few previously studied important mutations, we also created new single mutations and observed their effects. Here, the most important factor was to reveal the location of the amino acid to be mutated in order to contribute the effects to different types of interactions.

All the mutational screenings were done on PYD and CARD domains rather than full length ASC because effects of mutations on a domain of full length ASC protein could be compensated by another domain masking the effect on homooligomerization between domains. On PYD domain, D48A mutation showed co-localization with wt domain but PYD-D48A mutants were not able to homooligomerize with themselves (Figure 5.8 A and B). This expanded the interaction cases to mutant-wt co-localization and mutant-mutant no co-localization for D48A variants. On CARD domain, Y146A mutant showed similar phenotypes by slightly interacting with wt but it also failed to interact Y146A mutant counterpart (Figure 5.8 C and D). Also, Q185A mutation on CARD domain showed very distinct phenotype because mutant variant was able to co-localize with wt in very long and straight filaments without making a branching (Figure 5.8 E).

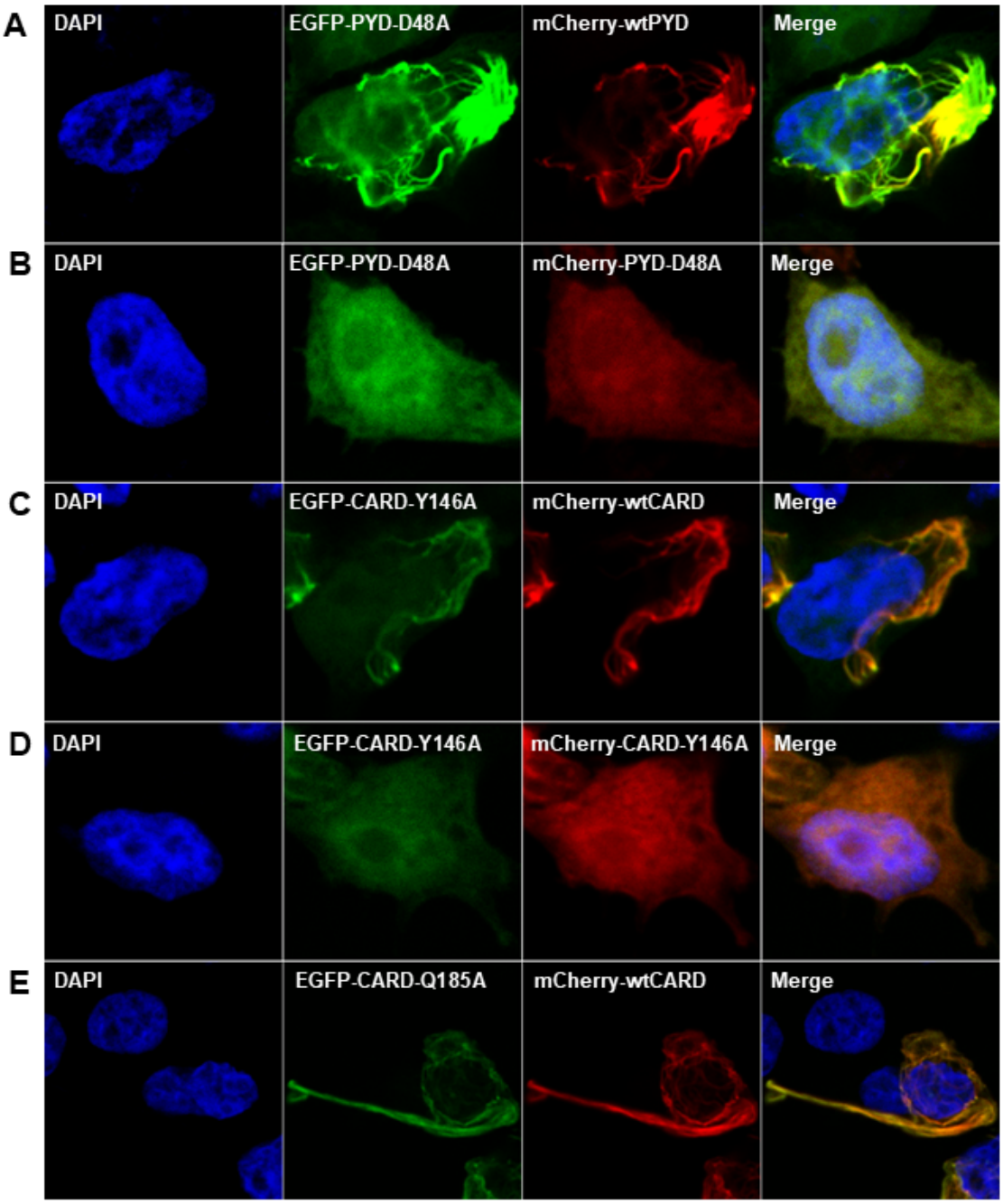

Figure 5.8. Confocal images of HEK293FT cells co-expressing (A) EGFP-PYD-D48A + mCherry-wtPYD, (B) EGFP-PYD-D48A + mCherry-PYD-D48A, (C) EGFP-CARD-Y146A + mCherry-wtCARD, (D) EGFP-CARD-Y146A + mCherry-CARD-Y146A and (E) EGFP-CARD-Q185A + mCherry-wtCARD proteins.

5.7. Effects of Single Mutations on PYD Variants

Mutational screenings were broadened by introducing single amino acid changes to alanine on PYD domain and the experimental set up was to co-transfect HEK293FT cells with EGFP-PYD single mutants with either mCherry-wtPYD or mCherry-PYD same single mutant variant in order to observe effects of the mutation on both wt-mutant and mutant-mutant homooligomerization process. Average emission spectra for each triplicate sample can be found in Figure A.1 and Figure A.2.

5.7.1. Partially Disruptive Mutations Block Interaction Between Mutant Domains

On PYD domain, not all the mutations were able to block interactions between domains entirely. The effects were classified in two patterns. First, the mutation partially disrupted mutant-mutant interaction while being more tolerant between wt-mutant domains. Second, mutation could give less disruption to mutant-mutant homooligomerization and showed similar pattern with wt-mutant co-localization.

5.7.1.1. Disruption Between Mutant-Mutant Interactions. In the case, mutation caused disruption between mutant-mutant domains more than wt-mutant domains. E13A mutation showed a co-localization with wt domain but mutant-mutant interaction rate was significantly decreased (Figure 5.9 and Figure 5.13 A). The mutation located on Type 3b interaction surface on Helix 1. E13A mutation showed wt-mutant co-localization and decreased mutant-mutant co-localization.

D48A mutation showed wt-mutant co-localization in reduced levels on the other hand, mutant-mutant homooligomerization was unable to occur (Figure 5.10). On the other hand, while wt-mutant interaction ratio was quantified as in nearly positive control, mutant-mutant interaction gave more ratio than negative control (Figure 5.13 B). D48A mutants showed limited rate of monomeric interaction but visible filament formation was inhibited so, inhibition case is observed between interaction of the variant.

D48A mutation is on Type 1a interaction surface on loop between Helix 3 and 4.

T53A mutation showed nearly increased co-localization between wt-mutant domains and also showed less co-localization between mutant-mutant domains (Figure 5.11). T53 residue is located on Helix 4 but not properly defined in an interaction surface. Nevertheless, interaction ratio between mutant-mutant homooligomerization was decreased even being more tolerant in wt-mutant condition (Figure 5.13 C).

Y60A mutation resulted in nearly complete disruption between wt-mutant and mutant-mutant interactions. Y60A mutant could not interact with wt so, wt remained as homooligomerized with other wt domains. Y60A mutant also failed to interact with other Y60A mutants (Figure 5.12 and Figure 5.13 D). Y60 is located on loop between Helix 4 and 5 but not identified as a point in particular interaction site. The result showed completely new phenotype increasing the importance of Y60 residue on homooligomerization.

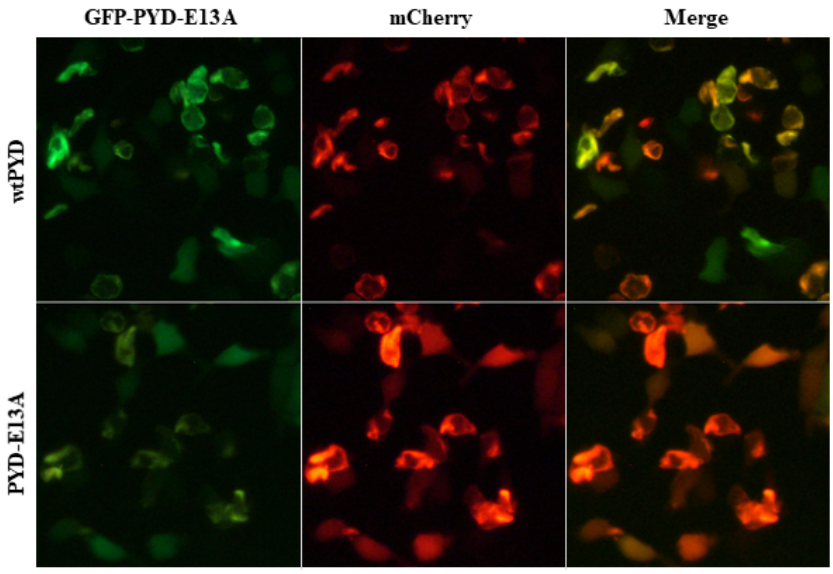

Figure 5.9. Fluorescent image set of EGFP-PYD-E13A single mutant variant (left column) co-expressed with mCh-wtPYD and mCh-PYD-E13A variants (middle column), and merge (right column).

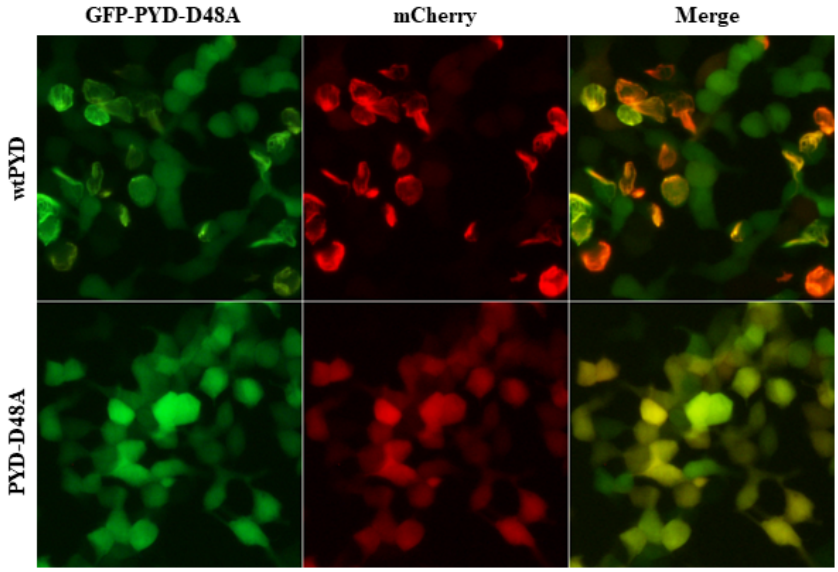

Figure 5.10. Fluorescent image set EGFP-PYD-D48A single mutant variant (left column) co-expressed with mCh-wtPYD and mCh-PYD-D48A variants (middle column), and merge (right column).

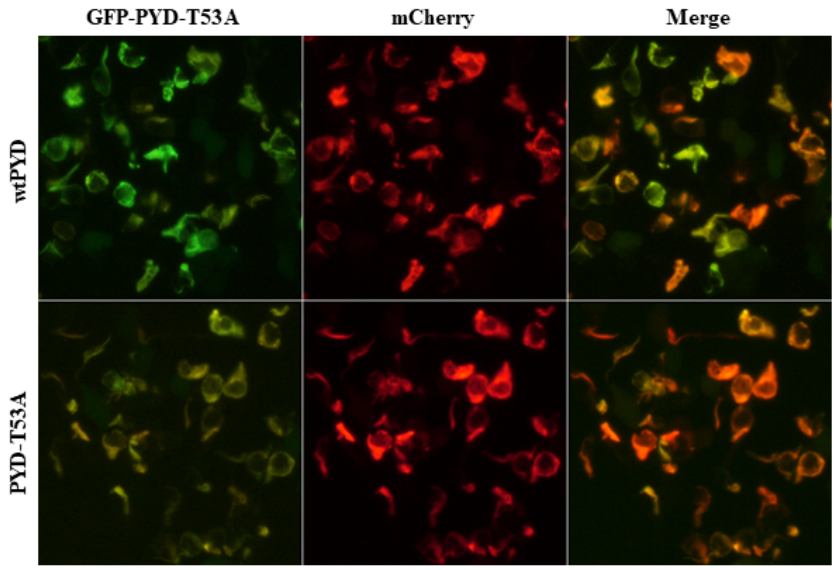

Figure 5.11. Fluorescent image set of EGFP-PYD-T53A single mutant variant (left column) co-expressed with mCh-wtPYD and mCh-PYD-T53A variants (middle column), and merge (right column).

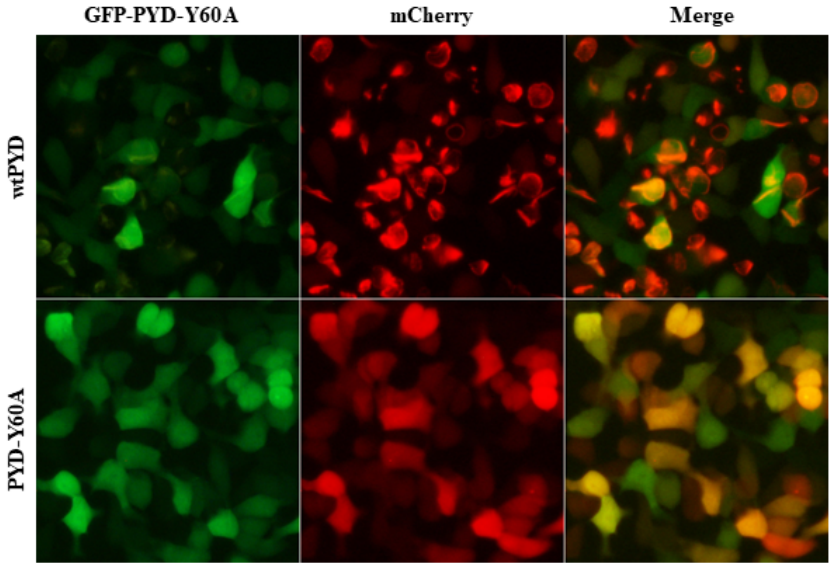

Figure 5.12. Fluorescent image set of EGFP-PYD-Y60A single mutant variant (left column) co-expressed with mCh-wtPYD and mCh-PYD-Y60A variants (middle column), and merge (right column).

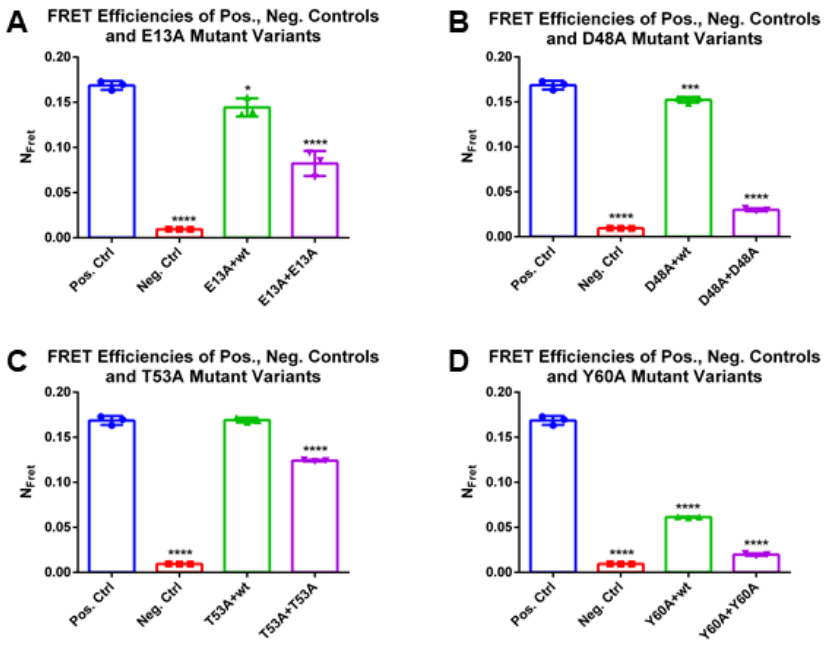

Figure 5.13. N_{FRET} graphs of (A) PYD-E13A, (B) PYD-D48A, (C) PYD-T53A and (D) PYD-Y60A single mutant sets.

5.7.1.2. Wild Type and Mutant Variants Show Similar Phenotypes. In that case, wild type-mutant and mutant-mutant phenotypes were similar and were not changed towards disruption. L25A mutation on PYD domain did not affect the homooligomerization both in interaction with wt and same mutant. Also, rates of interactions were similar with positive control (Figure 5.14 and Figure 5.18 A). L25 resides on Type 1b interaction surface on Helix 2.

S29A mutation interestingly increased wt-mutant and mutant-mutant interaction efficiencies towards increased co-localization which is more than positive control that is both observed on interaction ratios and quenching of EGFP primary signal (Figure 5.15 and Figure 5.18 B). S29 is located on Helix 2 and not previously not defined on any interaction surface however, it is close to Type 1b surface.

E67A and L85A mutations showed similar phenotypes with each other. The interaction rates for wt-mutant and mutant-mutant conditions were nearly similar and not affected by the mutation (Figure 5.16, Figure 5.17, Figure 5.18 C and D). E67 and L 85 are located on Helix 5 and Helix 6 respectively. Side chain of L85 is located as inward position into the domain.

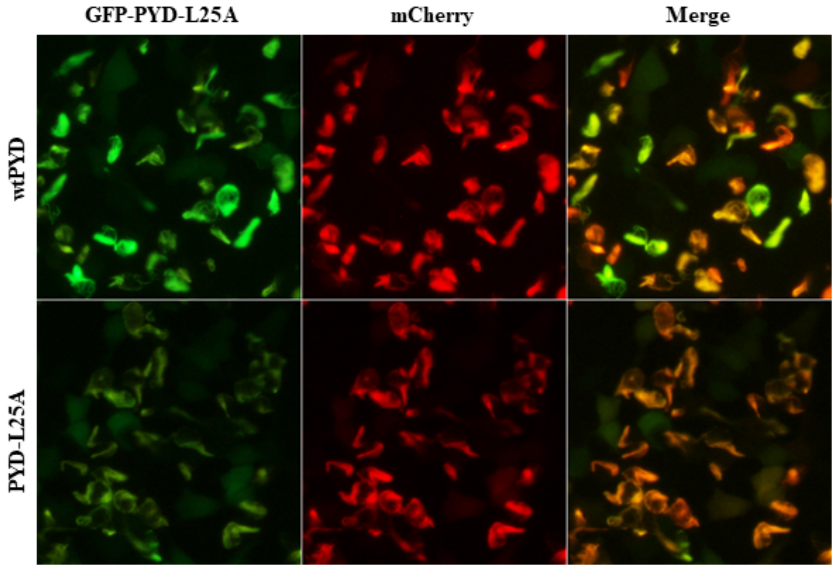

Figure 5.14. Fluorescent image set of EGFP-PYD-L25A single mutant variant (left column) co-expressed with mCh-wtPYD and mCh-PYD-L25A variants (middle column), and merge (right column).

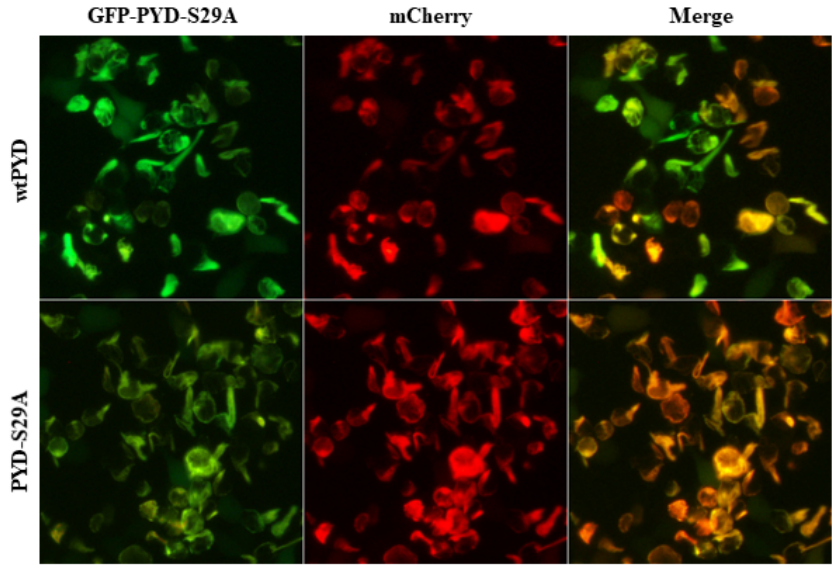

Figure 5.15. Fluorescent image set of EGFP-PYD-S29A single mutant variant (left column) co-expressed with mCh-wtPYD and mCh-PYD-S29A variants (middle column), and merge (right column).

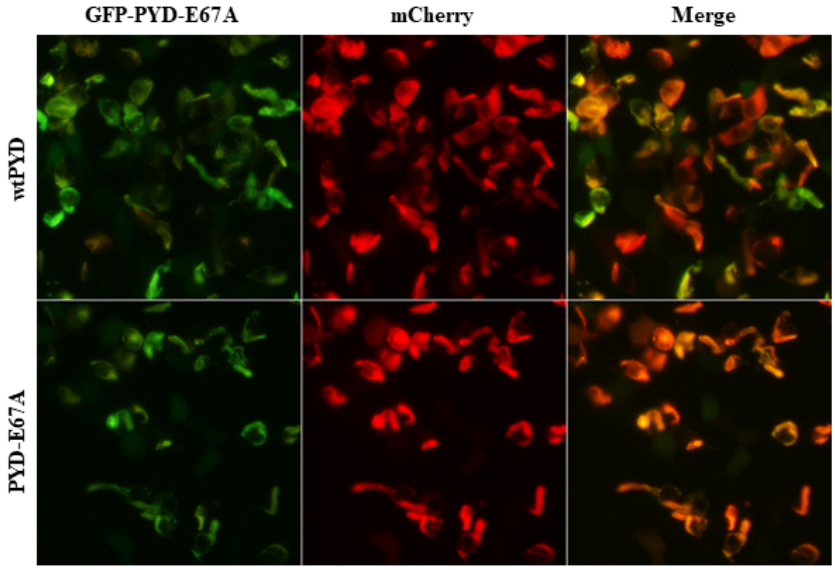

Figure 5.16. Fluorescent image set of EGFP-PYD-E67A single mutant variant (left column) co-expressed with mCh-wtPYD and mCh-PYD-E67A variants (middle column), and merge (right column).

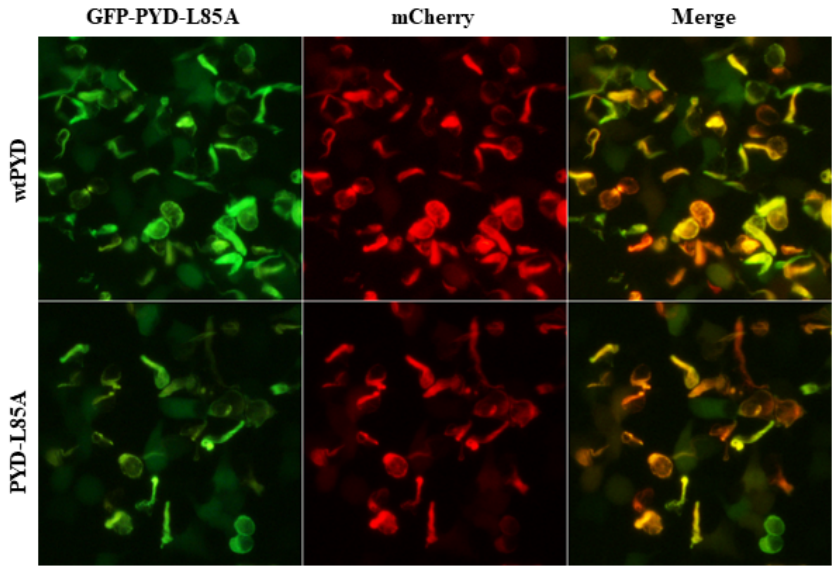

Figure 5.17. Fluorescent image set of EGFP-PYD-L85A single mutant variant (left column) co-expressed with mCh-wtPYD and mCh-PYD-L85A variants (middle column), and merge (right column).

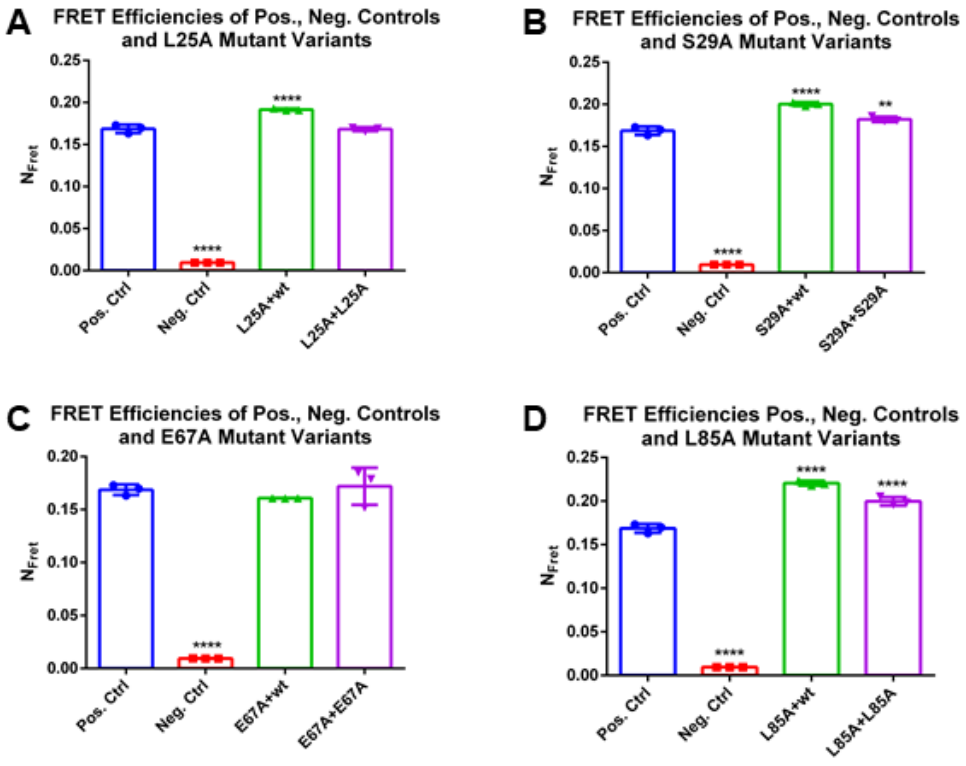

Figure 5.18. N_{FRET} graphs of (A) PYD-L25A, (B) PYD-S29A, (C) PYD-E67A and (D) PYD-L85A single mutant sets.

5.8. Effects of Single Mutations on CARD Variants

To observe effects of single mutations on polymerization dynamics of CARD domain, HEK293FT cells were co-transfected with EFGP-CARD single mutants with either mCherry-wtCARD or mCherry-CARD same single mutant variants. Totally, effects of 11 single mutations on CARD domain were analyzed. Average emission spectra for each triplicate sample can be found in Figure A.3, Figure A.4 and Figure A.5.

5.8.1. Completely Disruptive Mutations Interrupt Interaction Between Wild Type and Mutant Variants

On CARD domain, two of single mutations had completely disruptive effects on bot wt and mutant homooligomerizations. K158A and M159A mutations blocked the homooligomerizations between wt and mutant domains (Figure 5.19, Figure 5.20 and Figure 5.21). Especially, M159A mutation caused decrease in wt-wt homooligomerization while wt-mutant interaction rate is higher than negative control. The situation was caused by inhibition case because of oligomerization of mutant monomers with wt but blocking further interaction surfaces. K158 is located on Type 3b interaction surface on Helix 4 and M159 is not located on any interaction surface in previous studies however, it showed the highest blockage effect on oligomerization.

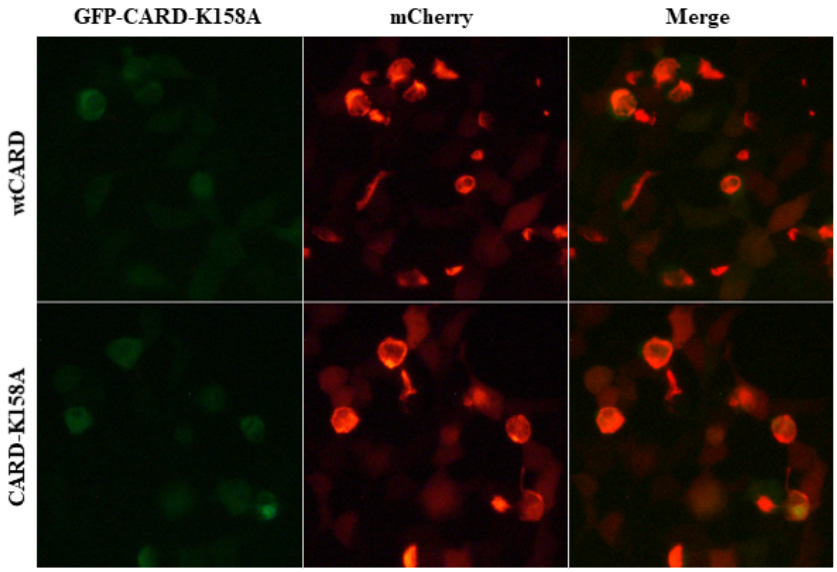

Figure 5.19. Fluorescent image set of EGFP-CARD-K158A single mutant variant (left column) co-expressed with mCh-wtCARD and mCh-CARD-K158A variants (middle column), and merge (right column).

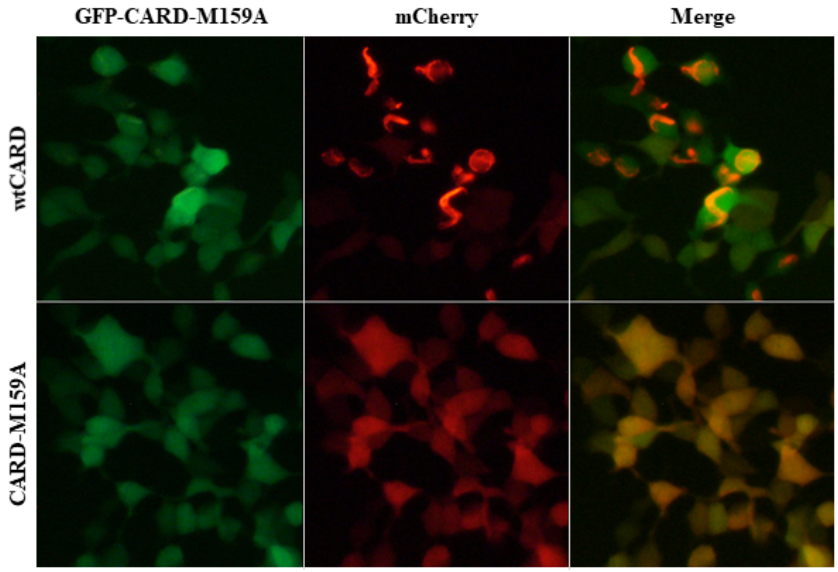

Figure 5.20. Fluorescent image set of EGFP-CARD-M159A single mutant variant (left column) co-expressed with mCherry-wtCARD and mCherry-CARD-M159A variants (middle column), and merge (right column).

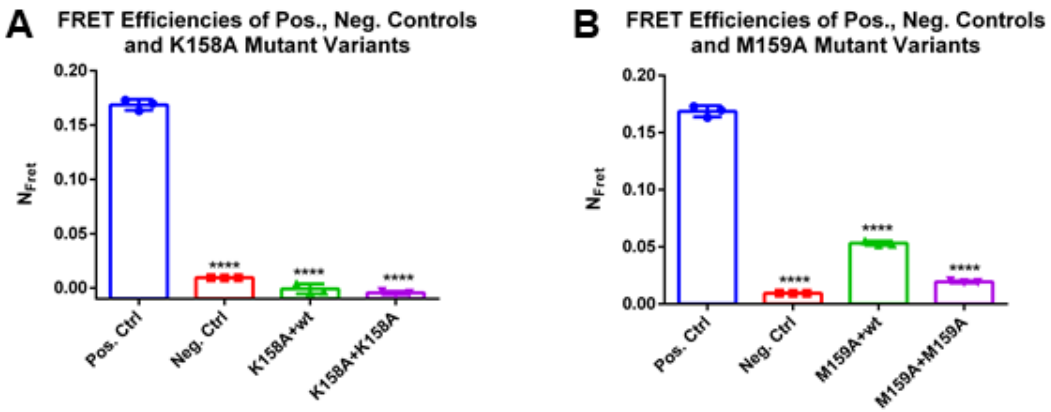

Figure 5.21. N_{FRET} graphs of (A) CARD-K158A and (B) CARD-M159A single mutant sets.

5.8.2. Effects of Partially Disruptive Mutations on Interaction

On CARD domain, some single mutations blocked interaction in mutant-mutant homooligomerization more than in wt-mutant interaction. Also, some mutants showed very slight changes on interactions.

5.8.2.1. Blockage of Homooligomerization Between Mutant Variants. In that case, the single mutations resulted in significant ($p \leq 0.0001$) decreases in mutant-mutant homooligomerization more than in wt-mutant. E130A mutation showed decreased co-localization between wt-mutant and mutant-mutant conditions (Figure 5.22 and Figure 5.26 A). E130 residue is located on Type 1b interaction surface on Helix 2.

Y146A mutation showed a distinct phenotype where the mutant variant could interact with wt without affecting wt-wt oligomerization but mutant-mutant interaction was not observed due to inhibition (Figure 5.23 and Figure 5.26 B). E146 residue is on Type 1b interaction surface on Helix 3.

E152A mutation had disruptive effects on both wt and mutant oligomerizations. Decreased co-localization was observed in both phenotypes and interaction ratios (Figure 5.24 and Figure 5.21 C). E152 amino acid is located on near Type 3b surface on loop between Helix 3 and 4.

W169A mutation blocked mutant-mutant interaction much more than wt-mutant interaction (Figure 5.25 and Figure 5.26 D). The residue is on Type 2a interaction surface between Helix 4 and 5.

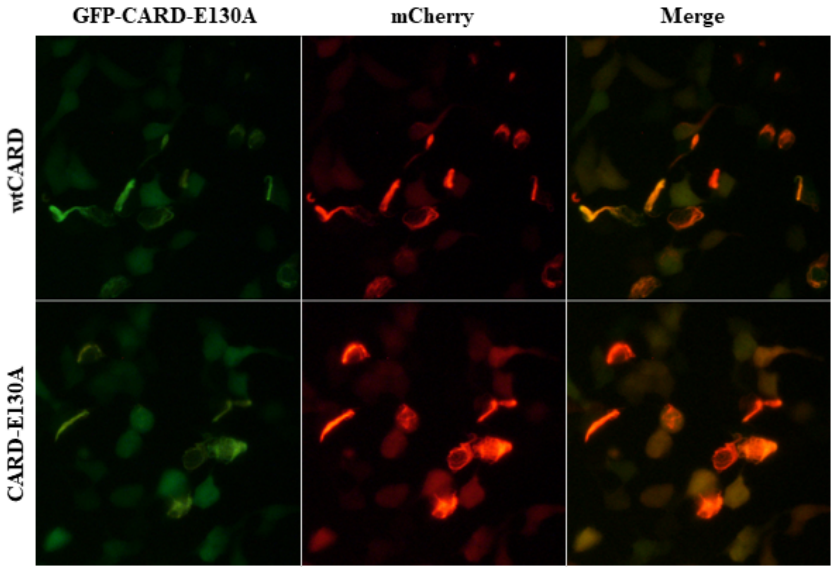

Figure 5.22. Fluorescent image set of EGFP-CARD-E130A single mutant variant (left column) co-expressed with mCh-wtCARD and mCh-CARD-E130A variants (middle column), and merge (right column).

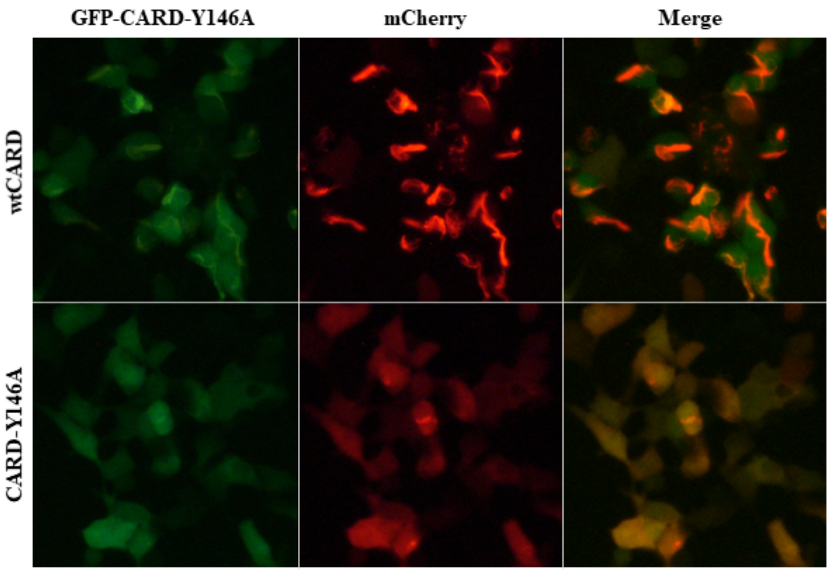

Figure 5.23. Fluorescent image set of EGFP-CARD-Y146A single mutant variant (left column) co-expressed with mCh-wtCARD and mCh-CARD-Y146A variants (middle column), and merge (right column).

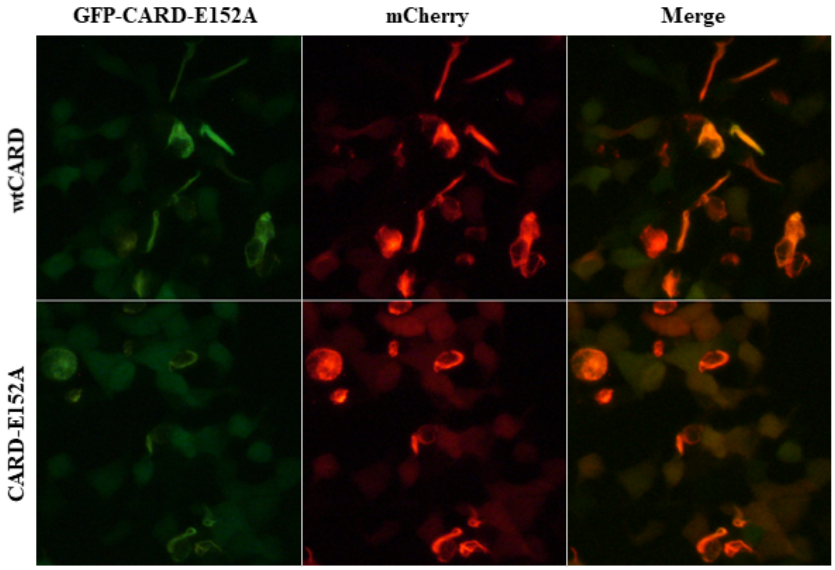

Figure 5.24. Fluorescent image set of EGFP-CARD-E152A single mutant variant (left column) co-expressed with mCh-wtCARD and mCh-CARD-E152A variants (middle column), and merge (right column).

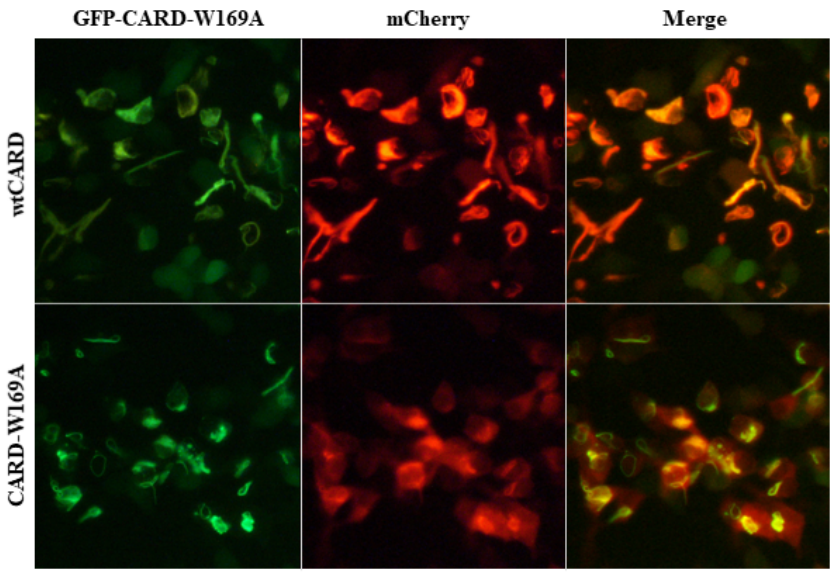

Figure 5.25. Fluorescent image set of EGFP-CARD-W169A single mutant variant (left column) co-expressed with mCh-wtCARD and mCh-CARD-W169A variants (middle column), and merge (right column).

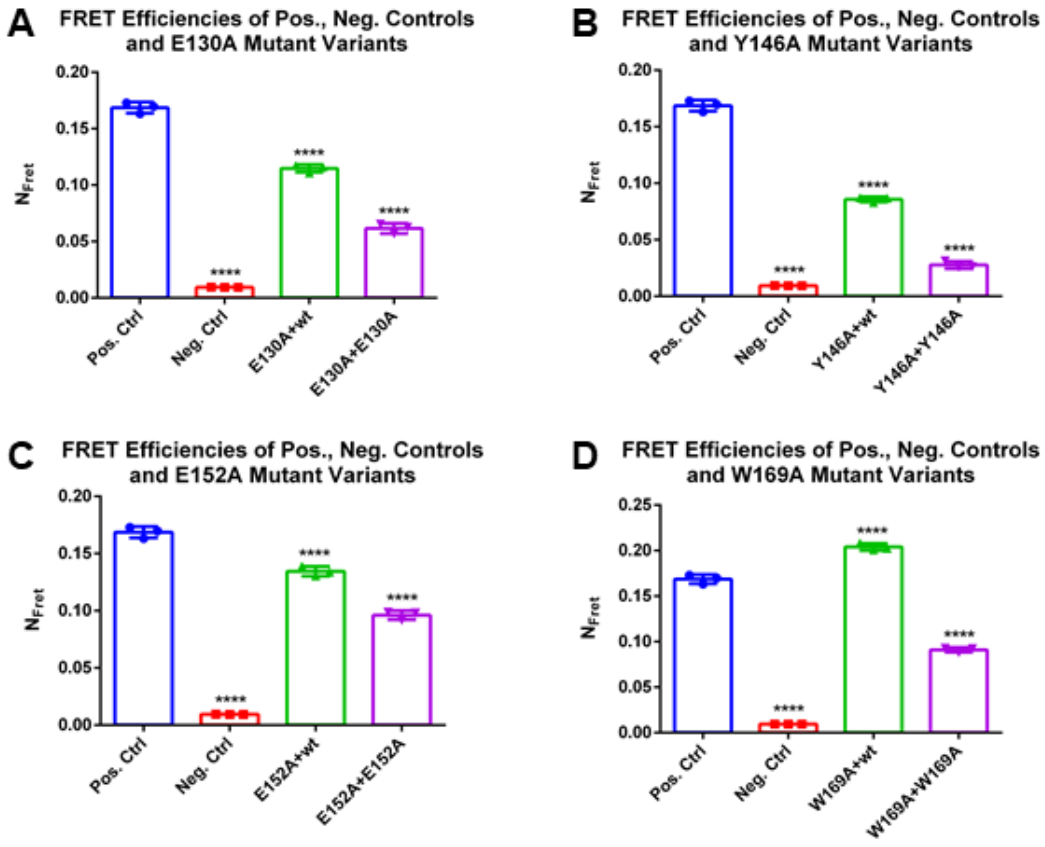

Figure 5.26. N_{FRET} graphs of (A) CARD-E130A, (B) CARD-Y146A, (C) CARD-E152A and (D) CARD-W169A single mutant sets.

5.8.2.2. Mutant and Wild Type Variants Show Similar Phenotypes. Effects of some mutations were tolerated on both wt and mutant variants. R150A mutation did not changed interaction dynamics on both wt and mutant conditions (Figure 5.27 and Figure 5.32 A) although the residue is on Type 1b interaction surface on Helix 3.

P156A caused less interaction rate between mutant-mutant condition than wt-mutant (Figure 5.28 and Figure 5.32 B) even though the residue is located on Type 3b interaction surface on Helix 4.

R182A and E183A showed less branching but interaction between wt-mutant and mutant-mutant conditions were not affected (Figure 5.29, Figure 5.30, Figure 5.32 C and D).

Q185A resulted in very long filaments with nearly no branching but interaction rates were not decreased significantly (Figure 5.31 and Figure 5.32 E). Q185 amino acid resides on Type 2b interaction surface between Helix 5 and 6.

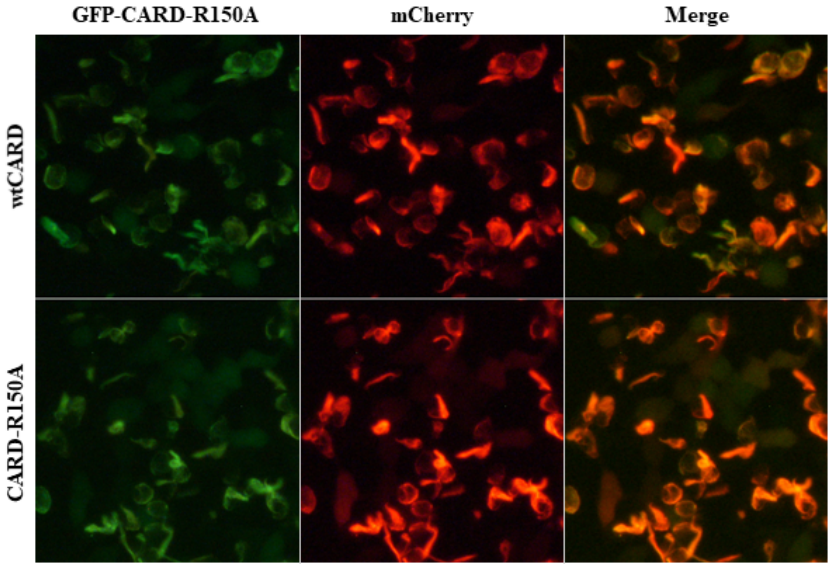

Figure 5.27. Fluorescent image set of EGFP-CARD-R150A single mutant variant (left column) co-expressed with mCh-wtCARD and mCh-CARD-R150A variants (middle column), and merge (right column).

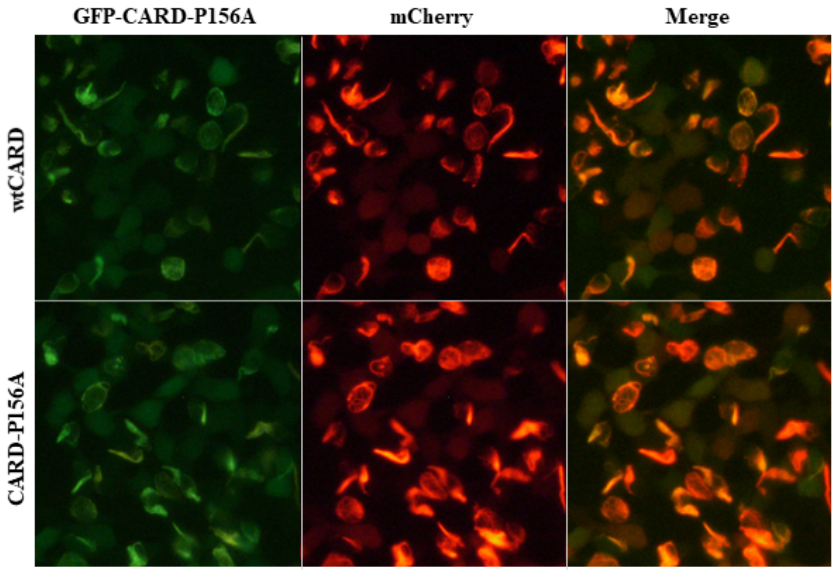

Figure 5.28. Fluorescent image set of EGFP-CARD-P156A single mutant variant (left column) co-expressed with mCh-wtCARD and mCh-CARD-P156A variants (middle column), and merge (right column).

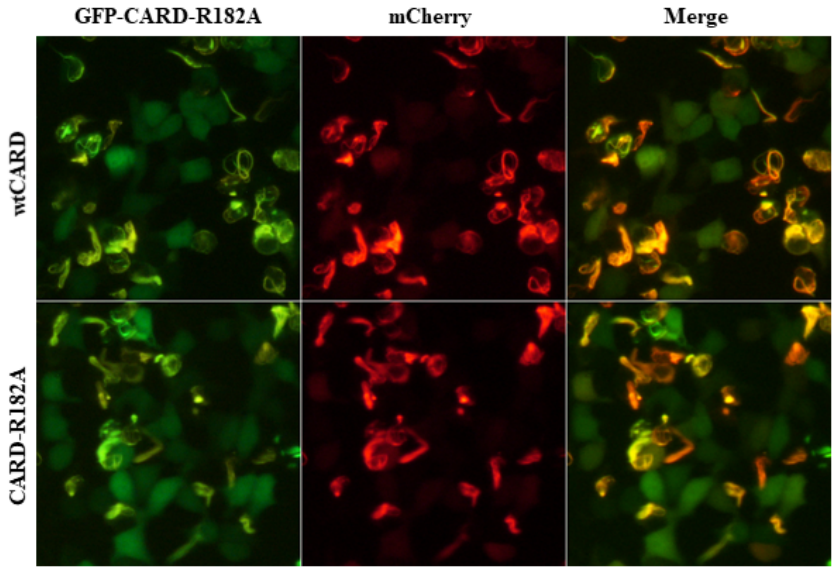

Figure 5.29. Fluorescent image set of EGFP-CARD-R182A single mutant variant (left column) co-expressed with mCh-wtCARD and mCh-CARD-R182A variants (middle column), and merge (right column).

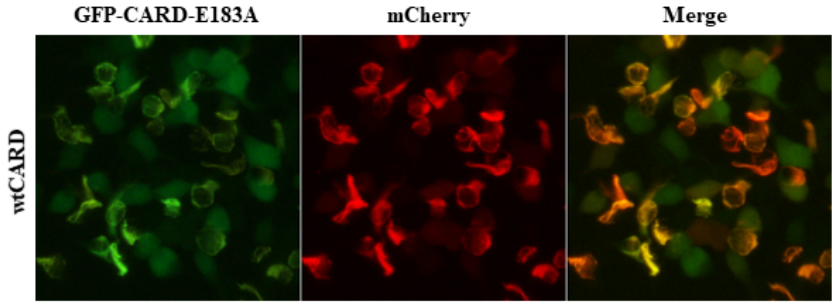

Figure 5.30. Fluorescent image set of EGFP-CARD-E183A single mutant variant (left column) co-expressed with mCh-wtCARD variant (middle column), and merge (right column).

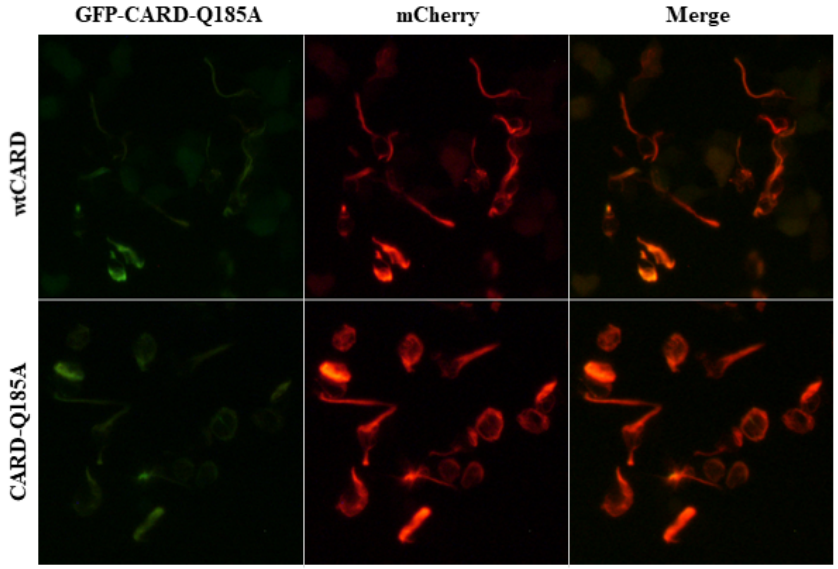

Figure 5.31. Fluorescent image set of EGFP-CARD-Q185A single mutant variant (left column) co-expressed with mCh-wtCARD and mCh-CARD-Q185A variants (middle column), and merge (right column).

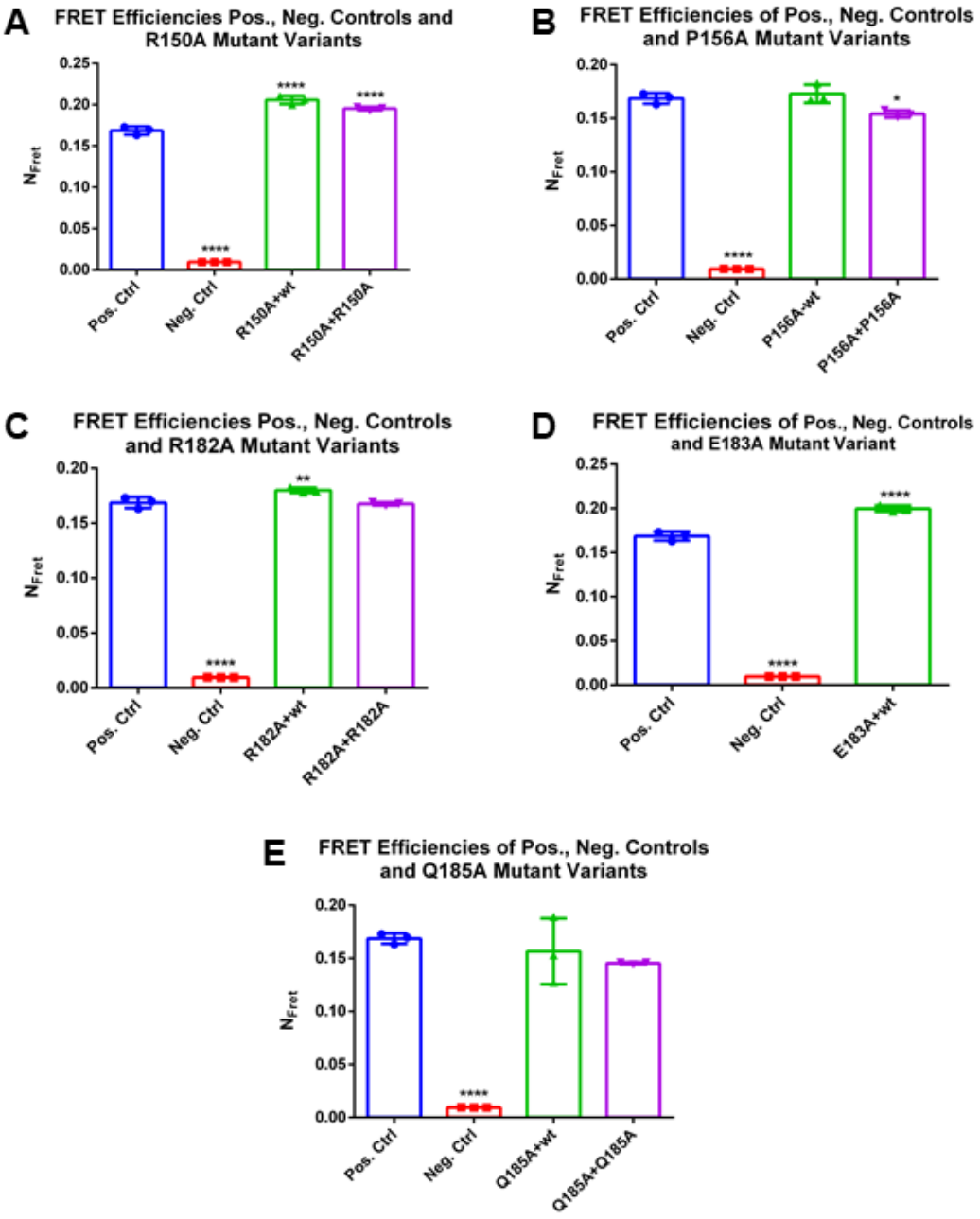

Figure 5.32. N_{FRET} graphs of (A) CARD-R150A, (B) CARD-P156A, (C) CARD-R182A, (D) CARD-E183A and (E) CARD-Q185A single mutant sets.

5.9. Effects of Double Mutations on PYD Variants

Effects of double mutations on homooligomerization dynamics of PYD domain was observed by co-transfecting HEK293FT cells with EGFP-PYD double mutants with either mCherry-wtPYD or mCherry-PYD double mutant variants. Effects of 8 different double mutant sets were observed including 4 sub-sets for each of them. Average emission spectra for each triplicate sample can be found in Figure A.6, Figure A.7, Figure A.8 and Figure A.9.

Double mutations provided us to observe more combinations in phenotypes and to classify the effects of blocked interaction surfaces in a disruptive spectrum manner.

5.9.1. Disruptive Mutations Hinder Interaction Between Mutant Variants

On PYD domain, two of double mutations showed disruptive effects on both wt-mutant and mutant-mutant cases.

In E13A-D48A double mutation case, both of Type 3b and Type 1a interaction surfaces were blocked on the double mutant and it failed to interact wt, E13A, D48A and E13A-D48A variants (Figure 5.33 and Figure 5.35 A). While E13A and D48A mutants can interact with wt, blocked interaction phenotype of E13A-D48 with wt shows that, Type 1 and Type 3 mutations can be partially compensated but if occurs together, Type 2 is not enough to compensate the mutational effect.

In E13A-Y60A double mutation case, inhibition of interaction was observed between the double mutant and all other variants (Figure 5.34 and Figure 5.35 B). When the double mutant was co-expressed with wt, homooligomerization of wt was also inhibited so, the result can be classified in inhibition case.

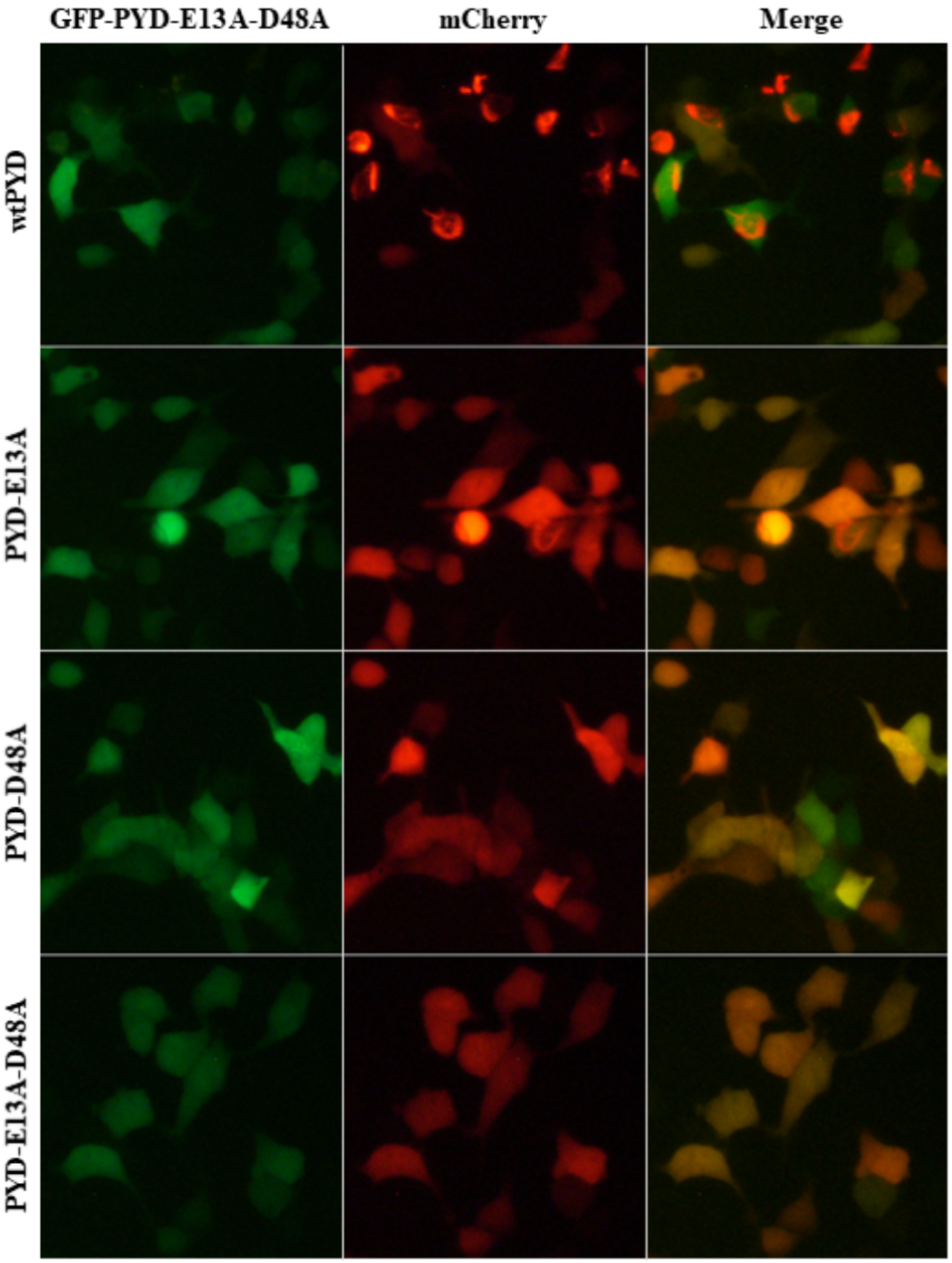

Figure 5.33. Fluorescent image set of EGFP-PYD-E13A-D48A double mutant variant (left column) co-expressed with mCh-wtPYD, mCh-PYD-E13A, mCh-PYD-D48A and mCh-PYD-E13A-D48A variants (middle column), and merge (right column).

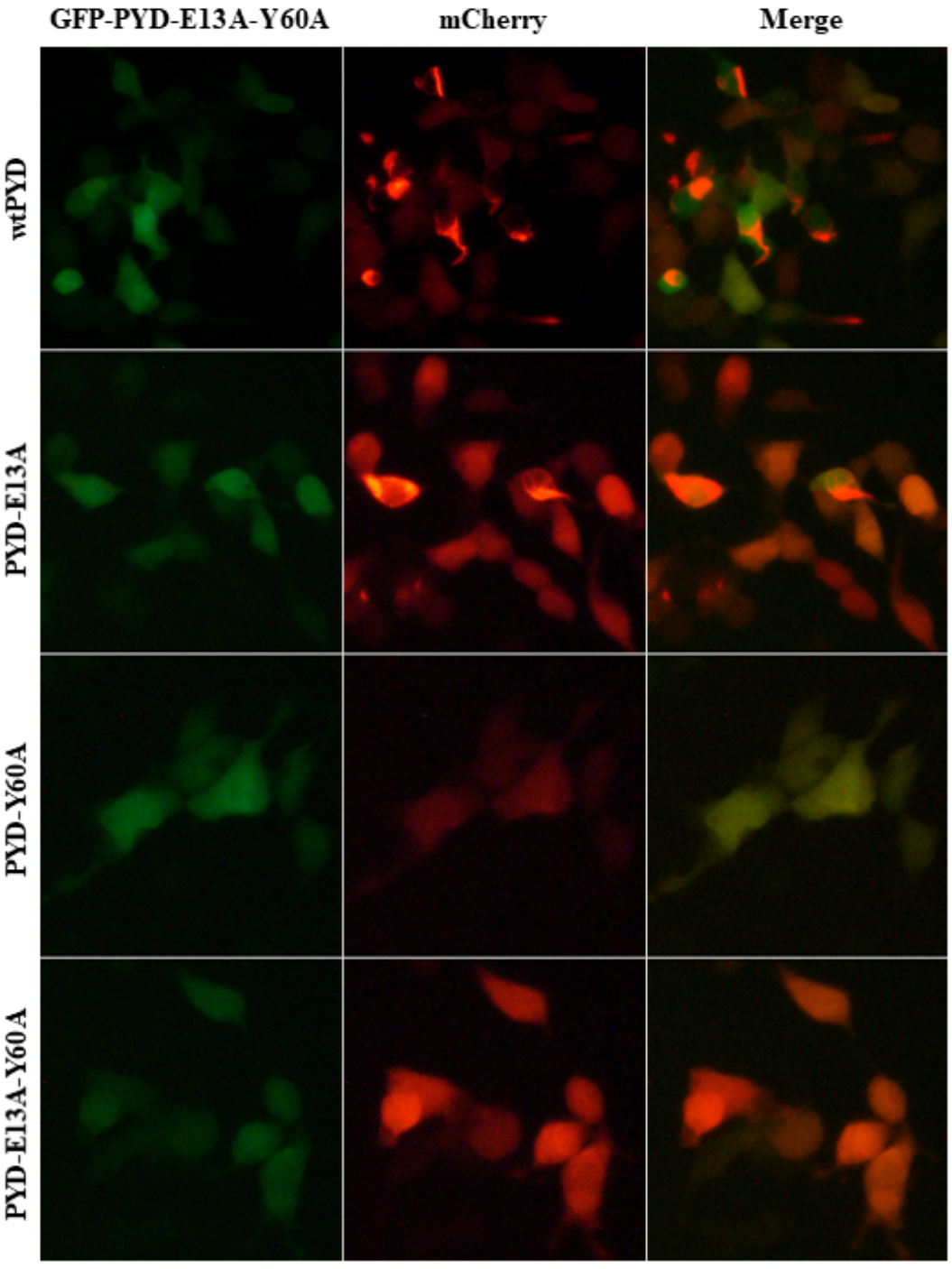

Figure 5.34. Fluorescent image set of EGFP-PYD-E13A-Y60A double mutant variant (left column) co-expressed with mCh-wtPYD, mCh-PYD-E13A, mCh-PYD-Y60A and mCh-PYD-E13A-Y60A variants (middle column), and merge (right column).

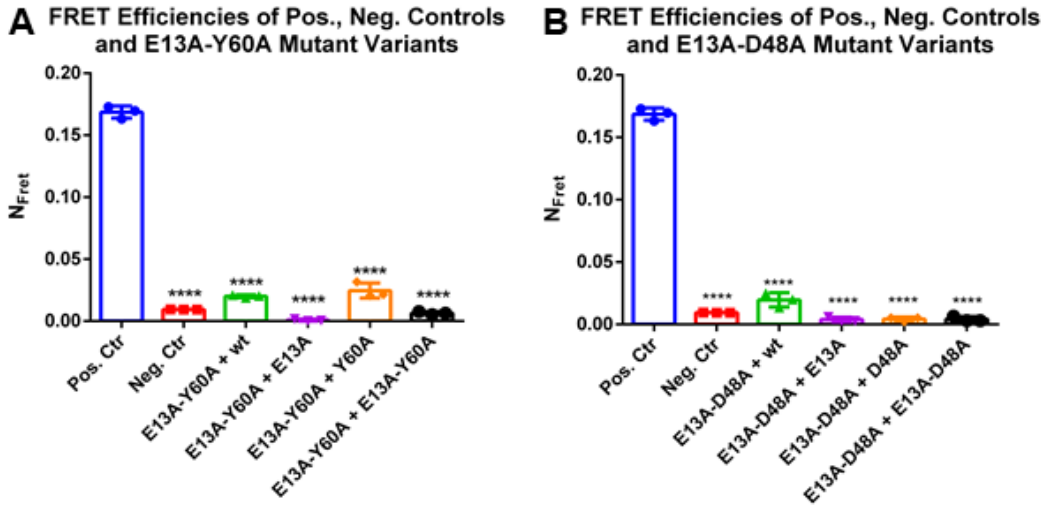

Figure 5.35. N_{FRET} graphs of (A) PYD-E13A-Y60A and (B) PYD-E13A-D48A double mutant sets.

5.9.2. Effects of Partially Shattering Mutations on Interaction

On PYD domain, double mutations showed 4 specific, partial patterns in which they showed either lower interaction rate more than two single variants, same interaction rate as lowest single mutant shows, middle interaction rate of two single mutants or similar interaction rates as wild type.

5.9.2.1. Double Mutant Shows Lower Interaction Efficiency Than Single Mutants. In the case, homooligomerization of double mutant variant with themselves resulted in lower interaction rate lower than with rate of single mutants.

In E13A-S29A case, interaction rate of the double mutant with wt was not affected due to presence of S29A on the other hand, double mutant oligomerization with itself was blocked significantly (Figure 5.36 and Figure 5.38 A).

In E67A-L85A case, double mutant-double mutant oligomerization rate was decreased more than rate of double mutant with other variants (Figure 5.37 and Figure 5.38 B).

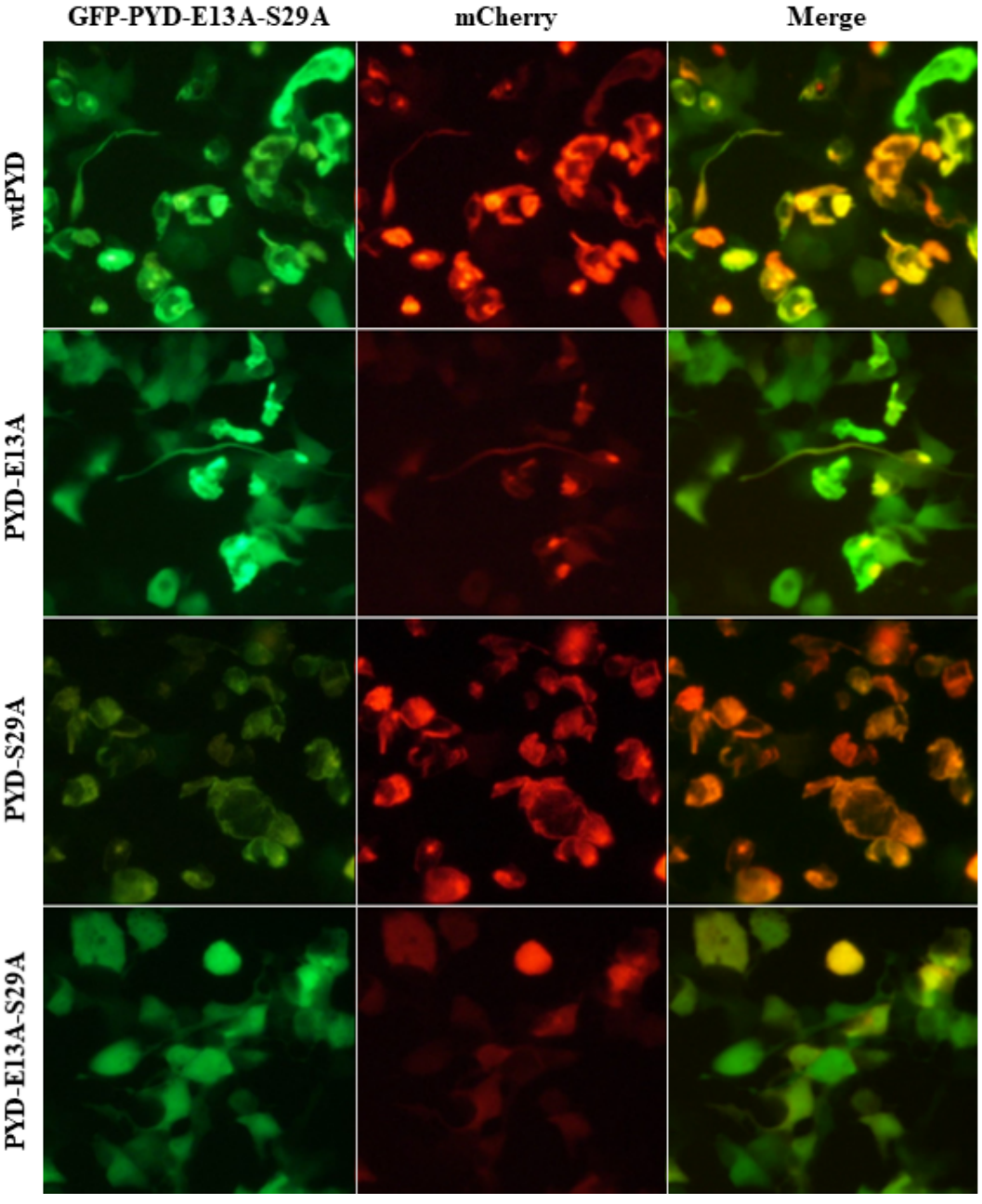

Figure 5.36. Fluorescent image set of EGFP-PYD-E13A-S29A double mutant variant (left column) co-expressed with mCh-wtPYD, mCh-PYD-E13A, mCh-PYD-S29A and mCh-PYD-E13A-S29A variants (middle column), and merge (right column).

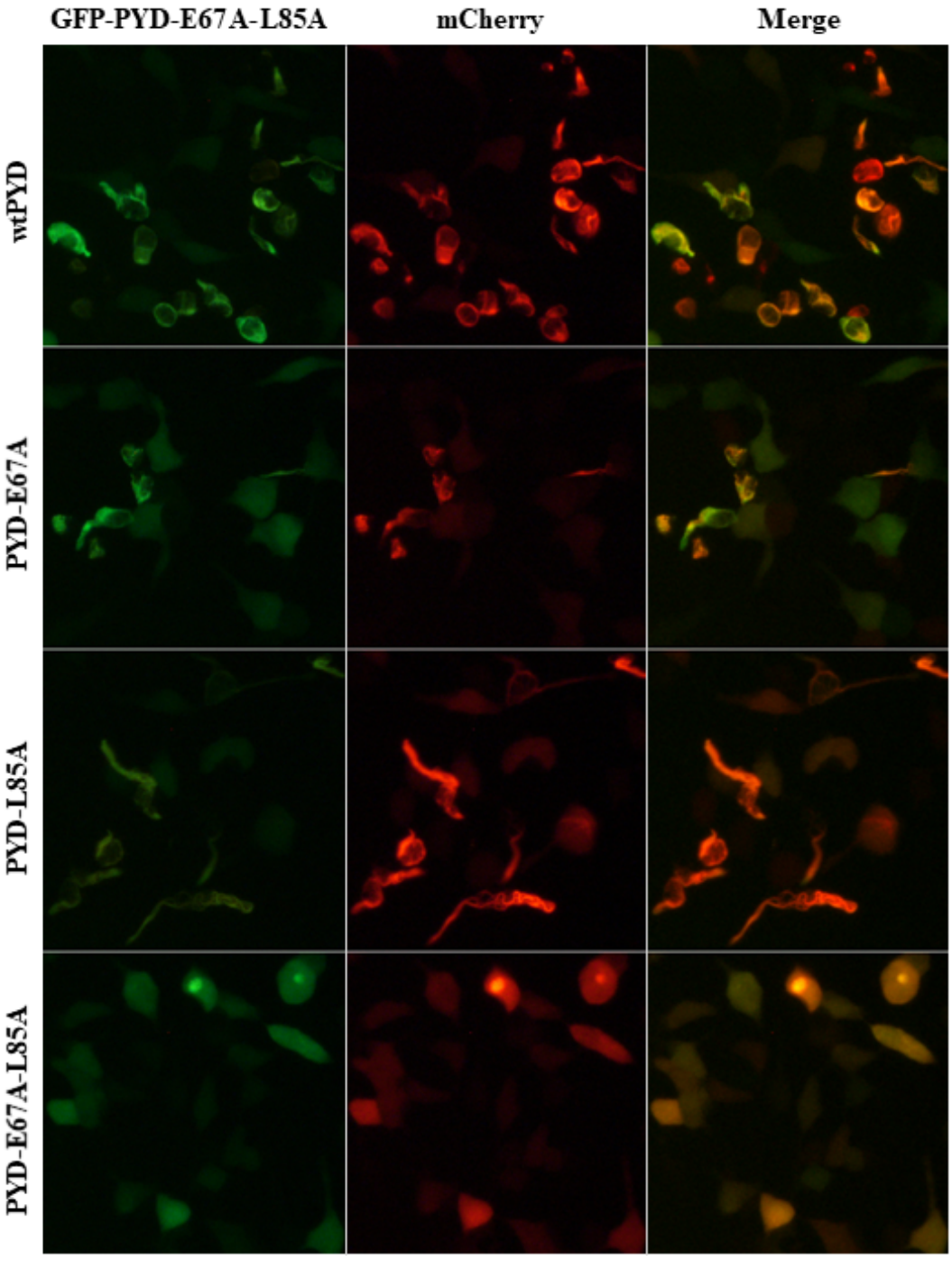

Figure 5.37. Fluorescent image set of EGFP-PYD-E67A-L85A double mutant variant (left column) co-expressed with mCh-wtPYD, mCh-PYD-E67A, mCh-PYD-L85A and mCh-PYD-E67A-L85A variants (middle column), and merge (right column).

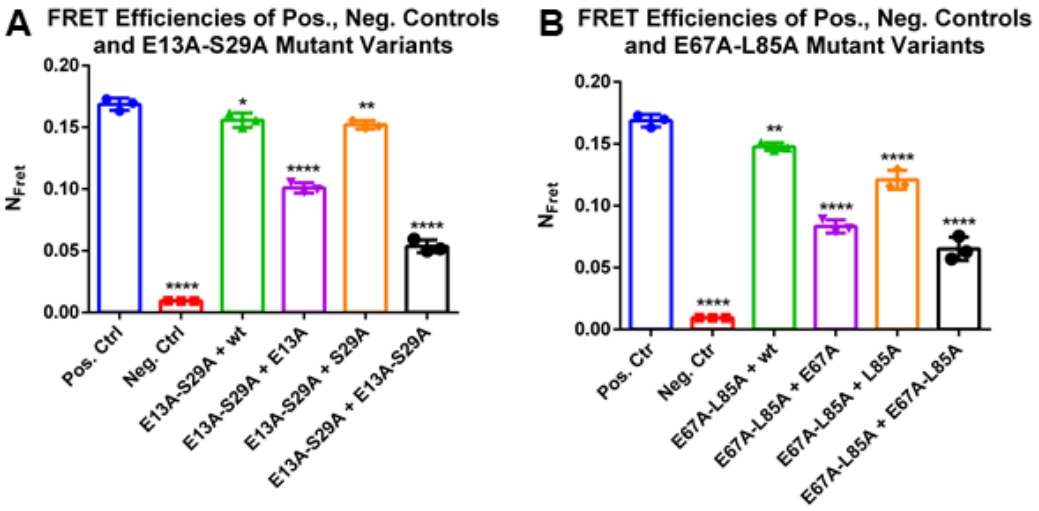

Figure 5.38. N_{FRET} graphs of (A) PYD-E13A-S29A and (B) PYD-E67A-L85A double mutant sets.

5.9.2.2. Double Mutant Shows Same Interaction Rate as Lowest Single Mutant. In the case, interaction rate of double mutants with same double mutant variant showed the effects of the interaction rate as lowest single mutant.

In E13A-L85A case, wt and L85A single mutations showed decreased co- localization with the double mutant separately, E13A and double mutant itself variant showed same results in interaction rate with the double mutant (Figure 5.39 and Figure 5.41 A). Blockage of L85 alone did not affect but when combined with E13, the effect was completely disruptive.

In L25A-T53A case, T53A mutation mostly saved the effects of the double mutant both in interaction with wt and T53A single mutant on the other hand, when combined with L25A, interaction rates were slightly decreased (Figure 5.40 and 5.41 B).

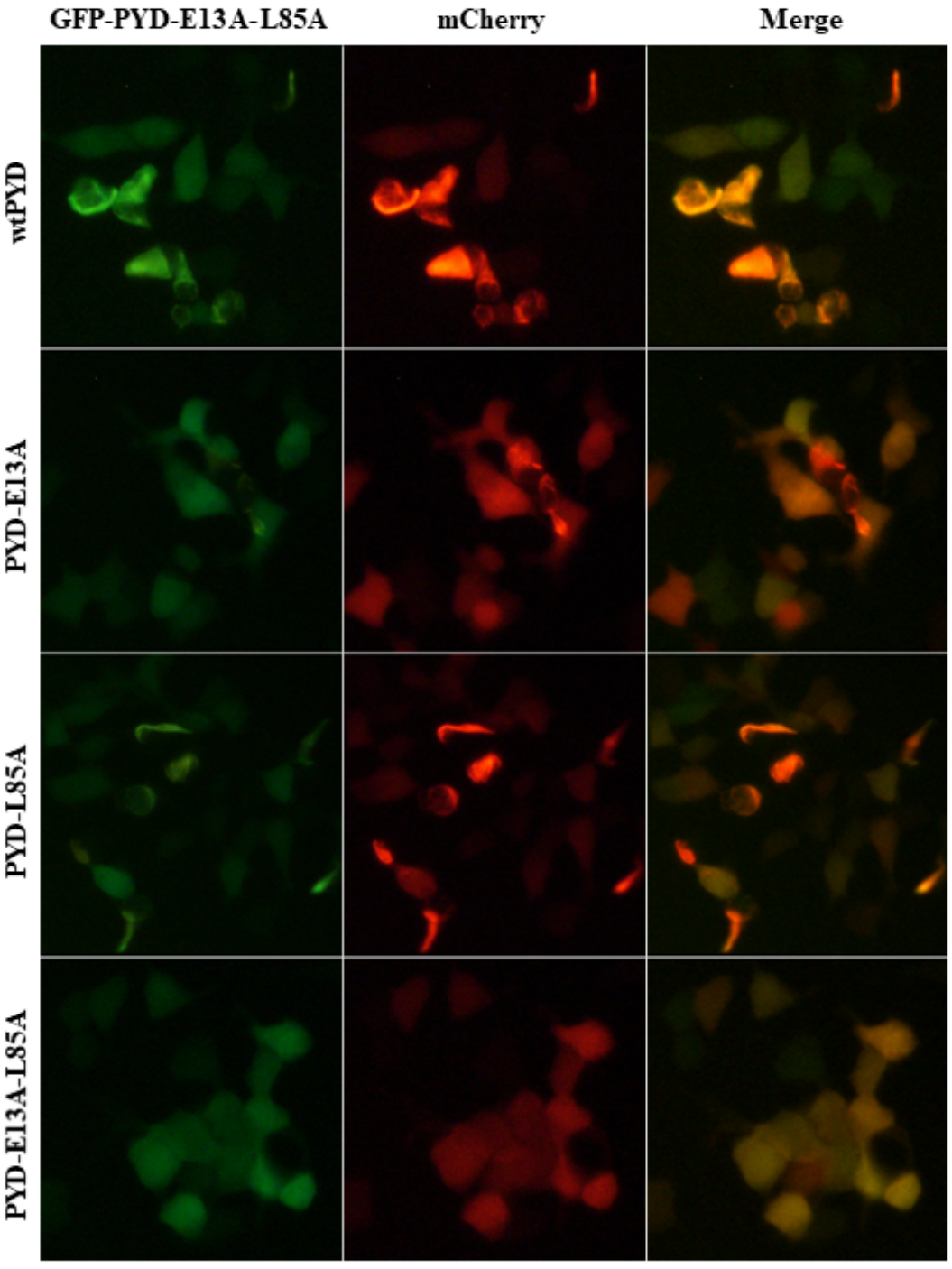

Figure 5.39. Fluorescent image set of EGFP-PYD-E13A-L85A double mutant variant (left column) co-expressed with mCh-wtPYD, mCh-PYD-E13A, mCh-PYD-L85A and mCh-PYD-E13A-L85A variants (middle column), and merge (right column).

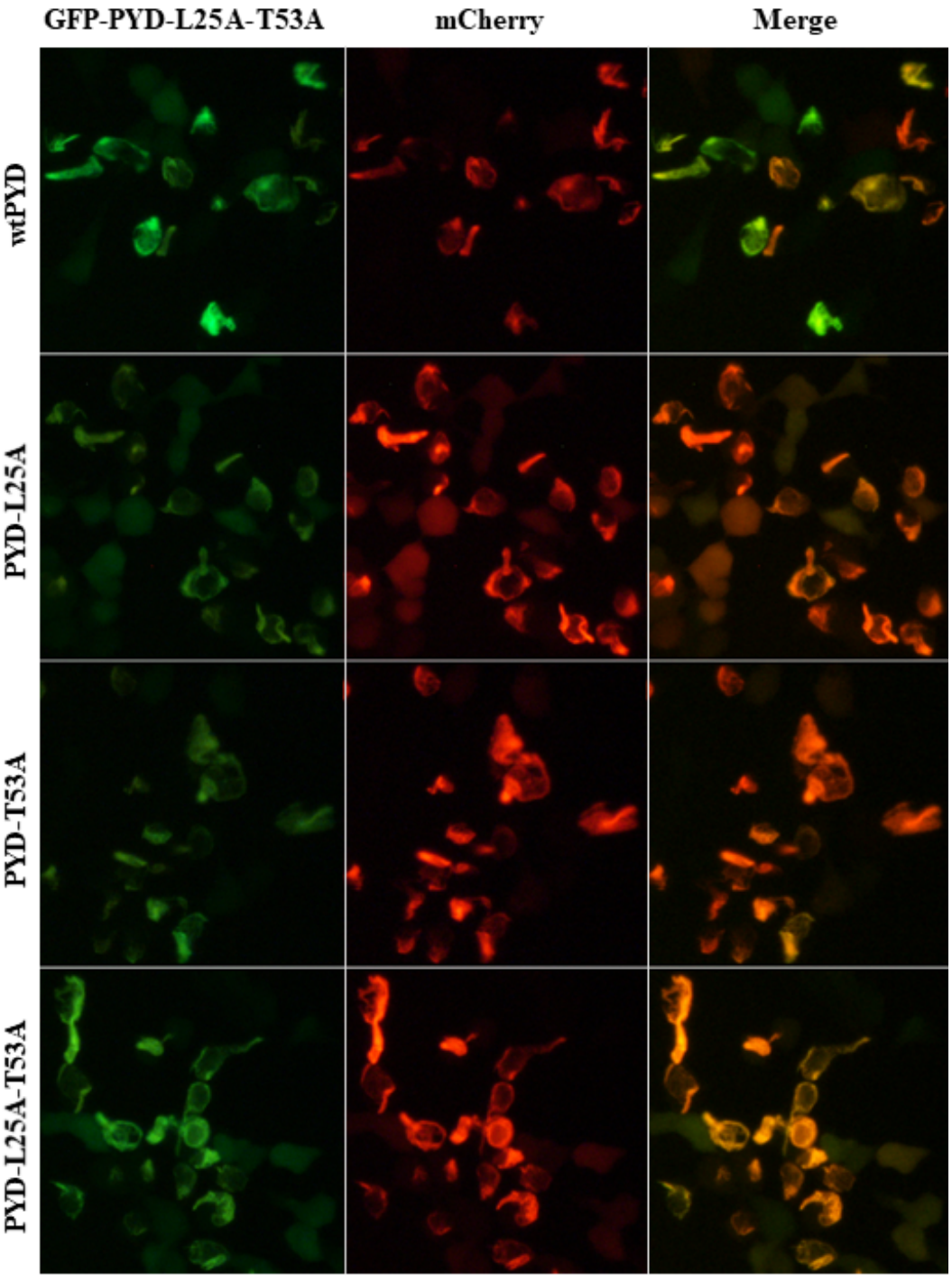

Figure 5.40. Fluorescent image set of EGFP-PYD-L25A-T53A double mutant variant (left column) co-expressed with mCh-wtPYD, mCh-PYD-L25A, mCh-PYD-T53A and mCh-PYD-L25A-T53A variants (middle column), and merge (right column).

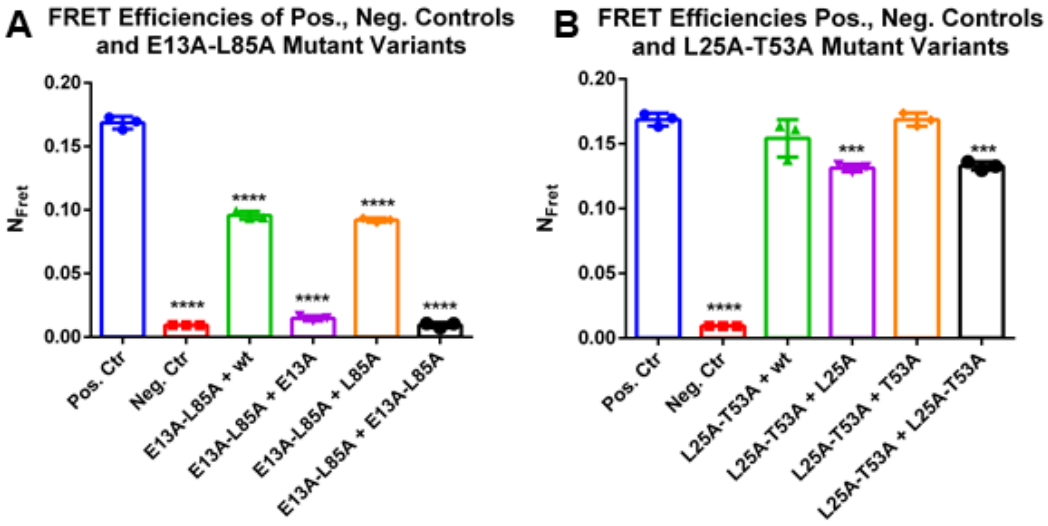

Figure 5.41. N_{FRET} graphs of (A) PYD-E13A-L85A and (B) PYD-L25A-T53A double mutant sets.

5.9.2.3. Double Mutant Shows Medium Interaction Between Two Single Mutants. In the case, effects of double mutant were between effects of two single mutant variants. In T53A-Y60A case, double mutant was not observed to interact with other variants but, interaction rates showed a distribution in the rates of different combinations (Figure 5.42 and Figure 5.43 A). T53A mutation had enhancer role in interaction especially between double mutant and T53A single mutant. It also recovered the disruptive effect of Y60A mutation through which double mutant homooligomerization with itself gave more interaction rate than double mutant homooligomerization with Y60A.

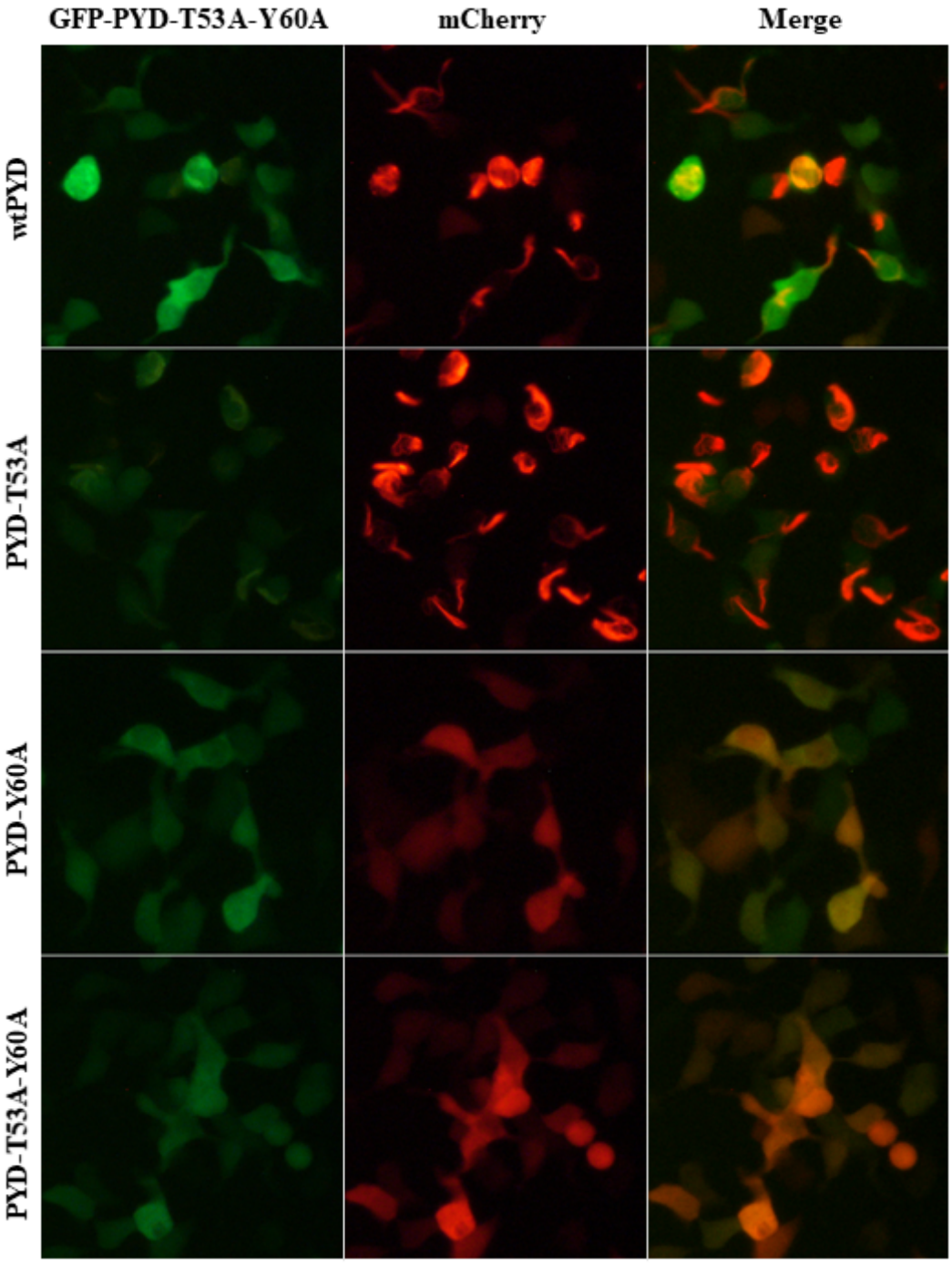

Figure 5.42. Fluorescent image set of EGFP-PYD-T53A-Y60A double mutant variant (left column) co-expressed with mCh-wtPYD, mCh-PYD-T53A, mCh-PYD-Y60A and mCh-PYD-T53A-Y60A variants (middle column), and merge (right column).

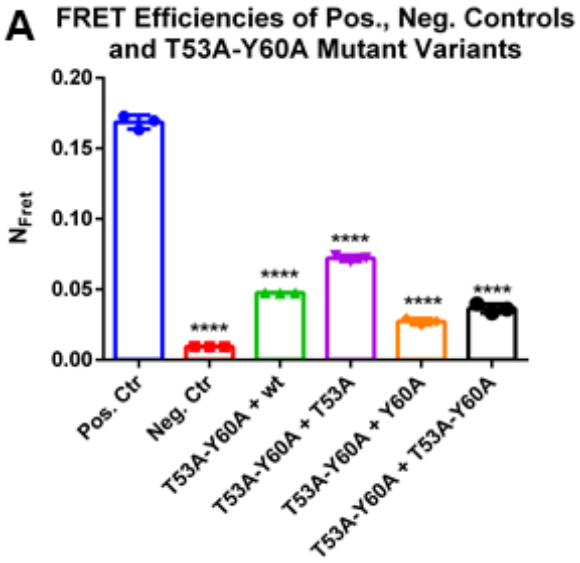

Figure 5.43. N_{FRET} graph of (A) PYD-T53A-Y60A double mutant set.

5.9.2.4. Double Mutant Shows Similar Interaction Rate as Wild Type. In that case, effects of double mutant were similar with wild type.

In L25A-S29A case, neither single mutants nor double mutant blocked homooligomerization between the variants (Figure 5.44 and Figure 5.45 A). The changes were not in disruptive manner. L25A is located on Type 1b and S29A is located on near Type 1b interaction surface both on Helix 2 on the other hand, even being on Type 1 interaction surface was not enough to block interaction between the variants.

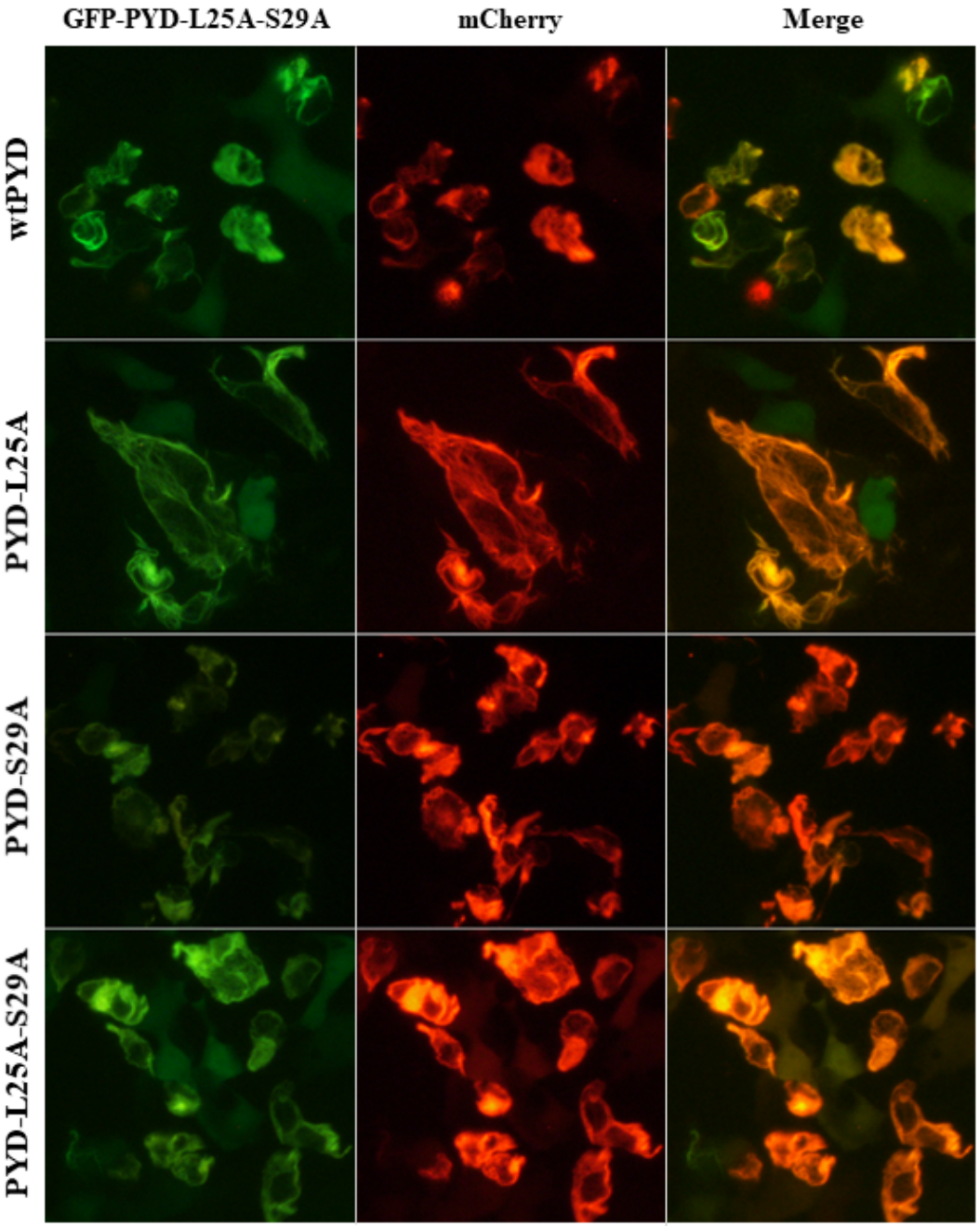

Figure 5.44. Fluorescent image set of EGFP-PYD-L25A-S29A double mutant variant (left column) co-expressed with mCh-wtPYD, mCh-PYD-L25A, mCh-PYD-S29A and mCh-PYD-L25A-S29A variants (middle column), and merge (right column).

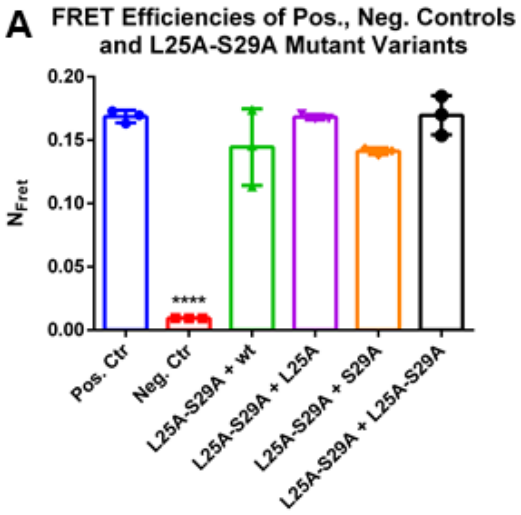

Figure 5.45. N_{FRET} graph of (A) PYD-L25A-S29A double mutant set.

5.10. Effects of Double Mutations on CARD Variants

Effects of double mutants on dynamics of CARD homooligomerization was observed by co-transfection of EGFP-CARD double mutants with either mCherry- wt-CARD or mCherry-CARD double mutant variants to HEK293FT cells. Effects of 14 different double mutant sets were observed including 4 sub-sets for each of them.

Introduction of double mutations over the selected single mutants provided us to analyze the effects of inhibition for two interaction surfaces at same time in a combinational manner. Average emission spectra for each triplicate sample can be found in Figure A.10, Figure A.11, Figure A.12, Figure A.13, Figure A.14, Figure A.15 and Figure A.16.

5.10.1. Completely Disruptive Mutations Block Interaction

On CARD domain, 6 of the double mutants showed soluble phenotype especially when double mutants were co-expressed. E130A-Y146 double mutant did not interacted with any of other mutant variants but double mutant-wt sub-set showed slight

interaction meaning that the double mutant could interact with wt very slightly but inhibited further localizations of other variants (Figure 5.46 and Figure 5.52 A). Here, Type 1b - Type 1b blockage resulted in inhibition case.

In E130A-M159A set, while the double mutant remained soluble, some minor filaments were formed in wt-wt and E130A-E130A variants, but the double mutant could not interact with these (Figure 5.47 and Figure 5.52 B). M159 residue extends its side chain inward of the protein and the change thoroughly caused both the double mutant and M159A single mutant variant to neither co-localize nor inhibit.

In E130A-W169A set, while the double mutant did not interact with wt, wt-wt interaction remained as filament. E130A single mutant also showed minor filamentous structures but W169A mutation did not show any filaments and the interaction rates were close to negative control (Figure 5.48 and 5.52 C). Inhibition of Type 1b and Type 2a caused disruption of the interaction.

In E152A-M159A, double mutant failed to interact with other variants but wt-wt interaction and minor E15A single mutant self-oligomerization was observed. M159A single mutant was unable to both self-oligomerize and interact with the double mutant (Figure 5.49 and Figure 5.52 D). while inhibition of Type 3b affected the interaction, effect of M159A mutation was dominant to see the neither co-localization, nor-inhibition phenotype.

In E152A-W169A set, double mutant could not interact with other variants. self-oligomerization of wt variants was observed but double mutant did not contribute to this organization. Also, while E152A variant slightly self-oligomerize, it did not show any co-localization with the double mutant (Figure 5.50 and Figure 5.52 E). Inhibition of Type 3b and Type 2a interaction surfaces resulted in soluble phenotype for the double mutant and Type 1 interaction could not recover these effects.

In W169A-R182A set, wt self-oligomerization showed minor filaments but interaction with the double mutant was not observed. Also, presence of W169A mutation

prevented the interaction between the variants (Figure 5.51 and Figure 5.52 F). R182A single mutant showed reduced co-localization.

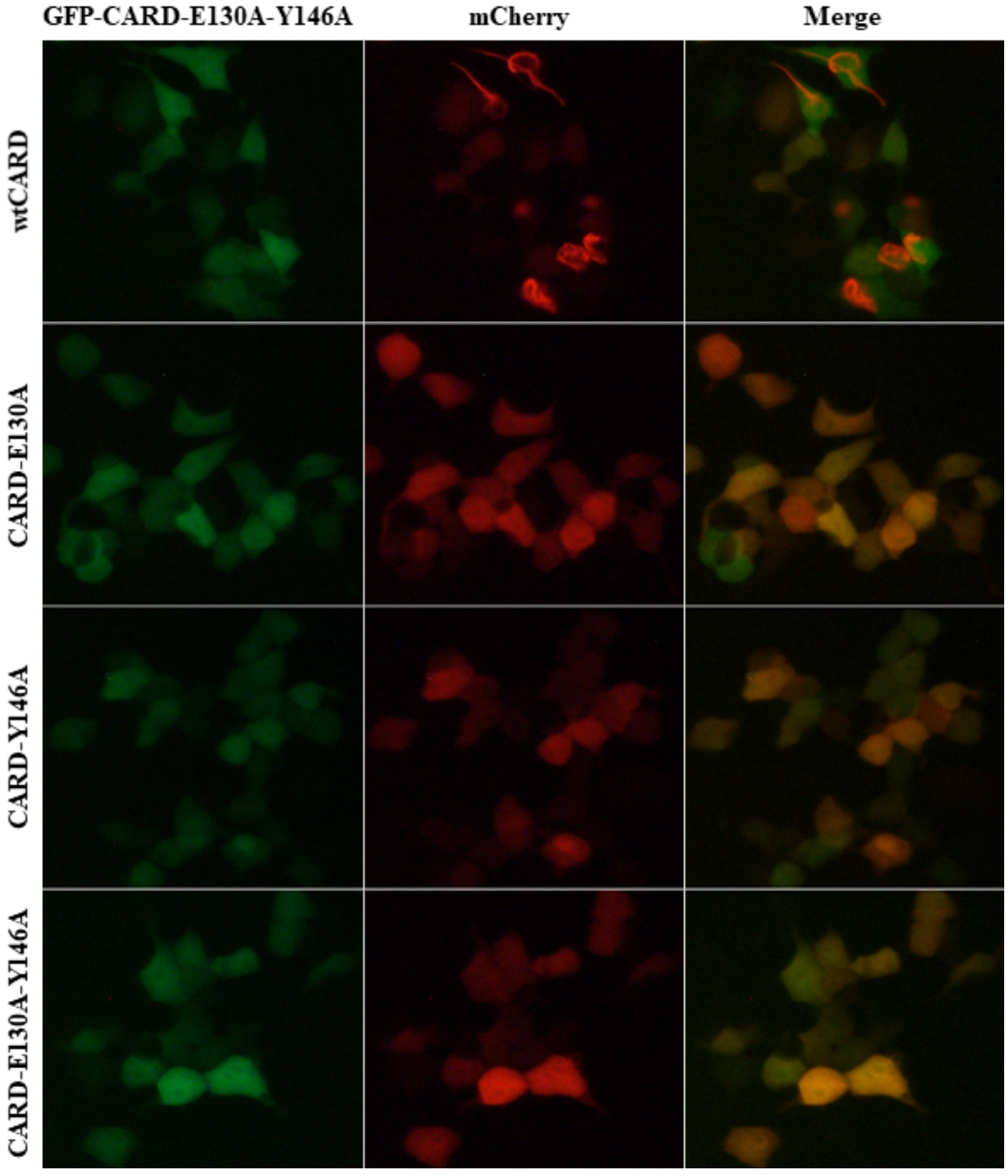

Figure 5.46. Fluorescent image set of EGFP-CARD-E130A-Y146A double mutant variant (left column) co-expressed with mCh-wtCARD, mCh-CARD-E130A, mCh-CARD-Y146A and mCh-CARD-E130A-Y146A variants (middle column), and merge (right column).

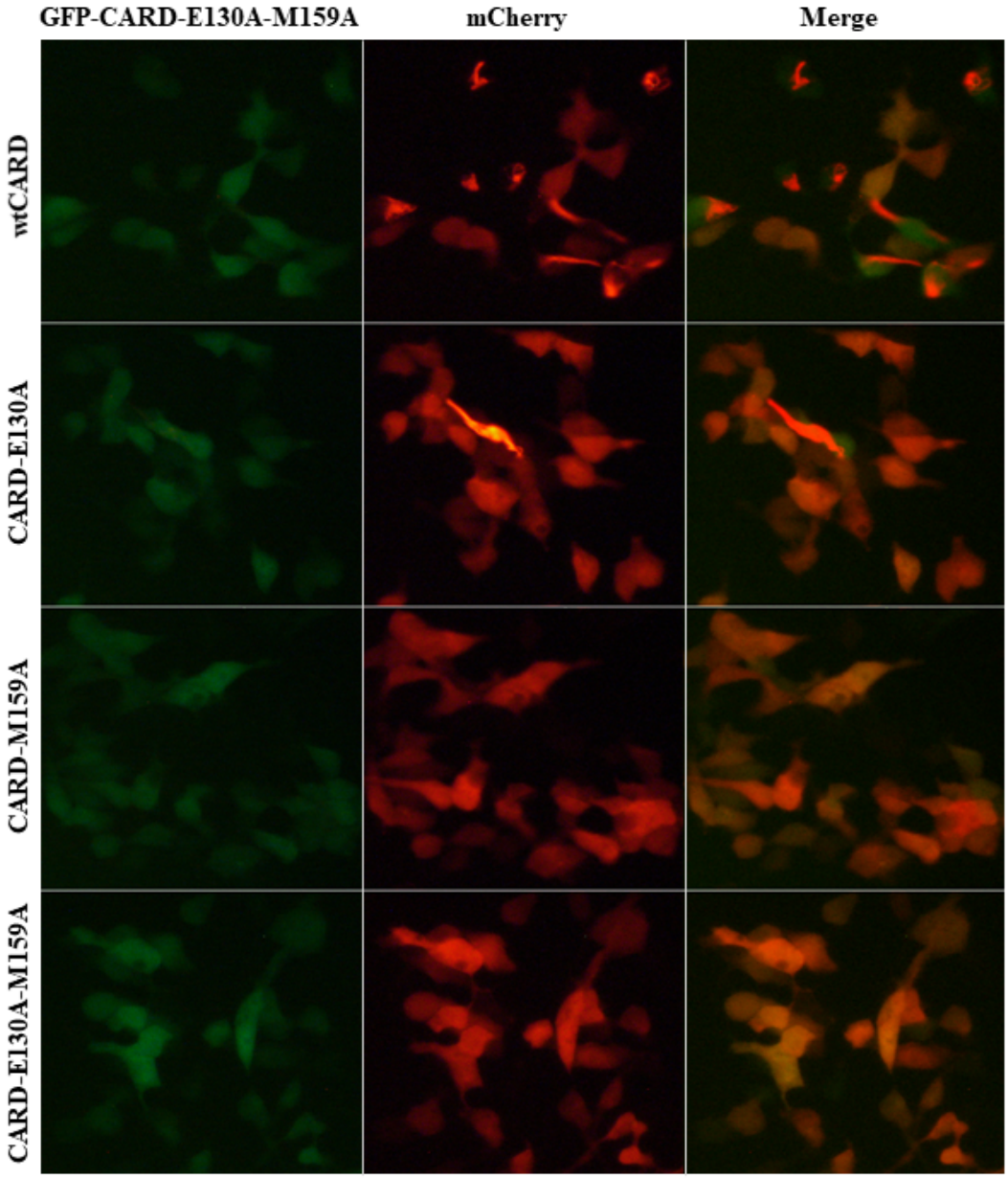

Figure 5.47. Fluorescent image set of EGFP-CARD-E130A-M159A double mutant variant (left column) co-expressed with mCh-wtCARD, mCh-CARD-E130A, mCh-CARD-M159A and mCh-CARD-E130A-M159A variants (middle column), and merge (right column).

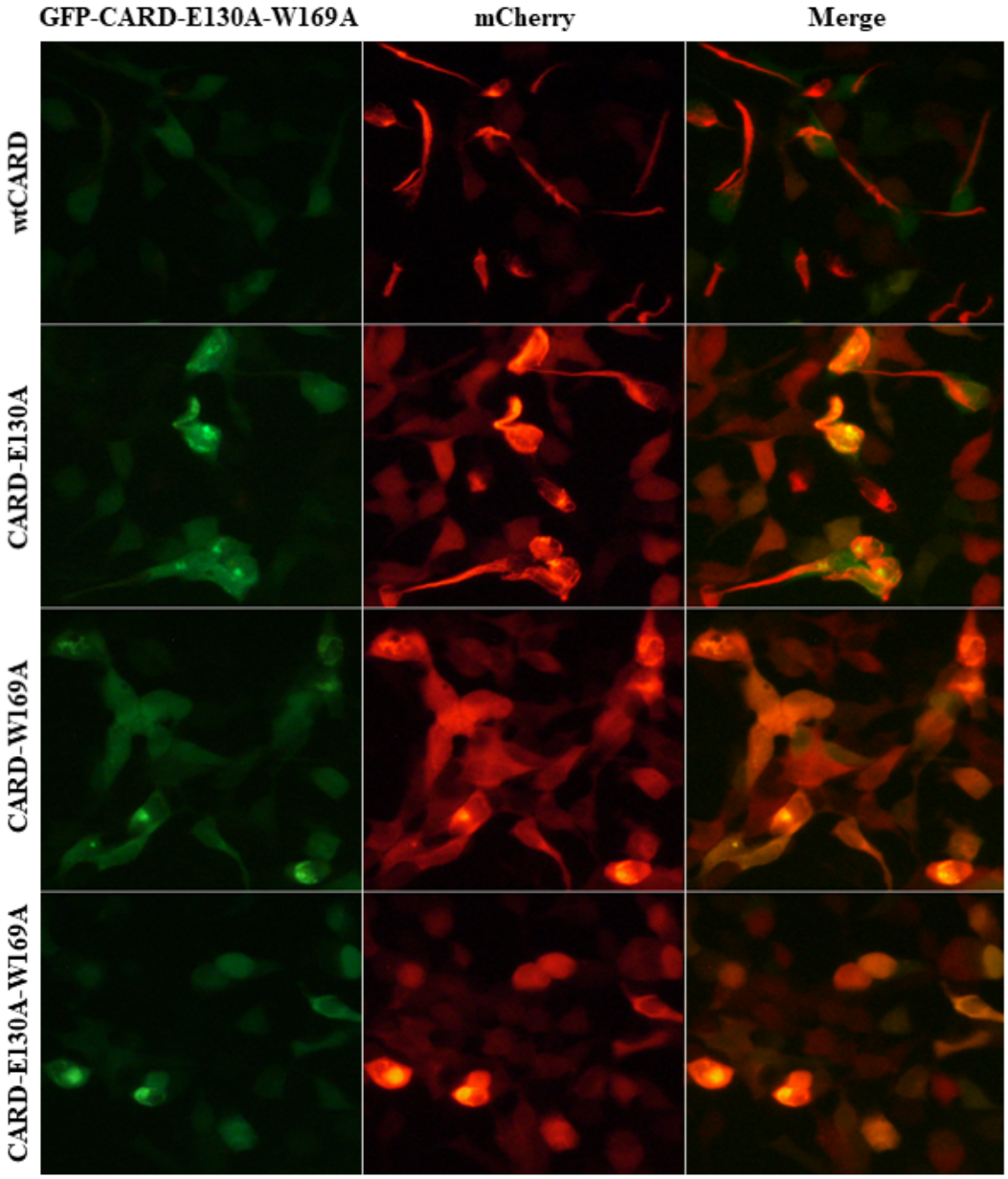

Figure 5.48. Fluorescent image set of EGFP-CARD-E130A-W169A double mutant variant (left column) co-expressed with mCh-wtCARD, mCh-CARD-E130A, mCh-CARD-W169A and mCh-CARD-E130A-W169A variants (middle column), and merge (right column).

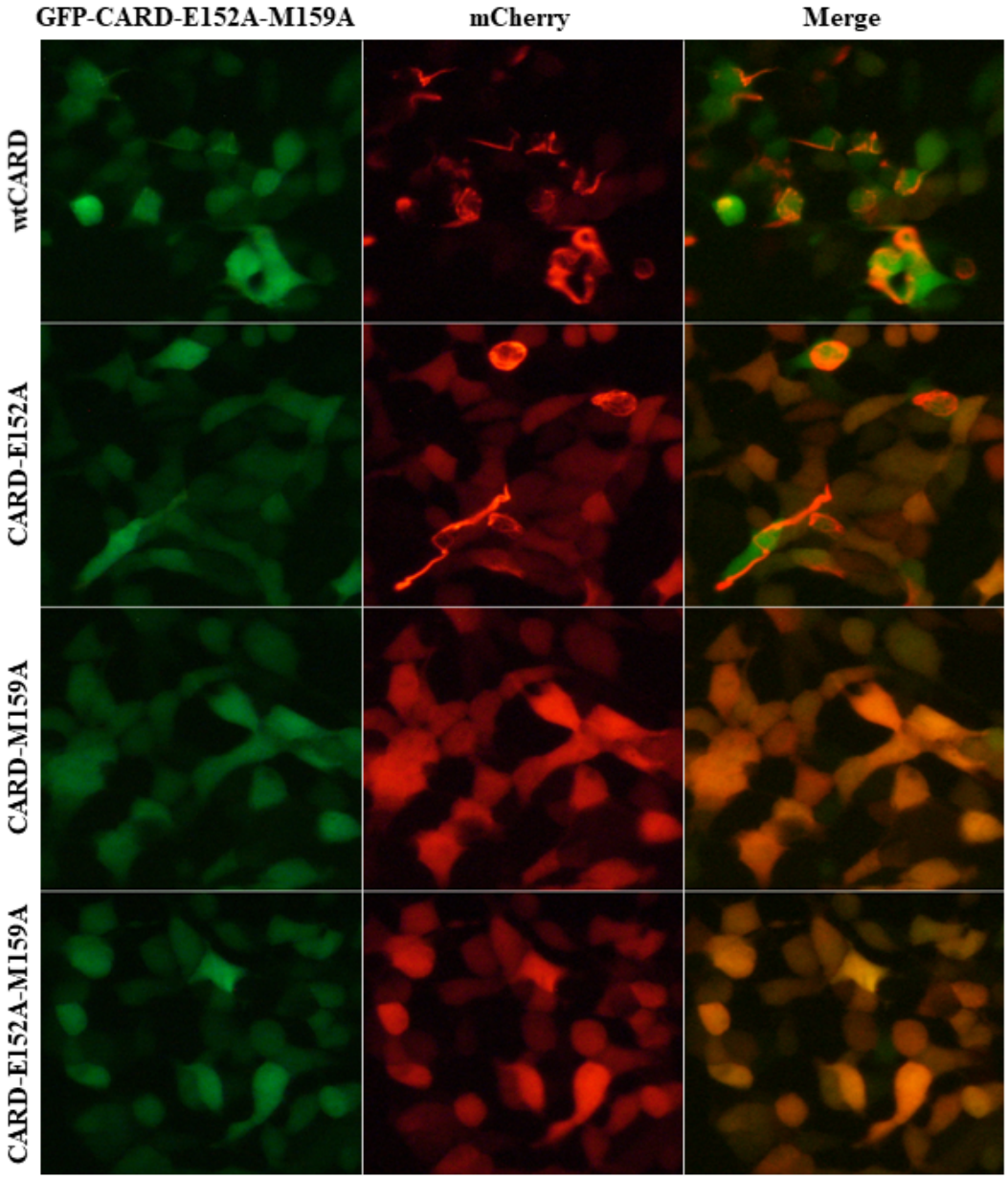

Figure 5.49. Fluorescent image set of EGFP-CARD-E152A-M159A double mutant variant (left column) co-expressed with mCh-wtCARD, mCh-CARD-E152A, mCh-CARD-M159A and mCh-CARD-E152A-M159A variants (middle column), and merge (right column).

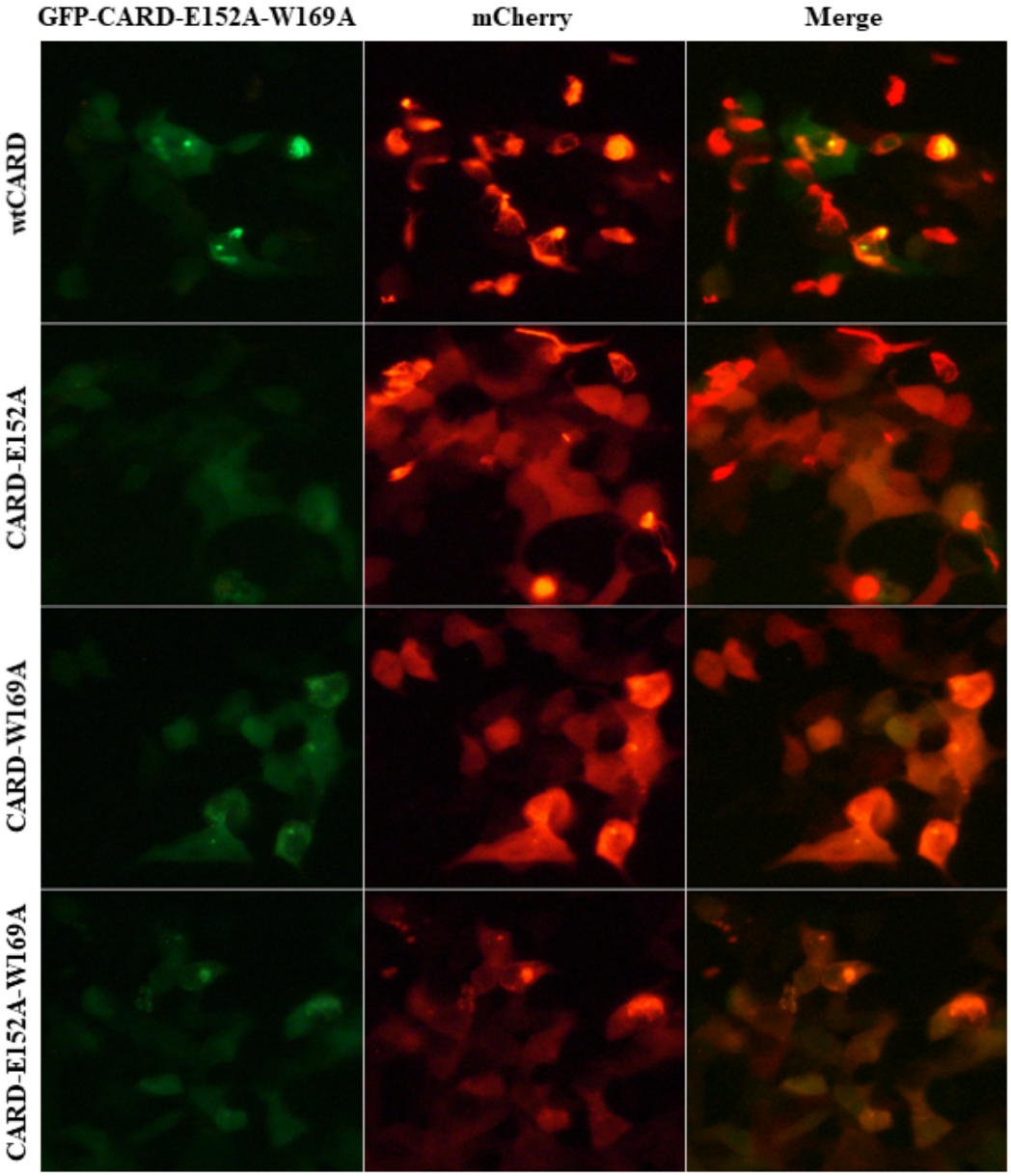

Figure 5.50. Fluorescent image set of EGFP-CARD-E152A-W169A double mutant variant (left column) co-expressed with mCh-wtCARD, mCh-CARD-E152A, mCh-CARD-W169A and mCh-CARD-E152A-W169A variants (middle column), and merge (right column).

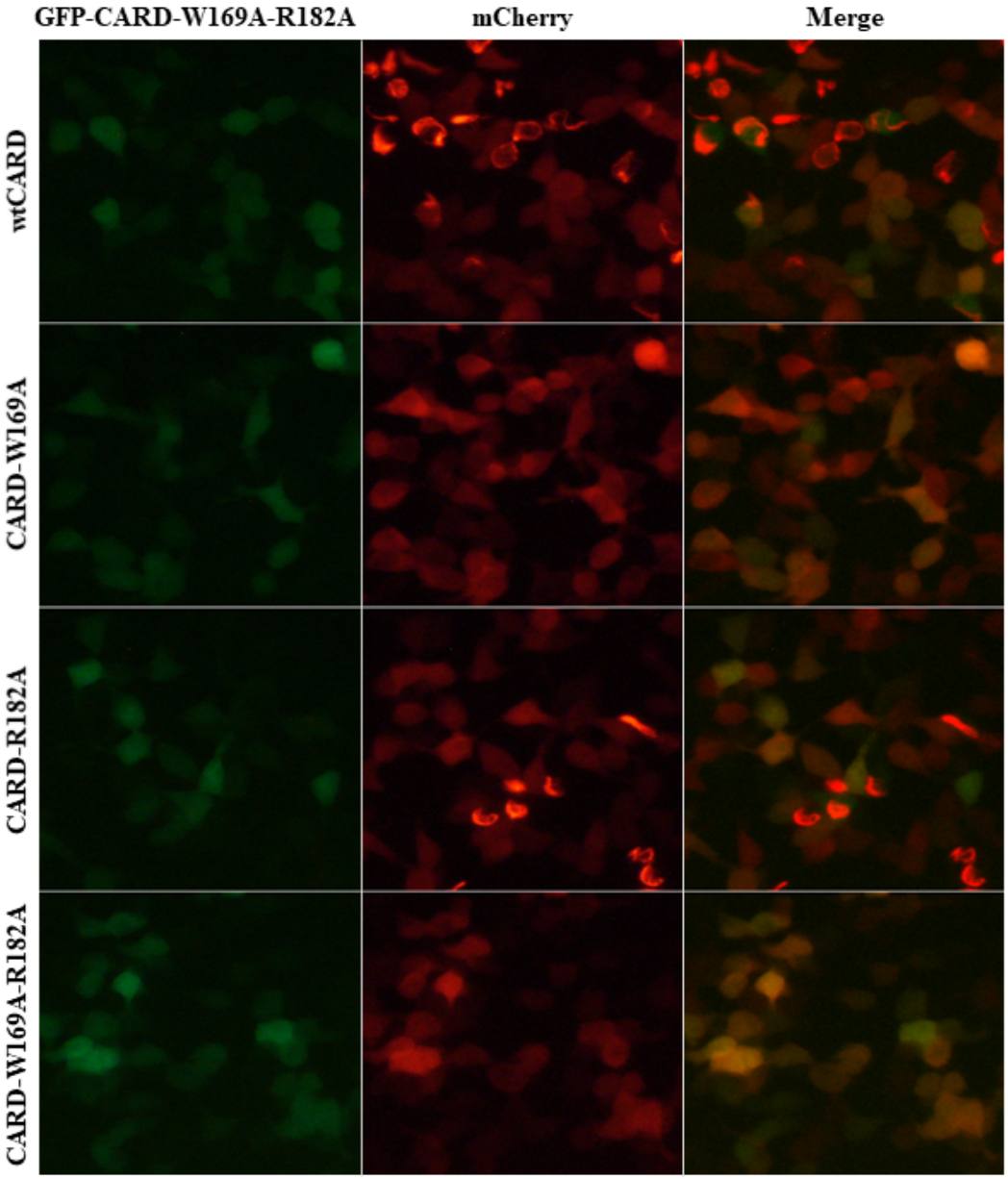

Figure 5.51. Fluorescent images set of EGFP-CARD-W169A-R182A double mutant variant (left column) co-expressed with mCh-wtCARD, mCh-CARD-W169A, mCh-CARD-R182A and mCh-CARD-W169A-R182A variants (middle column), and merge (right column).

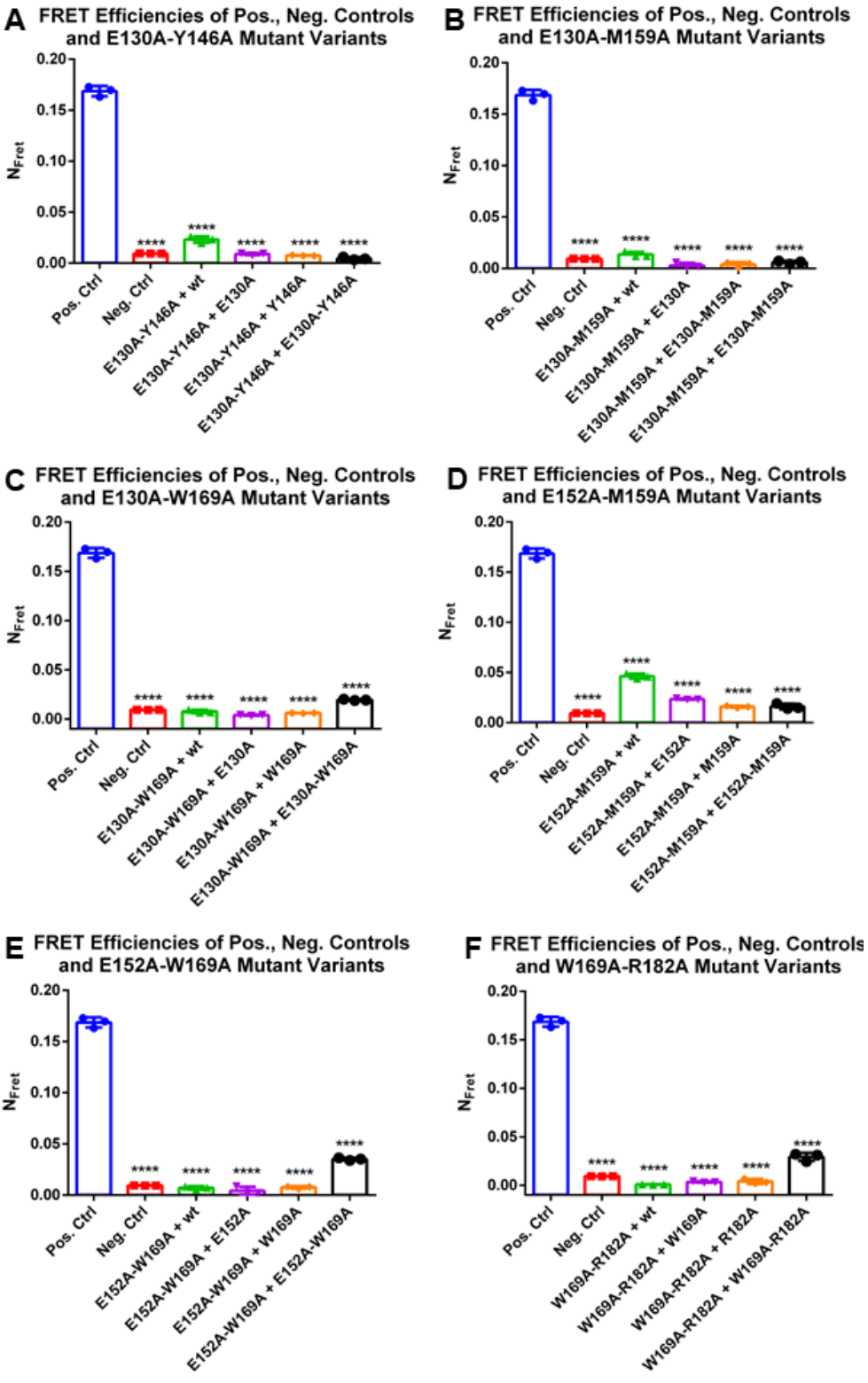

Figure 5.52. N_{FRET} graphs of (A) CARD-E130A-Y146A, (B) CARD-E130A-M159A, (C) CARD-E130A-W169A, (D) CARD-E152A-M159A, (E) CARD-E152A-W169A and (F) CARD-W169A-R182A double mutant sets.

5.10.2. Partially Destructive Mutations on Interaction

On CARD domain, double mutations showed 3 partially interaction patterns in which they either have lower interaction rate than single mutant variants, similar interaction rate as the lowest single mutant variant and middle interaction rate between rates of two single mutant variants.

5.10.2.1. Double Mutants Show Lower Interaction Rate Than Two Single Mutants. In the case, interaction rate of the double mutant was observed below the lowest single mutant interaction rate.

In E130A-E152A set, the double mutant could co-localize with wt and partially with E130A mutant. On the other hand, double mutant self-oligomerization was not observed (Figure 5.53 and Figure 5.57 A). Disruptive effect of E152A was higher than E130A but their total effects were much more disruptive when expressed together than separately.

In E130A-P156A set, double mutant showed reduced co-localization with wt and P156A mutant but failed to self-oligomerize (Figure 5.54 and 5.57 B). Type 1b and Type 3b inhibition remained as soluble phenotype.

In E130A-R182A, the double mutant showed decreased co-localizations with wt, E130A and R182A single mutants but did not show any co-localization with itself (Figure 5.55 and Figure 5.57 C). Total effects of E130A and R182A were observed more disruptive than they are expressed individually.

In R150A-K158A, the variants showed co-localization up to a level but the disruptive effect was ranged in a interaction rate spectrum. The rate of interaction decreased as double mutant interacted with wt, K158A, R150A and the double mutant itself in that order (Figure 5.56 and Figure 5.57 D). Disruption of Type 1b was more disruptive than Type 3b in the case.

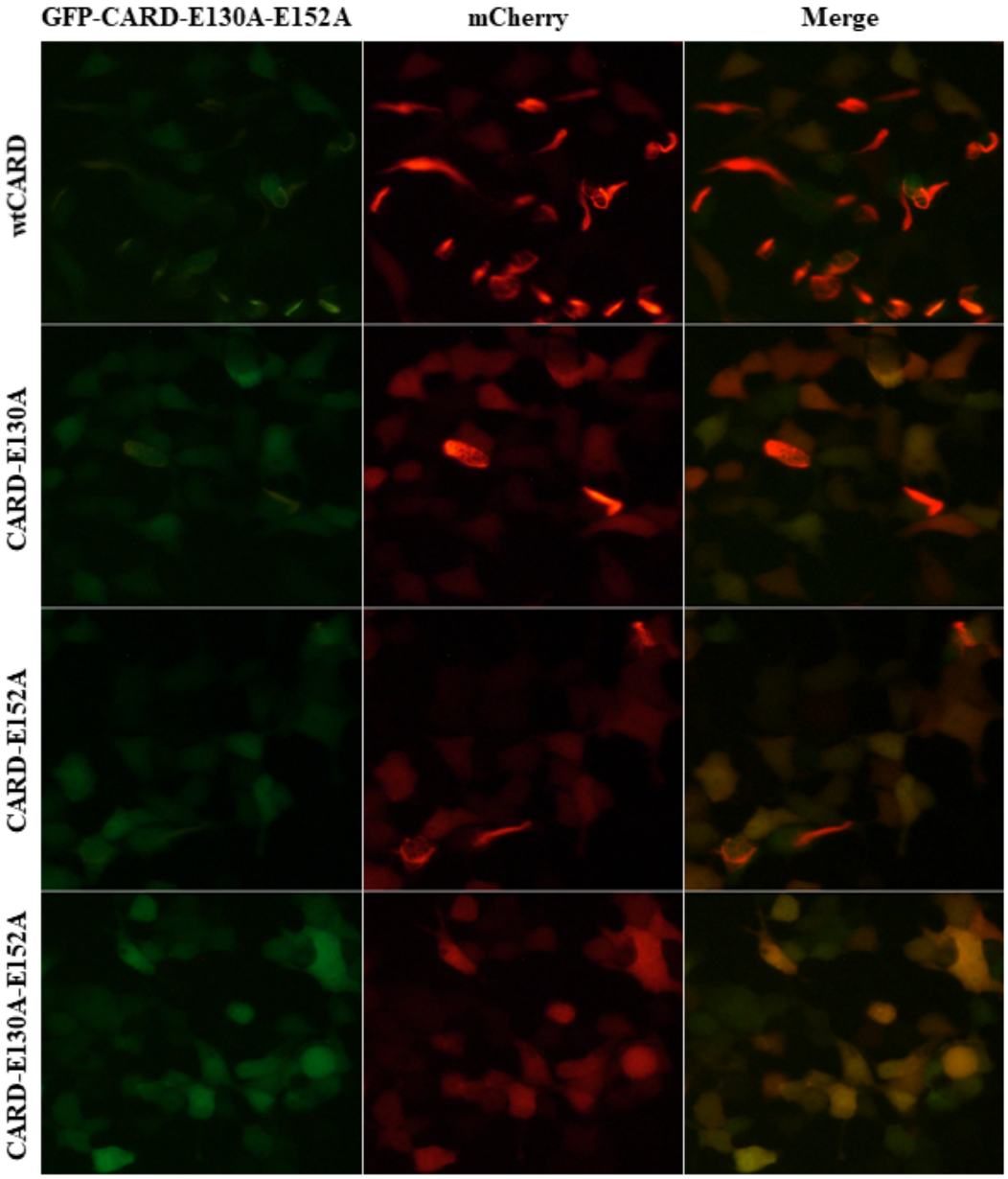

Figure 5.53. Fluorescent image set of EGFP-CARD-E130A-E152A double mutant variant (left column) co-expressed with mCh-wtCARD, mCh-CARD-E130A, mCh-CARD-E152A and mCh-CARD-E130A-E152A variants (middle column), and merge (right column).

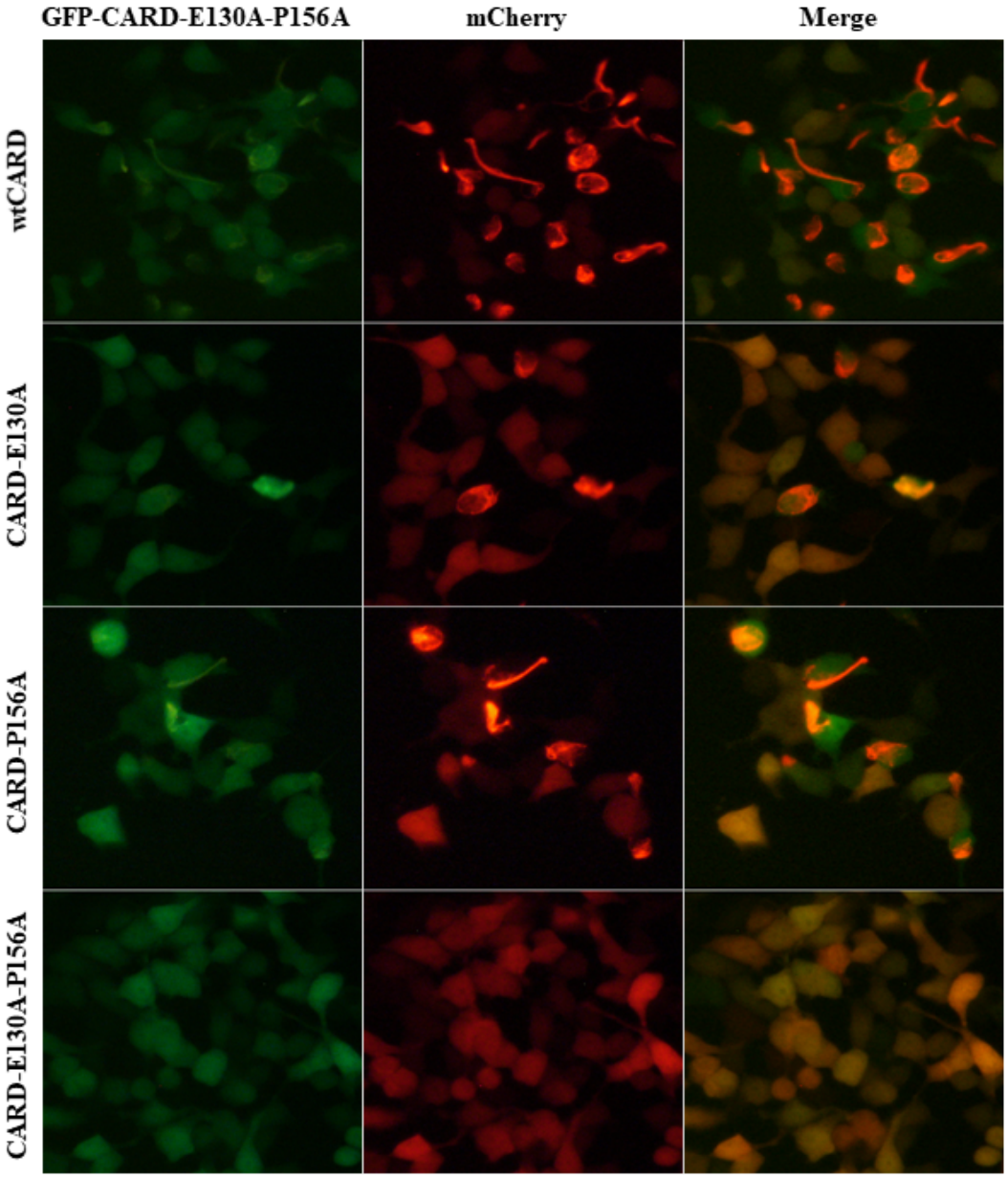

Figure 5.54. Fluorescent image set of EGFP-CARD-E130A-P156A double mutant variant (left column) co-expressed with mCh-wtCARD, mCh-CARD-E130A, mCh-CARD-P156A and mCh-CARD-E130A-P156A variants (middle column), and merge (right column).

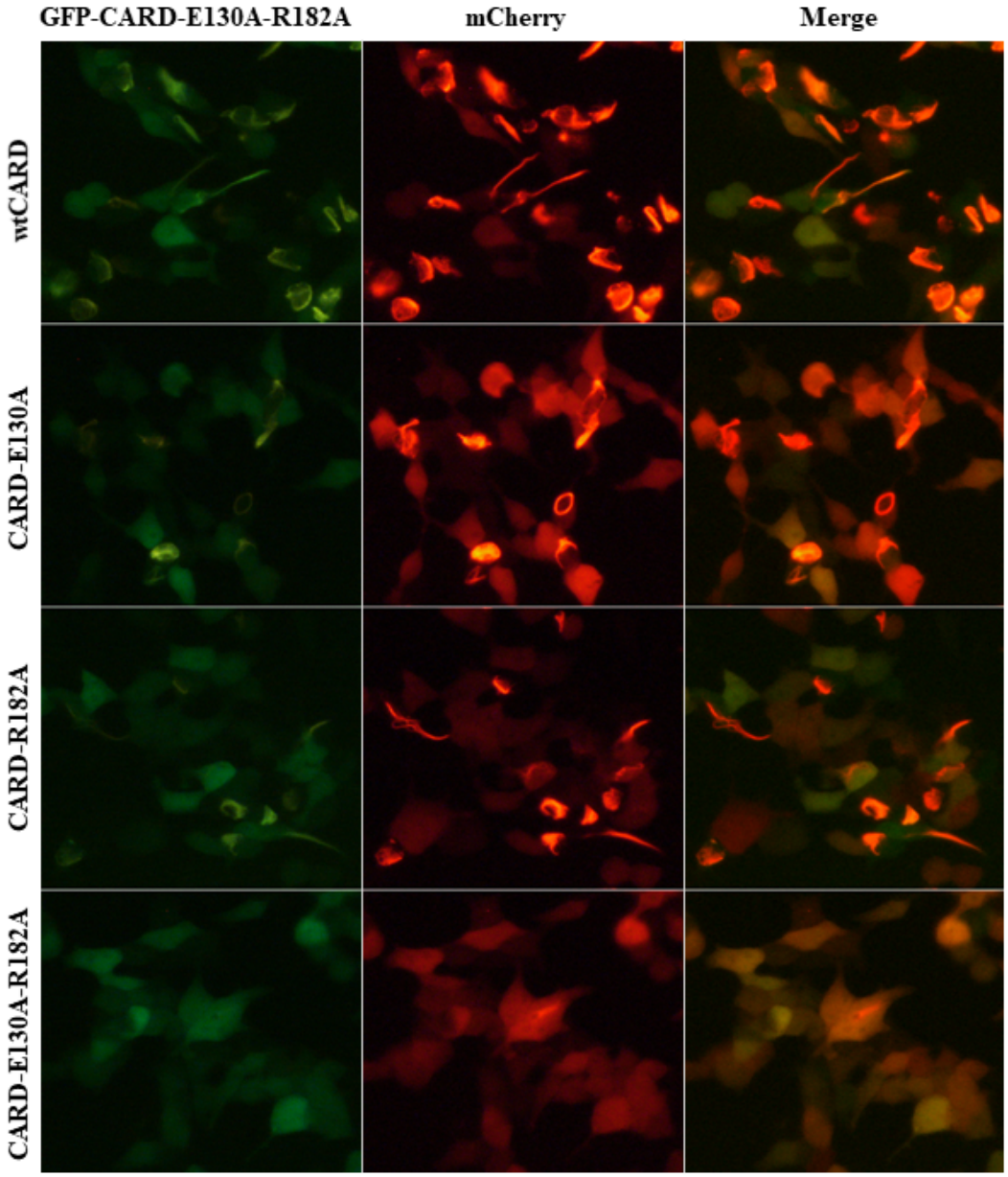

Figure 5.55. Fluorescent image set of EGFP-CARD-E130A-R182A double mutant variant (left column) co-expressed with mCh-wtCARD, mCh-CARD-E130A, mCh-CARD-R182A and mCh-CARD-E130A-R182A variants (middle column), and merge (right column).

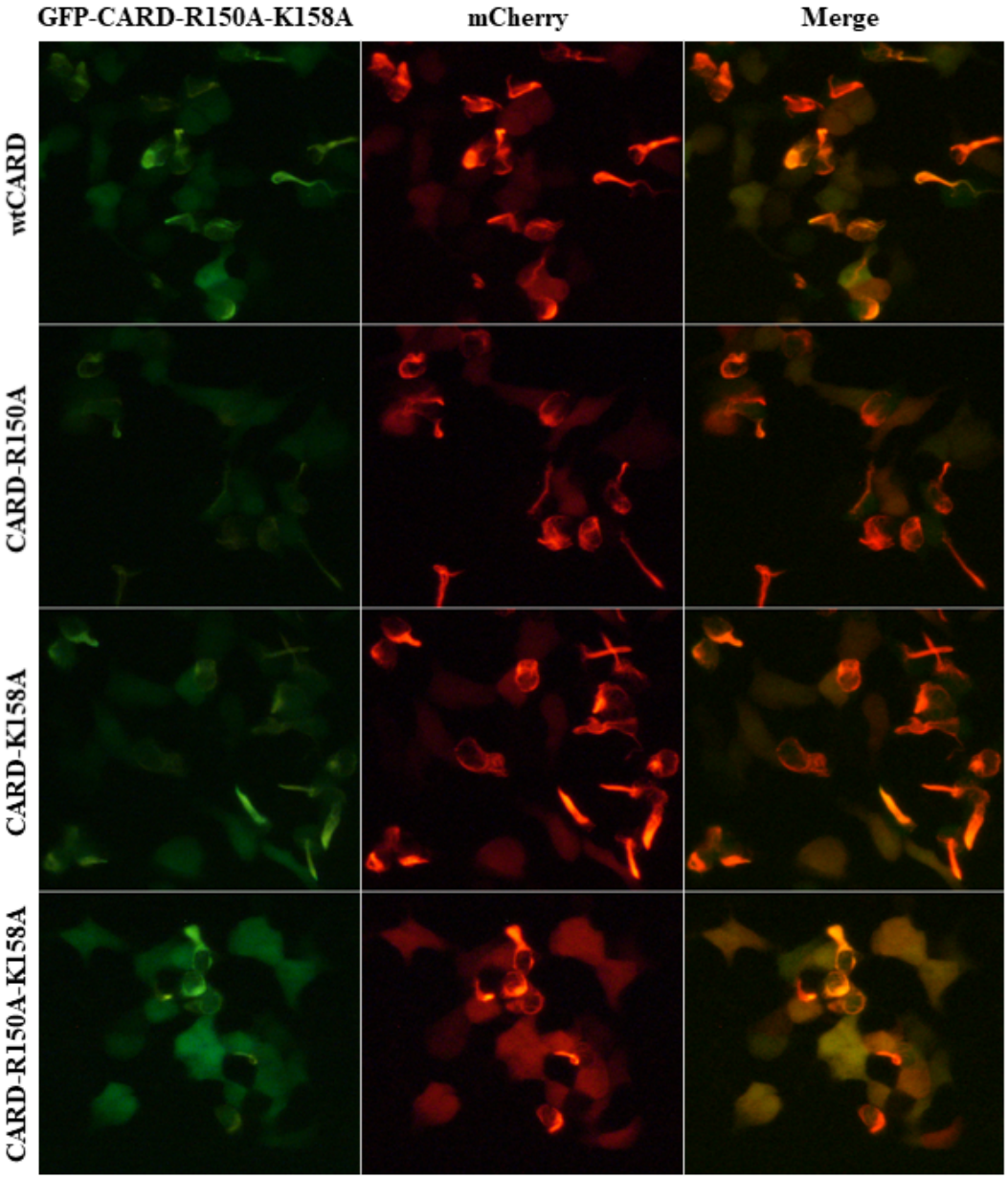

Figure 5.56. Fluorescent image set of EGFP-CARD-R150A-K158A double mutant variant (left column) co-expressed with mCh-wtCARD, mCh-CARD-R150A, mCh-CARD-K158A and mCh-CARD-R150A-K158A variants (middle column), and merge (right column).

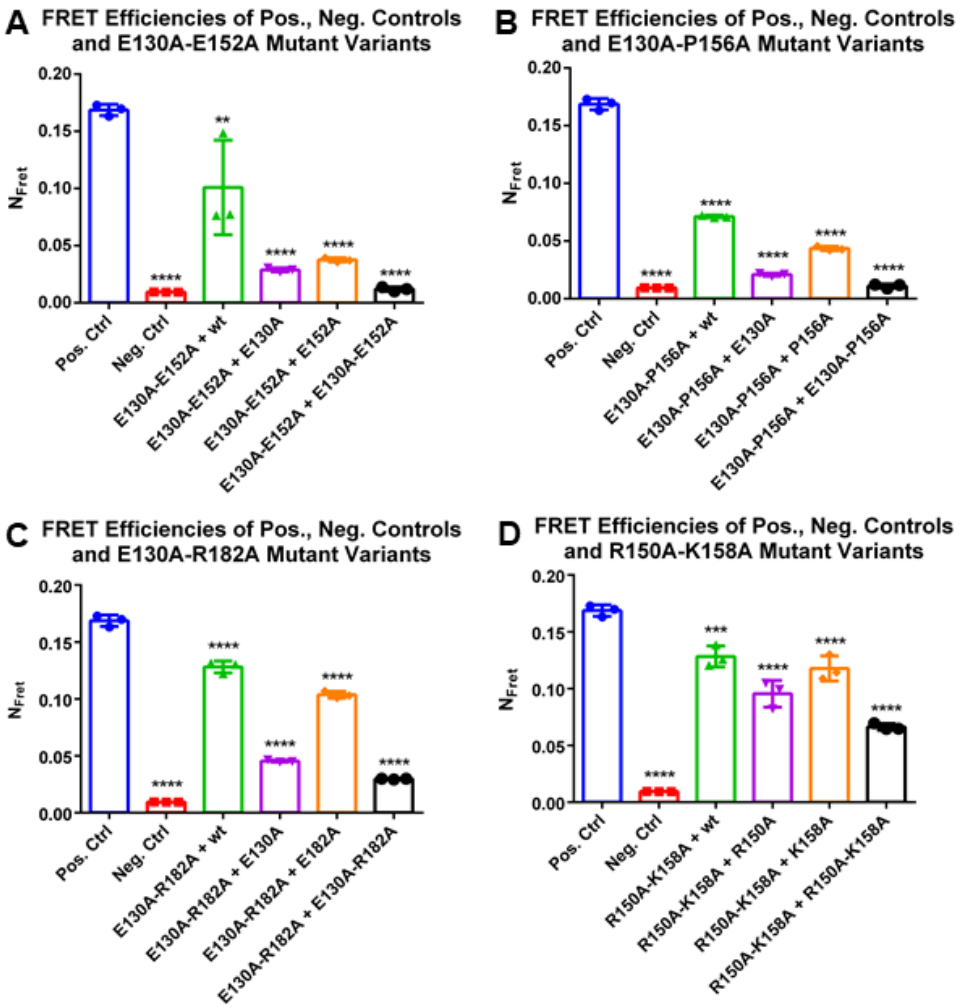

Figure 5.57. N_{FRET} graphs of (A) CARD-E130A-E152A, (B) CARD-E130A-P156A, (C) CARD-E130A-R182A and (D) CARD-R150A-K158A double mutant sets.

5.10.2.2. Double Mutant Show Similar Interaction Rate as Least Single Mutant. In this case, interaction efficiencies of double mutants were at same level as the efficiencies of least single mutant interactions. In E130A-Q185A case, the double mutant showed co-localization with wt, E130A, Q185A and itself. Moreover, rate of interaction between double mutants were same as the rate of interaction between double mutant and E130A single mutant making E130A mutation as the restrictive case (Figure 5.58 and Figure 5.60 A). Type 1b surface was the determinant of interaction rate over Type 2b surface. In Y146A-E152A set, rate of interaction decreased significantly but remained

at low levels. While wt-wt filaments were formed, contribution of double mutant was in very low levels. Also, the double mutant was unable to interact with Y146A single mutant but still able to interact with E152A single mutant (Figure 5.59 and Figure 5.60 B). Type 1b and Type 3b inhibition resulted in decrease in interaction rates.

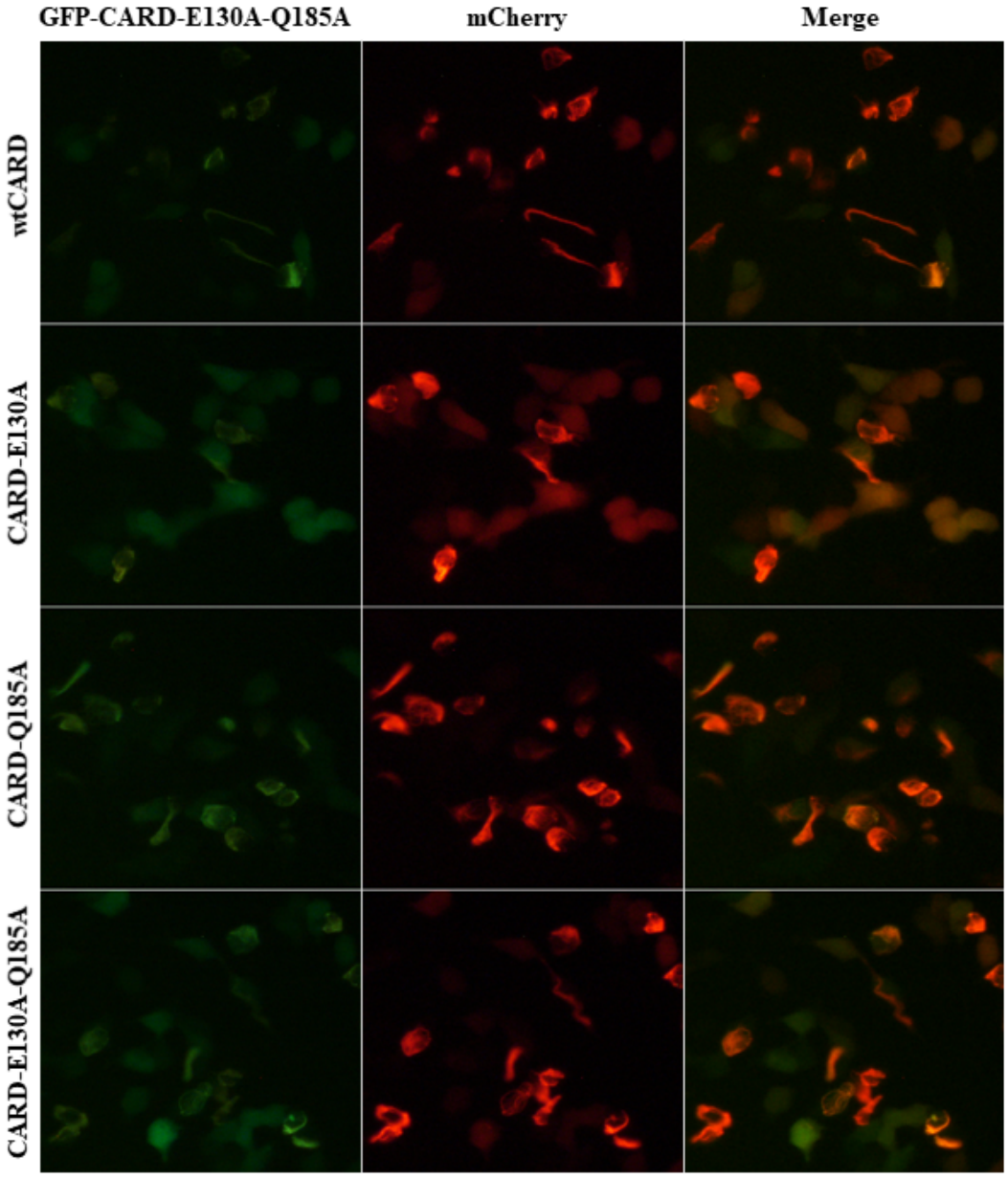

Figure 5.58. Fluorescent image set of EGFP-CARD-E130A-Q185A double mutant variant (left column) co-expressed with mCh-wtCARD, mCh-CARD-E130A, mCh-CARD-Q185A and mCh-CARD-E130A-Q185A variants (middle column), and merge (right column).

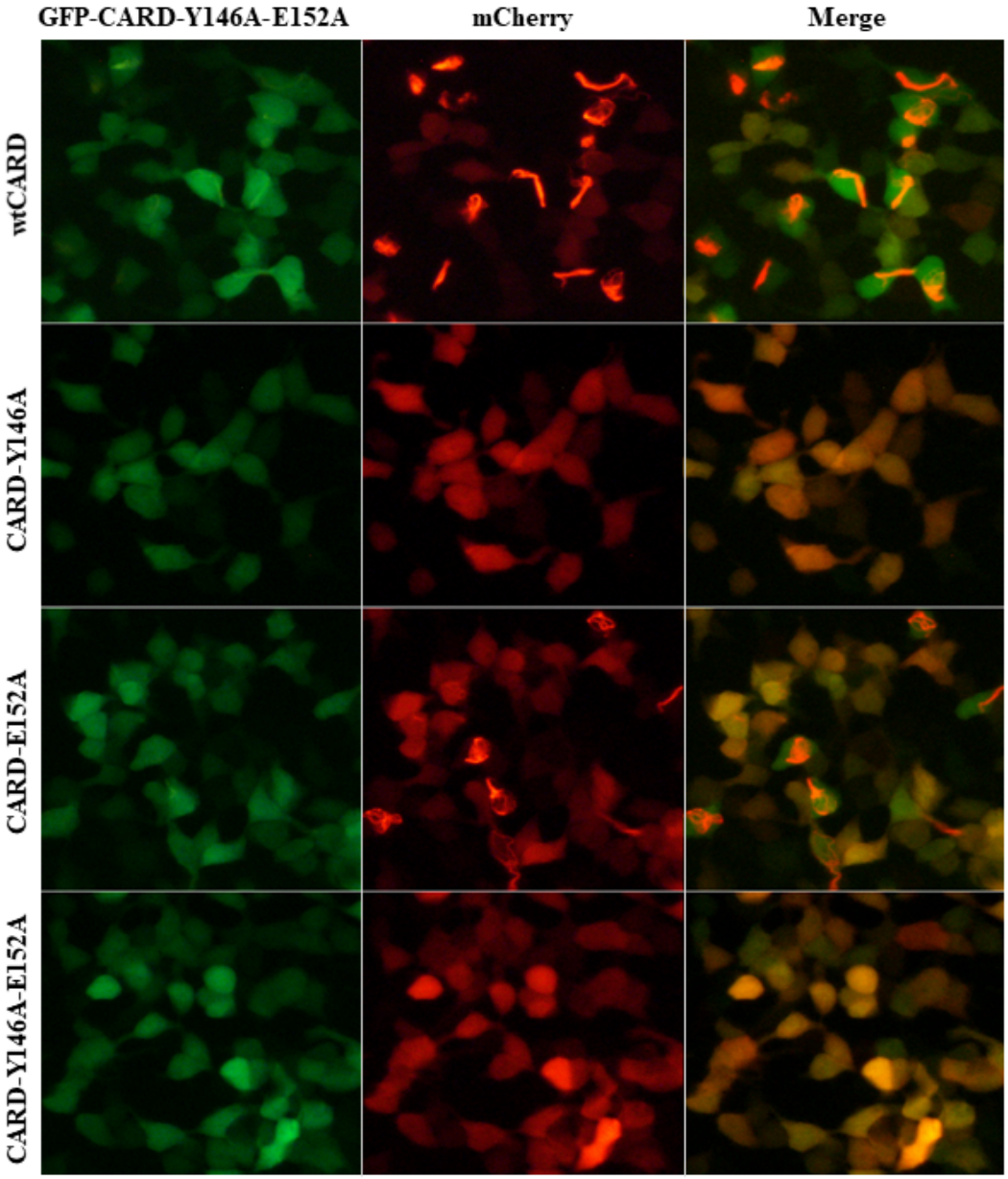

Figure 5.59. Fluorescent image set of EGFP-CARD-Y146A-E152A double mutant variant (left column) co-expressed with mCh-wtCARD, mCh-CARD-Y146A, mCh-CARD-E152A and mCh-CARD-Y146A-E152A variants (middle column), and merge (right column).

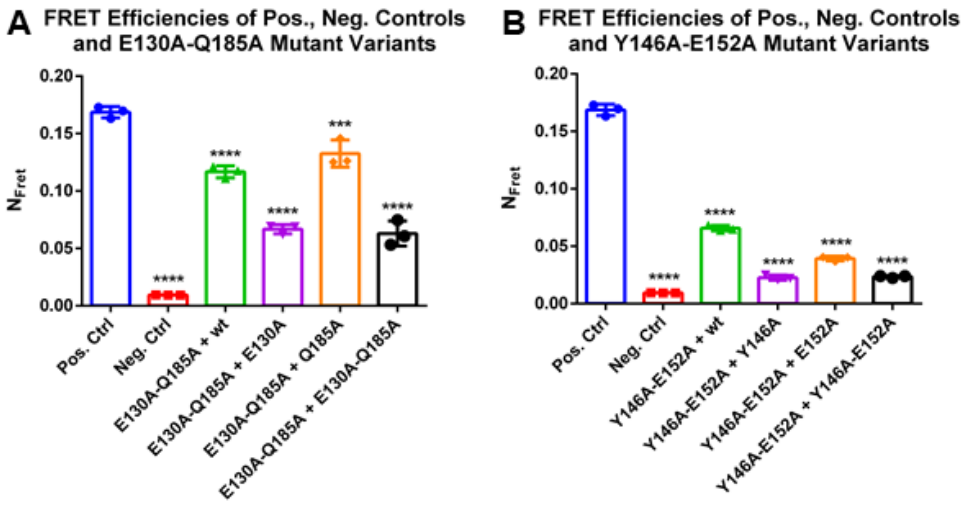

Figure 5.60. N_{FRET} graphs of (A) CARD-E130A-Q185A and (B) CARD-Y146A-E152A double mutant sets.

5.10.2.3. Double Mutant Shows Interaction Rate Between Two Single Mutants. In the case, double mutant variants were able to co-localize with itself at the middle rate of two single mutant showed.

In E130A-R150A case, double mutant co-localized with itself at rate lower than it co-localized with wt and K158A but higher than it co-localized with E130A single mutant (Figure 5.61 and Figure 5.63 A). In the case, of regions of Type 1b interaction surfaces were mutated but the interaction remained in decreased co-localization conditions.

In E130A-K158A case, the double mutant could co-localize with other variants, while its interaction with itself is decreased, interaction with E130A mutation rate showed much more decrease (Figure 5.62 and Figure 5.63 B). Type 1b and Type 3b inhibition resulted in the phenotype where rate double mutant self-oligomerization was increased than inhibition with more disruptive single mutant.

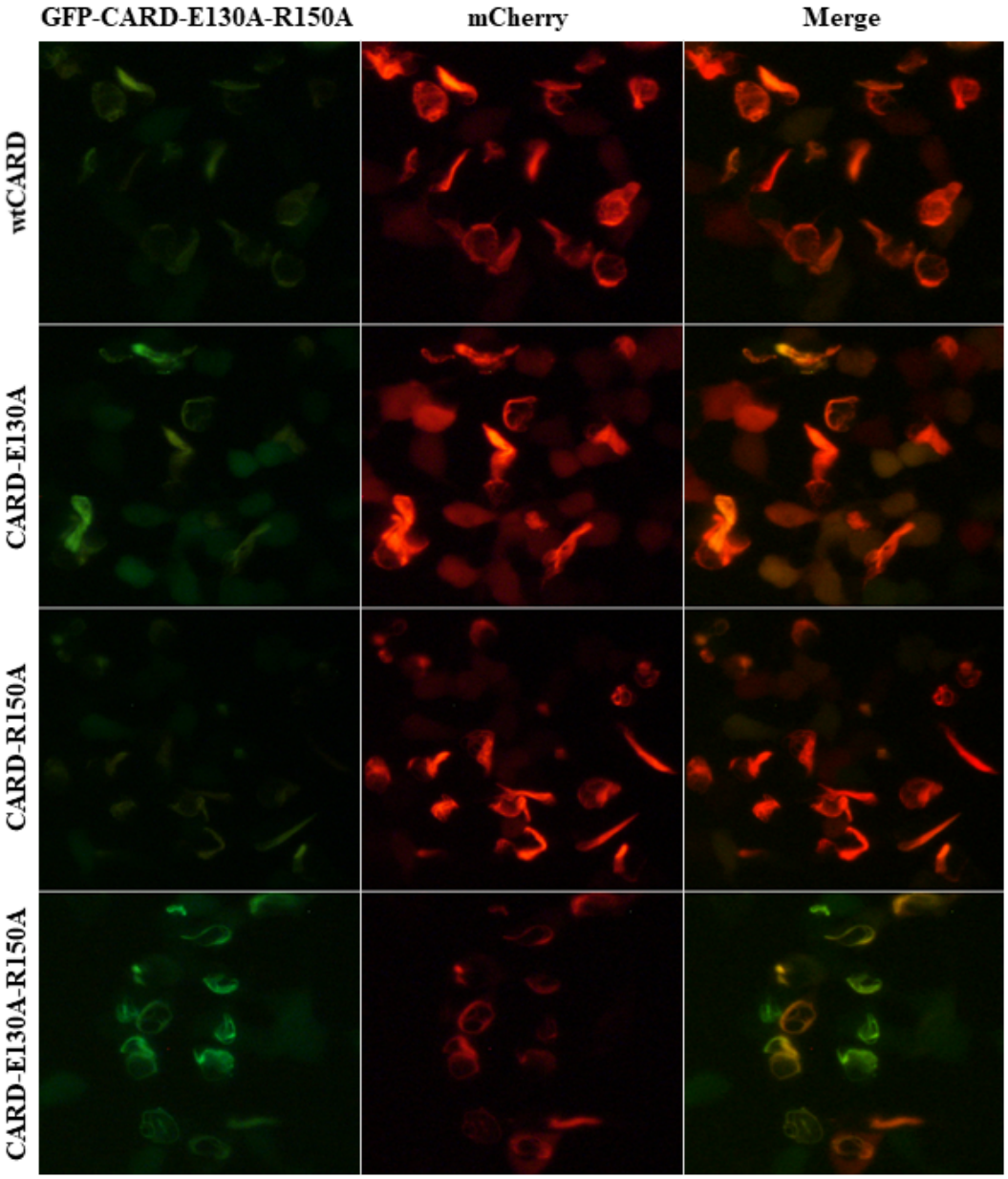

Figure 5.61. Fluorescent image set of EGFP-CARD-E130A-R150A double mutant variant (left column) co-expressed with mCh-wtCARD, mCh-CARD-E130A, mCh-CARD-R150A and mCh-CARD-E130A-R150A variants (middle column), and merge (right column).

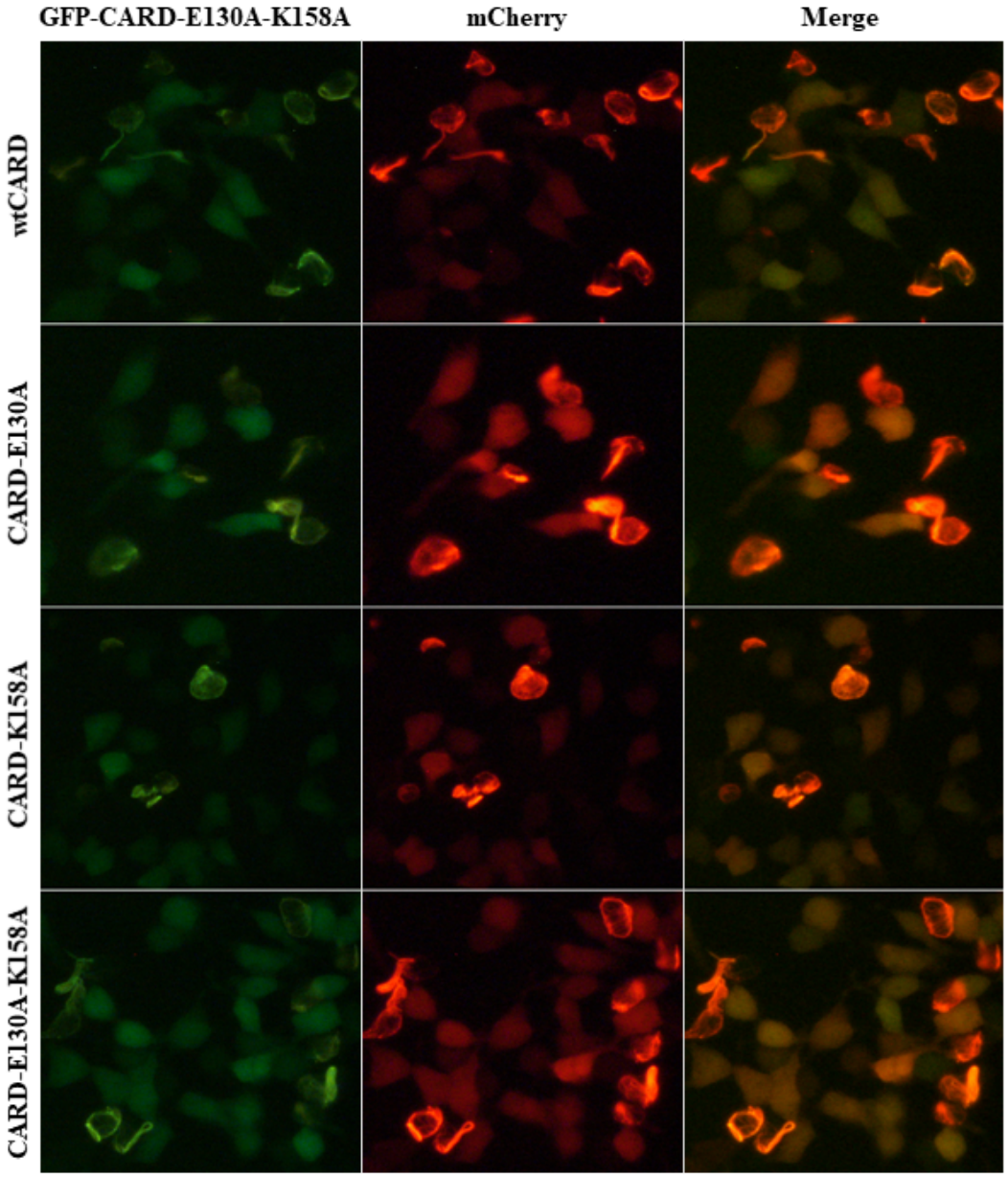

Figure 5.62. Fluorescent image set of EGFP-CARD-E130A-K158A double mutant variant (left column) co-expressed with mCh-wtCARD, mCh-CARD-E130A, mCh-CARD-K158A and mCh-CARD-E130A-K158A variants (middle column), and merge (right column).

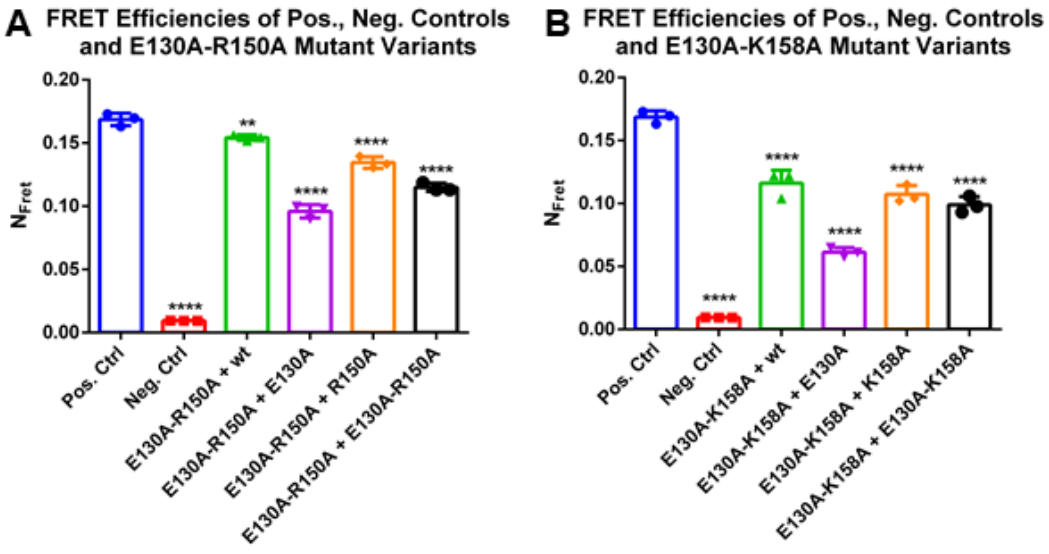

Figure 5.63. N_{FRET} graphs of (A) CARD-E130A-R150A and (B) CARD-E130A-K158A double mutant sets.

5.11. Western Blot Analysis of EGFP-PYD and EGFP-CARD Double Mutant Constructs

EGFP-PYD and EGFP-CARD double mutant constructs were analyzed by western blotting in order to check if the mutations alter the size of protein product causing undesired phenotypes.

HEK293FT cells were transfected with EGFP-PYD and EGFP-CARD double mutants and the cells were collected after transfection. Western blotting procedure was applied as described in Section 4.5.1.

According to the observations, any protein shortening was not detected on both EGFP-PYD (Figure 5.64) and EGFP-CARD (Figure 5.65) double mutant constructs and all the double mutants were remained in same protein size about 36 kDa. No DNA was to control the transfection, GFP-bb was to control the antibody.

In the no DNA sample, antibody did not give any signal. In GFP-bb sample, antibody recognized GFP-bb at about 29 kDa and the band shift of the sample is occurred due to the difference in the sizes of GFP-bb and GFP-PYD domains.

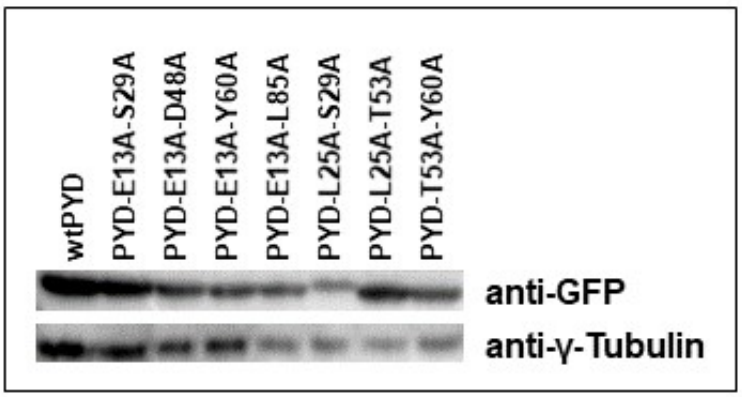

Figure 5.64. Western blot analysis of some EGFP-PYD double mutant constructs.

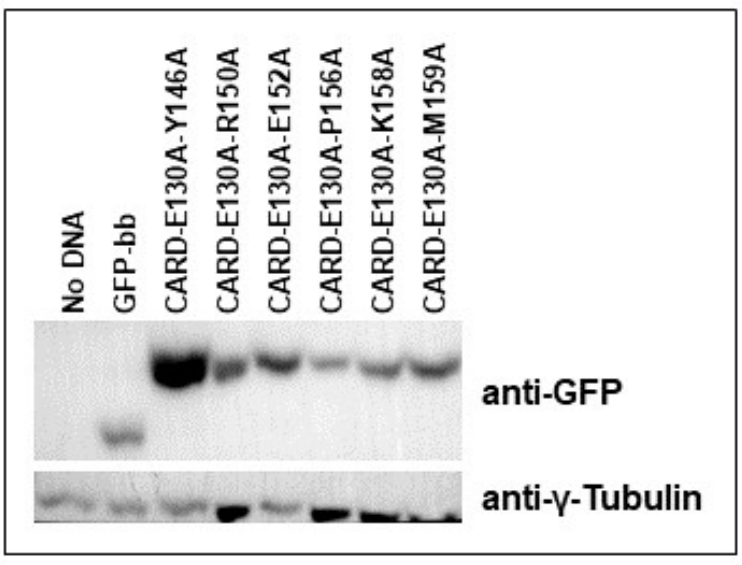

Figure 5.65. Western blot analysis of some EGFP-CARD constructs including no DNA and EGFP-bb controls.

5.12. Interaction of Caspase-1-CARD with Wild Type, Single and Double Mutant ASC-CARD Variants

To observe the effects of disruptive mutations on not only ASC-CARD but also Caspase-1-CARD domains, Cyan Fluorescent Protein (CFP) tagged Caspase-1 encoding plasmids was co-transfected with mCherry-wtCARD, mCherry-CARD-E130A, mCherry-CARD-Q185A and mCherry-CARD-E130A-Q185A mutant variants. HEK 293FT cells were seeded on 6-cm dishes and co-transfections were done to obtain these four subsets.

The reasons why E130A and Q185A mutations were chosen are following, E130 residue was previously determined as in interaction site of ASC-CARD and Caspase-1-CARD [38]. Q185A mutation was chosen as second because of its unique phenotype which normally causes elongation of filaments straightly rather than staying as branched (Figure 5.8 E and Figure 5.31). To observe whether Q185A mutation will provide a long interaction platform increasing surface of interaction area, both single and combinational double mutant with E130A was analyzed.

Interaction analysis of ASC-CARD variants including wt, E130A, Q185A and E130A-Q185A with wt Caspase-1-CARD showed that, while ASC-CARD wt homooligomerized with itself, Caspase-1 was not visually organized on the wtASC-CARD filaments (Figure 5.66 A). Co-expression of ASC-CARD-E130A mutant with Caspase-1 showed neither co-localization with itself, nor co-localization with Caspase-1-CARD (Figure 5.66 B). Q185A single mutant on ASC-CARD showed filament formation and interestingly, Caspase-1-CARD was observed as co-localized on these filaments (Figure 5.66 C). ASC-CARD-E130A-Q185A double mutation co-expressed with Caspase-1-CARD showed a moderate phenotype between phenotypes of Caspase-1 interaction with ASC-CARD-E130A and Q185A single mutants (Figure 5.66 D).

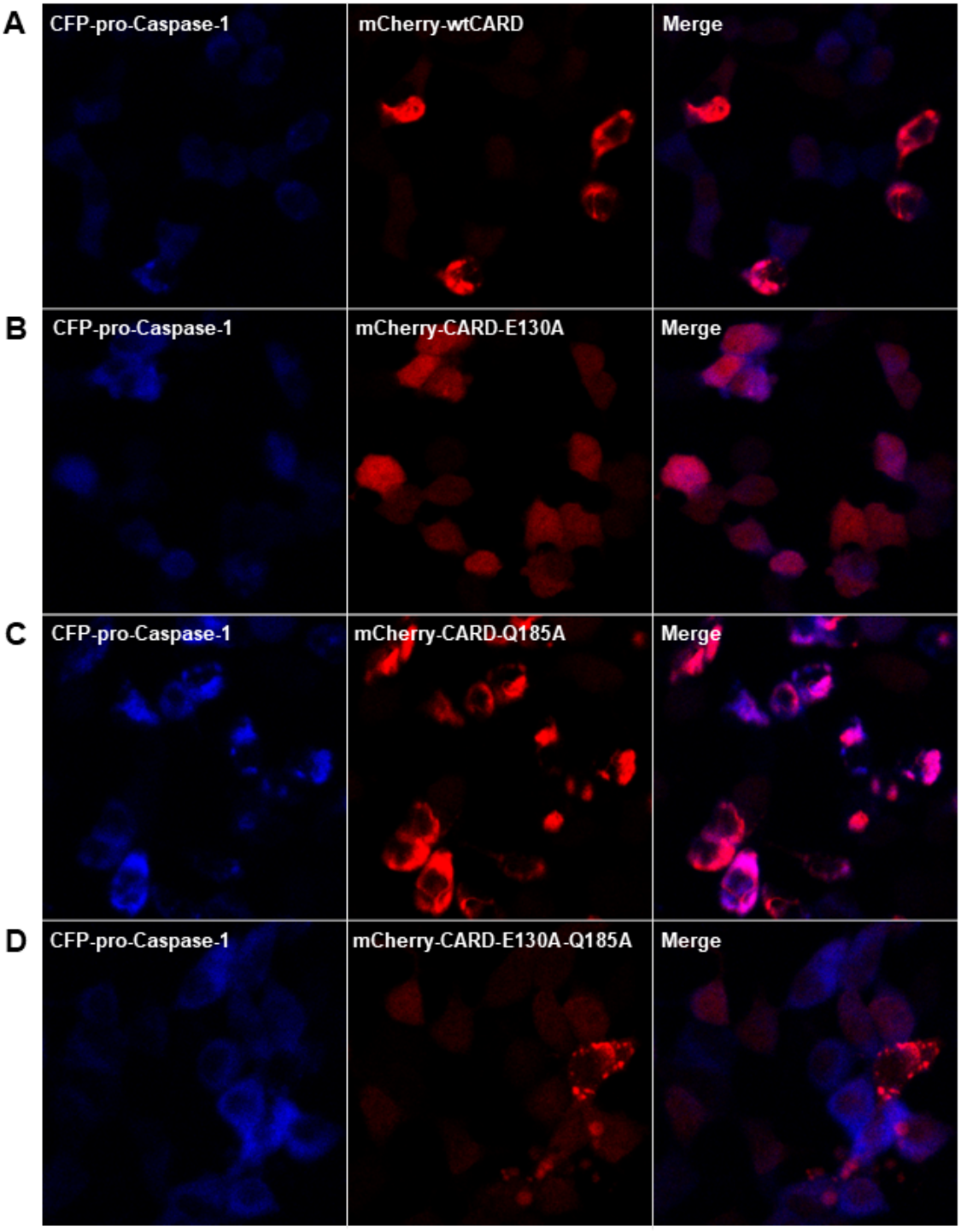

Figure 5.66. Confocal image of CFP-pro-Caspase-1 co-expressed with (A) mCh-wtCARD, (B) mCh-CARD-E130A, (C) mCh-CARD-Q185A and (D) mCh-CARD-E130A-Q185A.

6. DISCUSSION

Inflammasome activation is an essential process in innate immunity providing the early line of response upon stimulation by PAMPs and DAMPs. Key components of inflammasome complex are receptors, adaptor and effector caspase-1 protein. ASC is a 22 kDa protein which has PYD and CARD domains linked with an unstructured 23 aa linker. PYD and CARD domains are members of death-fold superfamily in which common features such as some general functions and structural dynamics are shared. One common feature of these members are their interaction dynamics [39]. The dynamics depend on the three types of interactions with two sub-types for each. Type I, II and III interactions are occurred between different surfaces of helices on these domains. Also, homoologomerization is another common feature through these domains in which only homooligomerization was shown between PYD-PYD or CARD-CARD domains without doing any heterooligomerizations. In previous research in our group, PYD and CARD domains co-transfected with fluorescent tags and their filaments were exclusive for each others preventing any heterooligomerizations [40]. Once PYD domain starts to homooligomerization process, it provides a platform for subsequent PYD-PYD oligomerizations between ASC proteins in the cell. Also, homooligomerization of CARD domains provide additional dimensions to speck formation providing the PYD filaments to be compacted and resulted in a speck shape. The speck is a center for activation of Caspase-1 through which inflammatory cytokines are matured and secreted [41].

In this study, we focused on interaction mechanisms of death-fold family proteins, PYD and CARD which are also two domains of ASC adaptor protein. We analyzed these domains individually because homotypic interactions of PYDs are contributed by additional effects of CARD homotypic interactions. Previous mutational screenings showed that, effects of two single mutations on PYD and CARD domains of ASC protein at different times are more tolerated than effects of their double mutation case at same time [20]. So, we determined to go forward with domains and analyzed them separately.

Previous single mutation based study in our group showed that, some important points on Type I interaction surface act key roles in oligomerizations because their alanine conversion mutations showed decreased yields in wt-mutant oligomerizations [42].

We have showed effects of mutations by introducing them as either mutant-wt or mutant-mutant cases. We also checked effects of novel mutations as well as effects of previous mutations which had been used in only wt-mutant cases. Due to a lack in interaction studies on CARD domains, we focused on CARD-CARD homooligomerizations and most of the mutational screenings were done on CARD domain. In our experimental design, first we started with introduction and screening the effects of single mutations on different interaction surfaces of PYD and CARD domains. Then, we co-expressed the single mutants with either wt or same single mutant variant which have tagged with a different fluorophore in order to discriminate between co-expressed variants. After checking the effects of single mutants, we stepped forward by introducing new double mutation combinations of these single mutations because analysis of disruption in different interaction sites in a step-wise manner gave us a pool of different phenotypes through which subsequent effects could be determined.

In our analysis part, we not only qualified the effects of single and double mutations by checking under fluorescence or confocal laser scanning microscopy, but also checked their interaction efficiencies in a quantitative way using FRET system. After that, we compared FRET efficiencies by subtraction of basal signal levels of fluorophores. All together, our microscopy and FRET results provided not only a proof of concept for the experimental design but also showed new interaction modes where filament formation is in 'all or none' mode but rate of interaction is distributed in a spectrum which positive and negative controls show its maximum and minimum levels.

We showed phenotypes of different combinations of mutations on Type I, II and III interaction surfaces through which underlying mechanisms and order of the interaction events are assessed.

6.1. Single Mutations

In our first experimental design part, we introduced new single mutations on EGFP-PYD, mCherry-PYD, EGFP-CARD and mCherry-CARD templates whose plasmid maps are shown in Appendix B (Figures B.1, B.2, B.3 and B.4). Since, three surfaces of interaction is required for proper homooligomerization of the domains as in Figure 6.1, we disrupted one type at a time with the single mutation screening. The single mutations which we introduced and screened their phenotypes are E13A, L25A, S29A, D48A, T53A, Y60A, E67A, L85A on PYD domain, E130A, Y146A, R150A, E152A, P156A, K158A, M159A, W169A, R182A, E183A and Q185A on CARD domain.

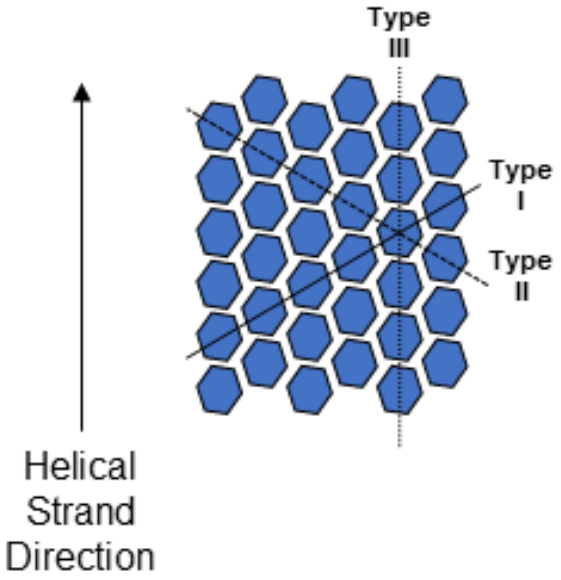

Figure 6.1. Schematic diagram of a helical filament. Three axes which show Type I, II and III interaction directions are indicated with different lines.

In our single mutation sets, we co-expressed EGFP tagged single mutant with either mCherry tagged wt domain or mCherry tagged same mutant domain in order to observe the effects of the mutation on wt-mutant and mutant-mutant interaction process. We observed two cases for PYD and three cases for CARD domains.

On PYD domain, when E13A, D48A, T53A and Y60A mutations were co- expressed with both wt and same mutant variants, N_{FRET} ratios in mutant-mutant sub-cases showed lower values than their wt-mutant cases making these single mutations important for proper interaction. Especially E13 residue was previously shown as potent interaction site [20] and negative charge on glutamate aa might has a role in interaction. D48A mutation showed inhibition condition for the interaction L25A, S29A, E67A and L85A mutations, on the other hand, showed similar results of N_{FRET} ratios between wt-mutant and mutant-mutant sub-cases so, these sites are more tolerant for changes in side chains and co-localize even L25A residue locates on type Ib interaction site. This condition is named as "co-localization" and schematically represented in Figure 6.2 A for three different mutation cases which disrupt the surfaces.

On CARD domain, K158A and M159A seemed to disrupt the filament formation completely and resulted in disruption of interaction in both wt-mutant and mutant-mutant conditions. M159A mutant neither interacted with itself nor with wt, allowing wt-wt domains to form wtCARD filaments. Possible explanation of the case can be the condition of "no co-localization and no-inhibition" as in Figure 6.2 B. Also, two additional patterns for CARD domain was firstly disruption of interaction in mostly mutant-mutant variants, secondly, retaining of interaction as in wt. First, E130A and Y146A mutation sites reside on Type Ib interaction surface and while E130A mutation shows slight co-localization with both wt and mutant, Y146A mutation caused total blockage between mutant-mutant variants on the other hand, N_{FRET} ratio of Y146A mutant-mutant sub-set is higher than negative control. This phenomenon can be explained as "inhibition" and schematically represented in Figure 6.2 C. In inhibition condition, monomers of mutant protein interact with wt variants preventing their further interaction. E152 and W169 also showed similar phenotypes. Secondly, R150A, P156A, R182A, E183A and Q185A mutations showed co-localization and filament formations were observed in the wt-mutant and mutant-mutant co-localization case even R150 and P156 sites reside on type Ib and type IIIb interaction surfaces, respectively.

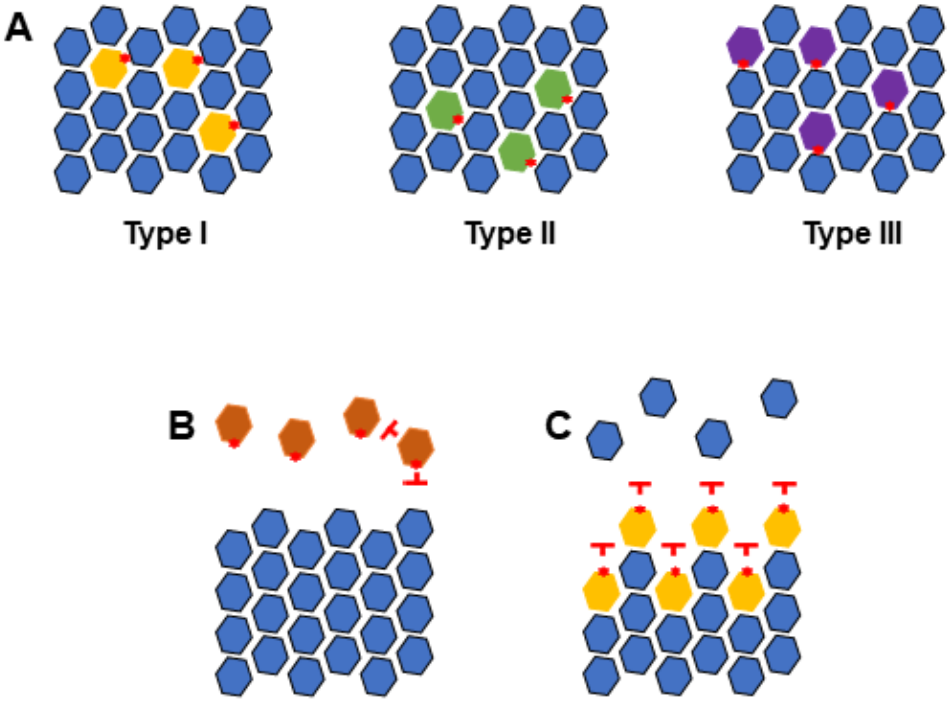

Figure 6.2. Schematic diagram of possible structural cases based on the result of this study. The cases are (A) Co-localization, (B) No-colocalization and no-inhibition, (C) Inhibition for wt-mutant variants.

6.2. Double Mutations

In our second and the biggest experimental design part, we combined single mutations in double mutation sets in order to see effects of disruption in two different interaction surfaces at same time. We introduced totally 8 double mutations on PYD, 14 double mutations on CARD.

According to our observations, N_{FRET} rates of interactions between wt-mutant, two single mutants and double mutant variants were either completely disrupted and observed as nearly same level with negative control or showed four different partially effective distribution patterns as illustrated in Figure 6.3.

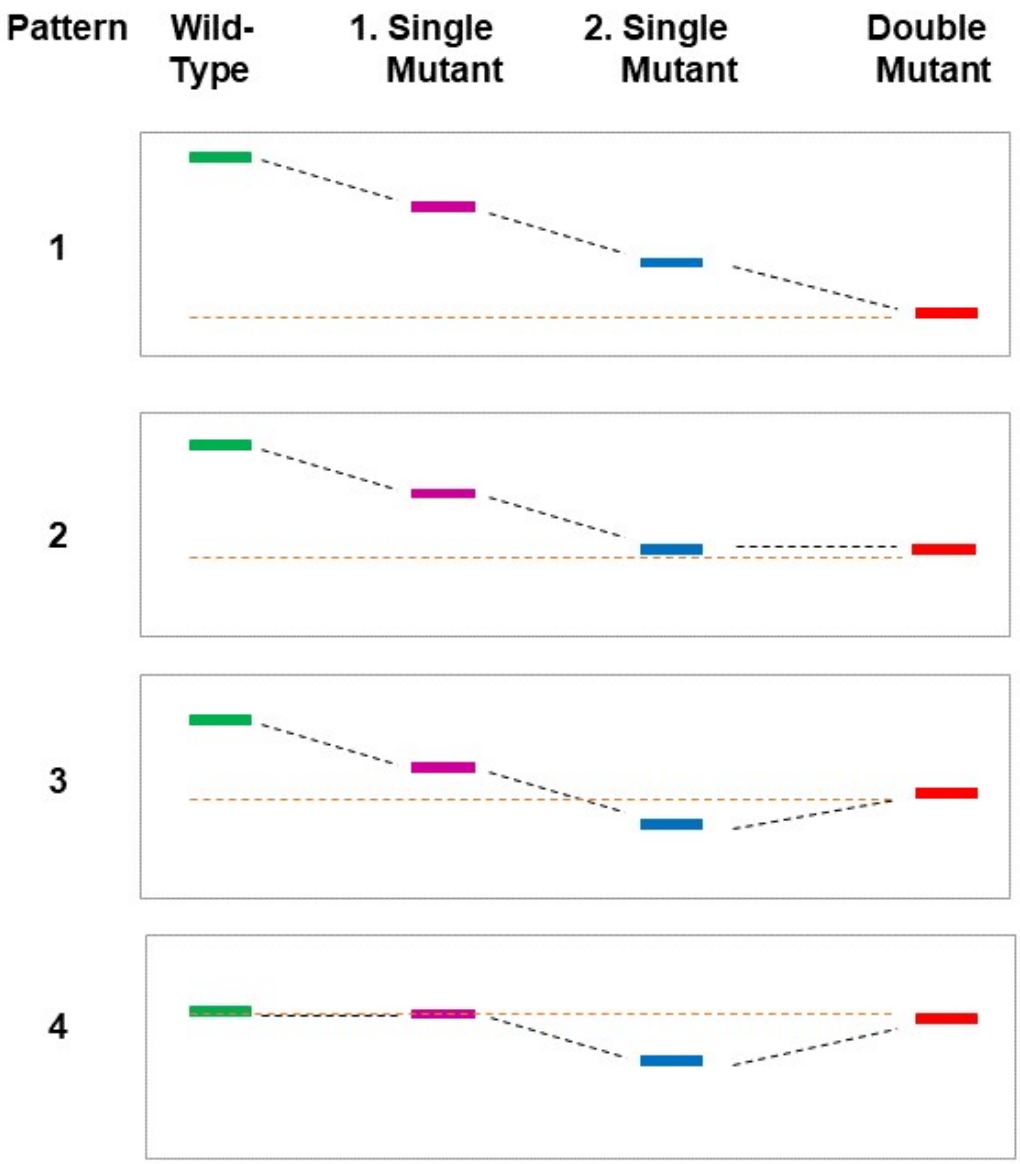

Figure 6.3. Patterns of interaction ratios from N_{FRET} graphs of wt, single and double mutant variants in the double mutant sets.

In these patterns, interaction rates of double mutants were observed as; lower than two single mutants in pattern 1, similar as the lowest single mutant in pattern 2, in medium range between rates of two single mutants in pattern 3 and in similar interaction rate as wild type in pattern 4.

On PYD domain, E13A-D48A and E13A-Y60A double mutants showed blocked phenotype. When D48A and Y60A residues are combined with E13A, filament formation was completely disrupted and also inhibition case was observed in E13A-Y60A set. E13A-S29A and E67A-L85A double mutant sets showed pattern 1 in which effects of the two single mutations are more disruptive when introduced together than in introduced individually as single mutants. E13A-L85A and L25A-T53A double mutants showed features of pattern 2 where the effects of double mutant is same as the effect of lowest single mutant. Here, it is interesting to observe that, while L85A mutation does not affect the interaction between wt and mutant in single sets, its combination with E13A mutation shows more disruption. T53A-Y60A double mutation set showed features of pattern 3 where the interaction rate of double mutant is intermediate between two single mutants. While Y60A mutation showed significant decrease in interaction rate, T53A mutation interestingly, showed increase in interaction and the rate of double mutant was in between of them. L25A-S29A double mutant showed features of pattern 4 in which interaction rates of the double mutant and wt are similar. So, L25A and S29A residues does not changed interaction rate significantly even they reside on type Ib interaction surface.

On CARD domain, E130A-Y146A, E130A-M159A, E130A-W169A, E152A-M159A, E152A-W169A and W169A-R182A sets showed entirely disruption in homologomerizations of the mutant CARD variants with wt, single and double mutant CARDs. E130A-Y146A mutant showed inhibition case. So, when two type I surfaces are disrupted, the outcome is being partly localization of mutants to wt then immediately inhibition of further interactions due to the blocked interaction surfaces. W169A mutation affected type IIa interaction surface and whenever it is combined with another type such as E130A-W169A - type I and II, E152A-W169A - type III and II, the phenotypes are observed as totally disruption in interaction. Thus, type II is observed to have role in which only its disruption can be rescued by other types in single mutant conditions but whenever it is inhibited with other two types, the disruption cannot be recovered by remaining one type.

E130A-E152A, E130A-P156A, E130A-R182A, R150A-K158A mutations showed features of pattern 1 and their double mutant interaction ratios located at below of the lowest single mutant making these sites important in interaction even their single mutant conditions do not show significant changes. 130A-Q185A and 146A-E152A double mutant sets showed features of pattern 2. Presence of E152A slightly increased the interaction rate than in presence of E130A in the double combination with Y146A. E130A-R150A and E130A-K158A double mutant sets showed features of pattern 3 and ratio of double mutant approximated towards the rate of E130A in these double sets. Interestingly, pattern 4 was not observed in CARD double mutants this can be caused by structural dynamics of CARD which has less tolerance upon changes and stays less densely than PYD [43].

In last part of the study, we observed effects of two CARD mutations on interaction dynamics of not only ASC-CARD but also Caspase-1-CARD. Our results indicated that, when E130 residue which is known as Caspase-1 interaction site [38] is mutated, soluble phenotype was shown than filamentous structures on the other hand, Q185A mutation caused extended filaments which might increase the interaction surface for Caspase-1-CARD to be incorporated to interaction with ASC-CARD.

6.3. Conclusions

Death-fold domains are capable of forming filamentous structures in especially cell death pathways [18], [19]. In this thesis, we examined 19 single mutations with 2 subsets for each (38 conditions) and 22 double mutations wit 4 subsets for each (88 conditions). Through the microscopic and spectrofluorometric analyses of single and double mutations, we hope to investigate and describe interaction dynamics of PYD and CARD domains through homooligomerization. According to our results, importance of different interaction types/surface were deeply analyzed and their effects were explained by blocking them one by one. Through this thesis, we hope to explain underlying mechanisms, to reveal the effects and order of interaction events and to make a projection to the homooligomerization dynamics of death-fold proteins.

REFERENCES

1. Kim, Y. K., J.-S. Shin and M. H. Nahm, "NOD-like receptors in infection, immunity, and diseases", *Yonsei medical journal*, Vol. 57, No. 1, pp. 5–14, 2016.

2. Voet, S., S. Srinivasan, M. Lamkanfi and G. van Loo, "Inflammasomes in neuroinflammatory and neurodegenerative diseases", *EMBO molecular medicine*, p. e10248, 2019.

3. Bauernfeind, F. and V. Hornung, "Of inflammasomes and pathogens - sensing of microbes by the inflammasome", *EMBO Molecular Medicine*, Vol. 5, No. 6, pp. 814–826, Jun. 2013.

4. Kersse, K., J. Verspurten, T. V. Berghe and P. Vandenabeele, "The death-fold superfamily of homotypic interaction motifs", *Trends in Biochemical Sciences*, Vol. 36, No. 10, pp. 541–552, Oct. 2011.

5. de Alba, E., "Structure and Interdomain Dynamics of Apoptosis-associated Speck-like Protein Containing a CARD (ASC)", *Journal of Biological Chemistry*, Vol. 284, No. 47, pp. 32932–32941, Nov. 2009.

6. Hoss, F., J. F. Rodriguez-Alcazar and E. Latz, "Assembly and regulation of ASC specks", *Cellular and Molecular Life Sciences*, pp. 1–19, Oct. 2016.

7. Miyawaki, A., "Development of Probes for Cellular Functions Using Fluorescent Proteins and Fluorescence Resonance Energy Transfer", *Annual Review of Biochemistry*, Vol. 80, No. 1, pp. 357–373, Jul. 2011.

8. Parkin, J. and B. Cohen, "An overview of the immune system", *The Lancet*, Vol. 357, No. 9270, pp. 1777–1789, Jun. 2001.

9. Mackay, I. R., F. S. Rosen, P. J. Delves and I. M. Roitt, "The Immune System",

New England Journal of Medicine, Vol. 343, No. 1, pp. 37–49, Jul. 2000.

10. Mackay, I. R., F. S. Rosen, P. J. Delves and I. M. Roitt, "The Immune System", *New England Journal of Medicine*, Vol. 343, No. 2, pp. 108–117, Jul. 2000.

11. Elliott, D. E., S. S. Siddique and J. V. Weinstock, "Innate Immunity in Disease", *Clinical Gastroenterology and Hepatology*, Vol. 12, No. 5, pp. 749–755, May 2014.

12. Cui, J., Y. Chen, H. Y. Wang and R.-F. Wang, "Mechanisms and pathways of innate immune activation and regulation in health and cancer", *Human Vaccines & Immunotherapeutics*, Vol. 10, No. 11, pp. 3270–3285, Nov. 2014.

13. Meylan, E., J. Tschopp and M. Karin, "Intracellular pattern recognition receptors in the host response", *Nature*, Vol. 442, No. 7098, pp. 39–44, Jul. 2006.

14. Elinav, E., T. Strowig, J. Henao-Mejia and R. A. Flavell, "Regulation of the Antimicrobial Response by NLR Proteins", *Immunity*, Vol. 34, No. 5, pp. 665–679, May 2011.

15. Hauenstein, A. V., L. Zhang and H. Wu, "The hierarchical structural architecture of inflammasomes, supramolecular inflammatory machines", *Current Opinion in Structural Biology*, Vol. 31, No. 4, pp. 75–83, Apr. 2015.

16. Miao, E. A., I. A. Leaf, P. M. Treuting, D. P. Mao, M. Dors, A. Sarkar, S. E. Warren, M. D. Wewers and A. Aderem, "Caspase-1-induced pyroptosis is an innate immune effector mechanism against intracellular bacteria", *Nature immunology*, Vol. 11, No. 12, p. 1136, 2010.

17. Suzuki, T., L. Franchi, C. Toma, H. Ashida, M. Ogawa, Y. Yoshikawa, H. Mimuro, N. Inohara, C. Sasakawa and G. Nuñez, "Differential regulation of caspase-1 activation, pyroptosis, and autophagy via Ipaf and ASC in Shigella-infected macrophages", *PLoS pathogens*, Vol. 3, No. 8, p. e111, 2007.

18. Hughes, M. A., I. R. Powley, R. Jukes-Jones, S. Horn, M. Feoktistova, L. Fairall, J. W. Schwabe, M. Leverkus, K. Cain and M. MacFarlane, "Co-operative and Hierarchical Binding of c-FLIP and Caspase-8: A Unified Model Defines How c-FLIP Isoforms Differentially Control Cell Fate", *Molecular Cell*, Vol. 61, No. 6, pp. 834–849, Mar. 2016.

19. Janssens, S. and A. Tinel, "The PIDDosome, DNA-damage-induced apoptosis and beyond", *Cell Death and Differentiation*, Vol. 19, No. 1, pp. 13–20, Jan. 2012.

20. Sahillioglu, A. C., F. Sumbul, N. Ozoren and T. Haliloglu, "Structural and Dynamics Aspects of ASC Speck Assembly", *Structure*, Vol. 22, No. 12, pp. 1722–1734, Dec. 2014.

21. Cai, X., J. Chen, H. Xu, S. Liu, Q.-X. Jiang, R. Halfmann and Z. J. Chen, "Prion-like Polymerization Underlies Signal Transduction in Antiviral Immune Defense and Inflammasome Activation", *Cell*, Vol. 156, No. 6, pp. 1207–1222, Mar. 2014.

22. Sborgi, L., F. Ravotti, V. P. Dandey, M. S. Dick, A. Mazur, S. Reckel, M. Chami, S. Scherer, M. Huber, A. Böckmann, E. H. Egelman, H. Stahlberg, P. Broz, B. H. Meier and S. Hiller, "Structure and assembly of the mouse ASC inflammasome by combined NMR spectroscopy and cryo-electron microscopy", *Proceedings of the National Academy of Sciences*, Vol. 112, No. 43, pp. 13237–13242, Oct. 2015.

23. Liepinsh, E., R. Barbals, E. Dahl, A. Sharipo, E. Staub and G. Otting, "The Death-domain Fold of the ASC PYRIN Domain, Presenting a Basis for PYRIN/PYRIN Recognition", *Journal of Molecular Biology*, Vol. 332, No. 5, pp. 1155–1163, Oct. 2003.

24. Lu, A., V. G. Magupalli, J. Ruan, Q. Yin, M. K. Atianand, M. R. Vos, G. F. Schröder, K. A. Fitzgerald, H. Wu and E. H. Egelman, "Unified Polymerization Mechanism for the Assembly of ASC-Dependent Inflammasomes", *Cell*, Vol. 156, No. 6, pp. 1193–1206, Mar. 2014.

25. Richards, N., P. Schaner, A. Diaz, J. Stuckey, E. Shelden, A. Wadhwa and D. L. Gumucio, "Interaction between Pyrin and the Apoptotic Speck Protein (ASC) Modulates ASC-induced Apoptosis", *Journal of Biological Chemistry*, Vol. 276, No. 42, pp. 39320–39329, Oct. 2001.

26. Schmidt, F. I., A. Lu, J. W. Chen, J. Ruan, C. Tang, H. Wu and H. L. Ploegh, "A single domain antibody fragment that recognizes the adaptor ASC defines the role of ASC domains in inflammasome assembly", *The Journal of Experimental Medicine*, Vol. 213, No. 5, pp. 771–790, May 2016.

27. Fernandes-Alnemri, T., J. Wu, J.-W. Yu, P. Datta, B. Miller, W. Jankowski, S. Rosenberg, J. Zhang and E. S. Alnemri, "The pyroptosome: a supramolecular assembly of ASC dimers mediating inflammatory cell death via caspase-1 activation", *Cell Death and Differentiation*, Vol. 14, No. 9, pp. 1590–1604, Sep. 2007.

28. Sahillioğlu, A. C. and N. Özören, "Artificial Loading of ASC Specks with Cytosolic Antigens", *PLOS ONE*, Vol. 10, No. 8, p. e0134912, Aug. 2015.

29. Yaşa, S., *In Vivo Studies of ASC Specks as Antigen Delivery Vehicles*, Ms thesis, Boğaziçi University, 2017.

30. Forster, T., "Energiewanderung und Fluoreszenz", *Die Naturwissenschaften*, Vol. 33, No. 6, pp. 166–175, 1946.

31. Zaccolo, M., "Use of Chimeric Fluorescent Proteins and Fluorescence Resonance Energy Transfer to Monitor Cellular Responses", *Circulation Research*, Vol. 94, No. 7, pp. 866–873, Apr. 2004.

32. Zeug, A., A. Woehler, E. Neher and E. G. Ponimaskin, "Quantitative Intensity-Based FRET Approaches—A Comparative Snapshot", *Biophysical Journal*, Vol. 103, No. 9, pp. 1821–1827, Nov. 2012.

33. Bajar, B., E. Wang, S. Zhang, M. Lin and J. Chu, "A Guide to Fluorescent Protein

FRET Pairs", *Sensors*, Vol. 16, No. 9, p. 1488, Sep. 2016.

34. Hoppe, A., K. Christensen and J. A. Swanson, "Fluorescence Resonance Energy Transfer-Based Stoichiometry in Living Cells", *Biophysical Journal*, Vol. 83, No. 6, pp. 3652–3664, Dec. 2002.

35. Xia, Y., W. Chu, Q. Qi and L. Xun, "New insights into the QuikChangeTM process guide the use of Phusion DNA polymerase for site-directed mutagenesis", *Nucleic Acids Research*, Vol. 43, No. 2, pp. e12–e12, Jan. 2015.

36. Kovtun, A., R. Heumann and M. Epple, "Calcium phosphate nanoparticles for the transfection of cells.", *Bio-medical materials and engineering*, Vol. 19, No. 2-3, pp. 241–7, 2009.

37. Dick, M. S., L. Sborgi, S. Rühl, S. Hiller and P. Broz, "ASC filament formation serves as a signal amplification mechanism for inflammasomes", *Nature Communications*, Vol. 7, No. May, p. 11929, Jun. 2016.

38. Proell, M., M. Gerlic, P. D. Mace, J. C. Reed and S. J. Riedl, "The CARD plays a critical role in ASC foci formation and inflammasome signalling", *Biochemical Journal*, Vol. 449, No. 3, pp. 613–621, Feb. 2013.

39. Kuri, P., N. L. Schieber, T. Thumberger, J. Wittbrodt, Y. Schwab and M. Leptin, "Dynamics of in vivo ASC speck formation", *Journal of Cell Biology*, Vol. 216, No. 9, pp. 2891–2909, 2017.

40. Sahillioğlu, A. C., *Structural Aspects of ASC Speck Formation and Its Potential Novel Functions*, Ms thesis, Boğaziçi University, 2010.

41. Franklin, B. S., E. Latz and F. I. Schmidt, "The intra-and extracellular functions of ASC specks", *Immunological Reviews*, Vol. 281, No. 1, pp. 74–87, 2018.

42. Kuzucu, H. O., *Study of the Polymerization Dynamics of Asc and its Domains*,

Ms thesis, Boğaziçi University, 2017.

43. Li, Y., Y. Huang, X. Cao, X. Yin, X. Jin, S. Liu, J. Jiang, W. Jiang, T. S. Xiao, R. Zhou *et al.*, "Functional and structural characterization of zebrafish ASC", *The FEBS journal*, Vol. 285, No. 14, pp. 2691–2707, 2018.

APPENDIX A: EMISSION SPECTRA OF ALL VARIANTS

A.1. Emission Spectra of Variants Carrying Single Mutation

A.1.1. PYD Variants

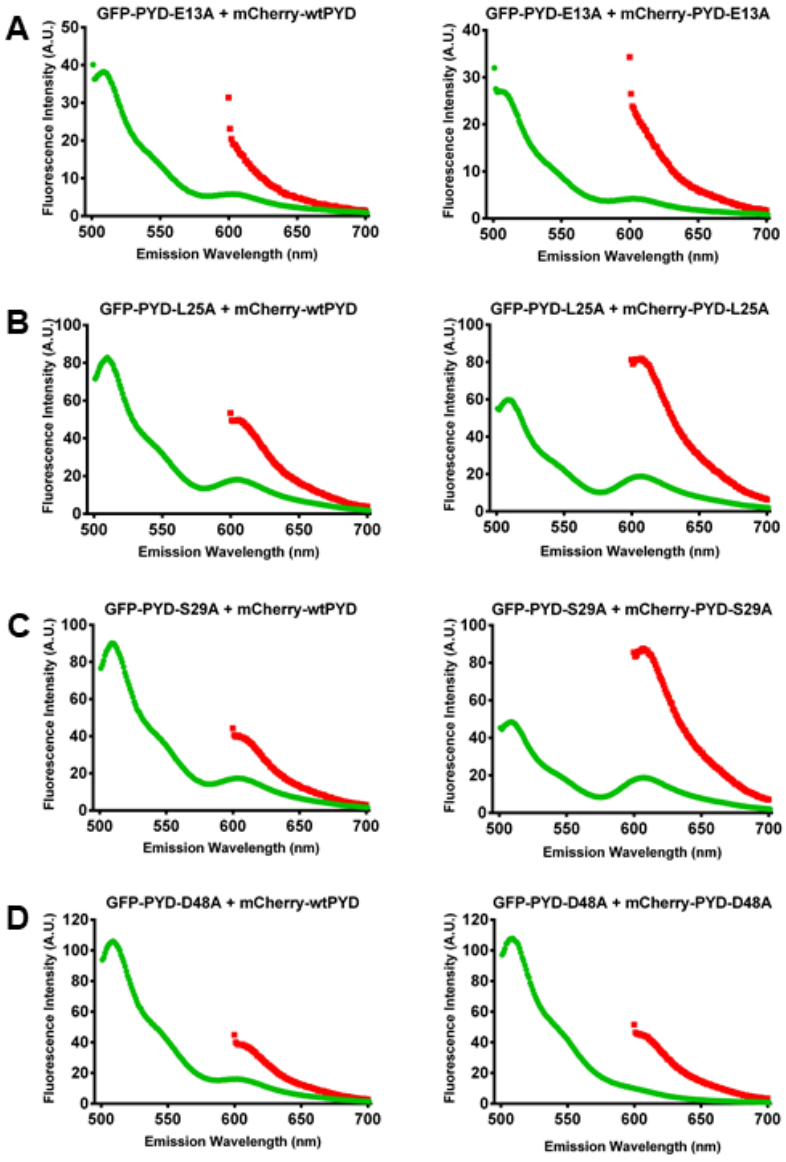

Figure A.1. Emission spectra of PYD (A) E13A, (B) L25A, (C) S29A and (C) D48A variants

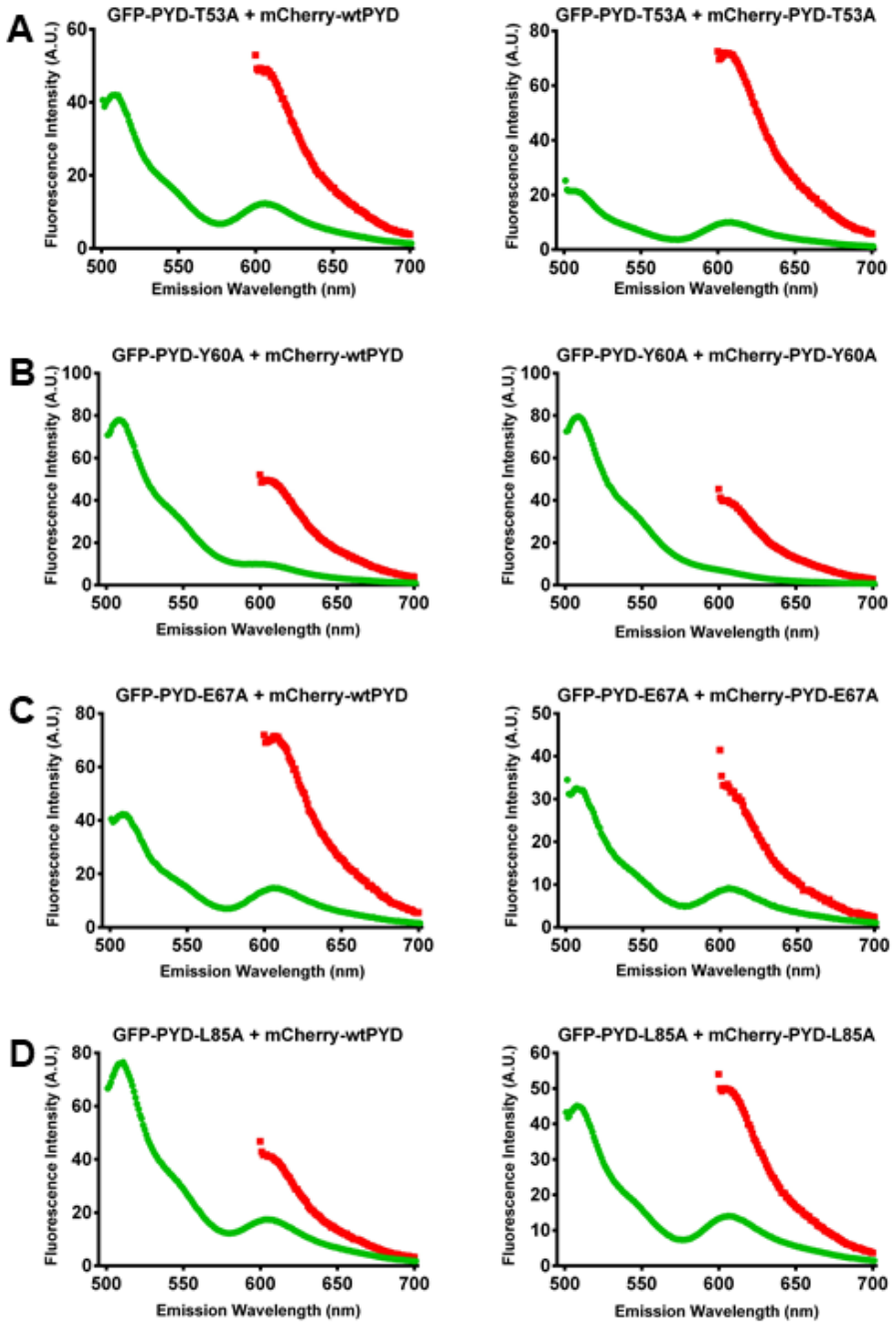

Figure A.2. Emission spectra of PYD (A) T53A, (B) Y60A, (C) E67A and (C) L85A variants

A.1.2. CARD Variants

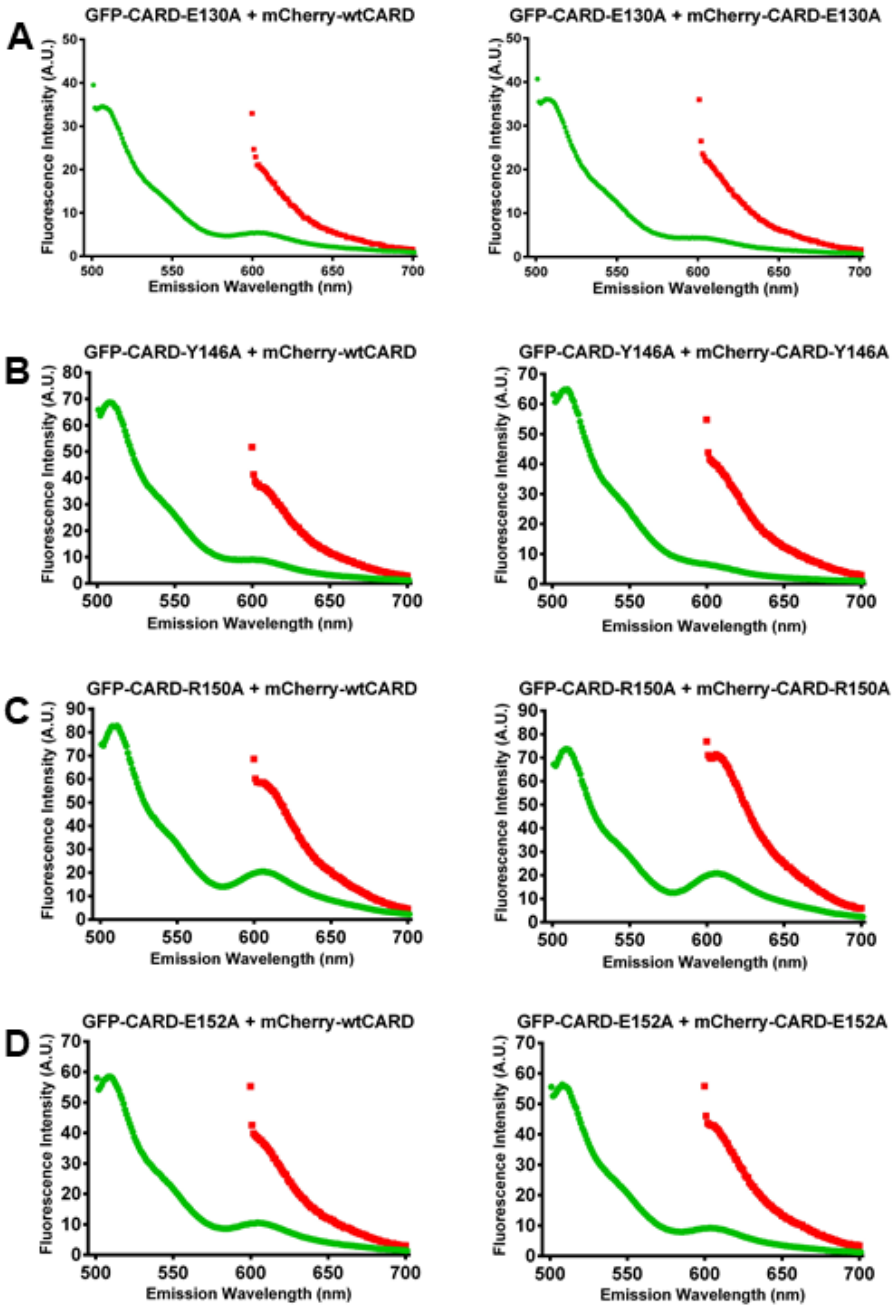

Figure A.3. Emission spectra of CARD (A) E130A, (B) Y146A, (C) R150A and (C) E152A variants

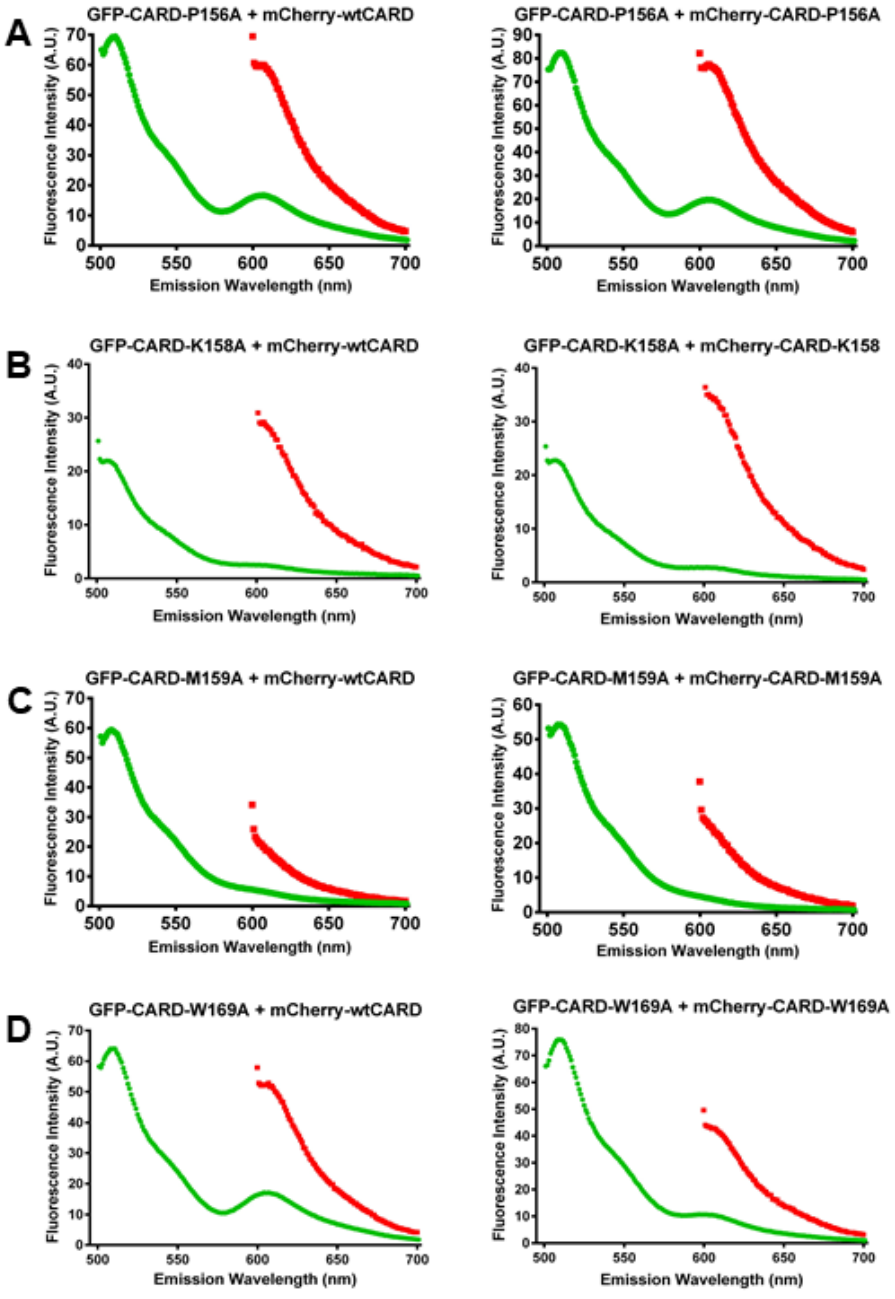

Figure A.4. Emission spectra of CARD (A) P156A, (B) K158A, (C) M159A and (C) W169A variants

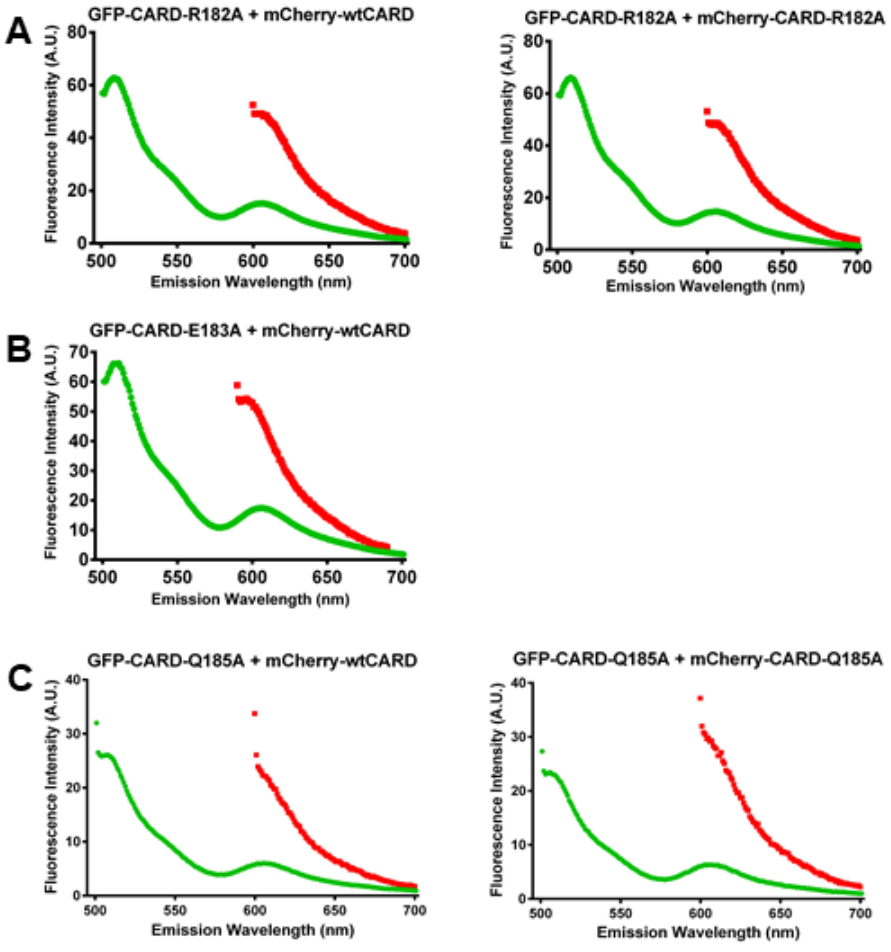

Figure A.5. Emission spectra of CARD (A) R182A, (B) E183A and (C) Q185A variants

A.2. Emission Spectra of Variants Carrying Double Mutations

A.2.1. PYD Variants

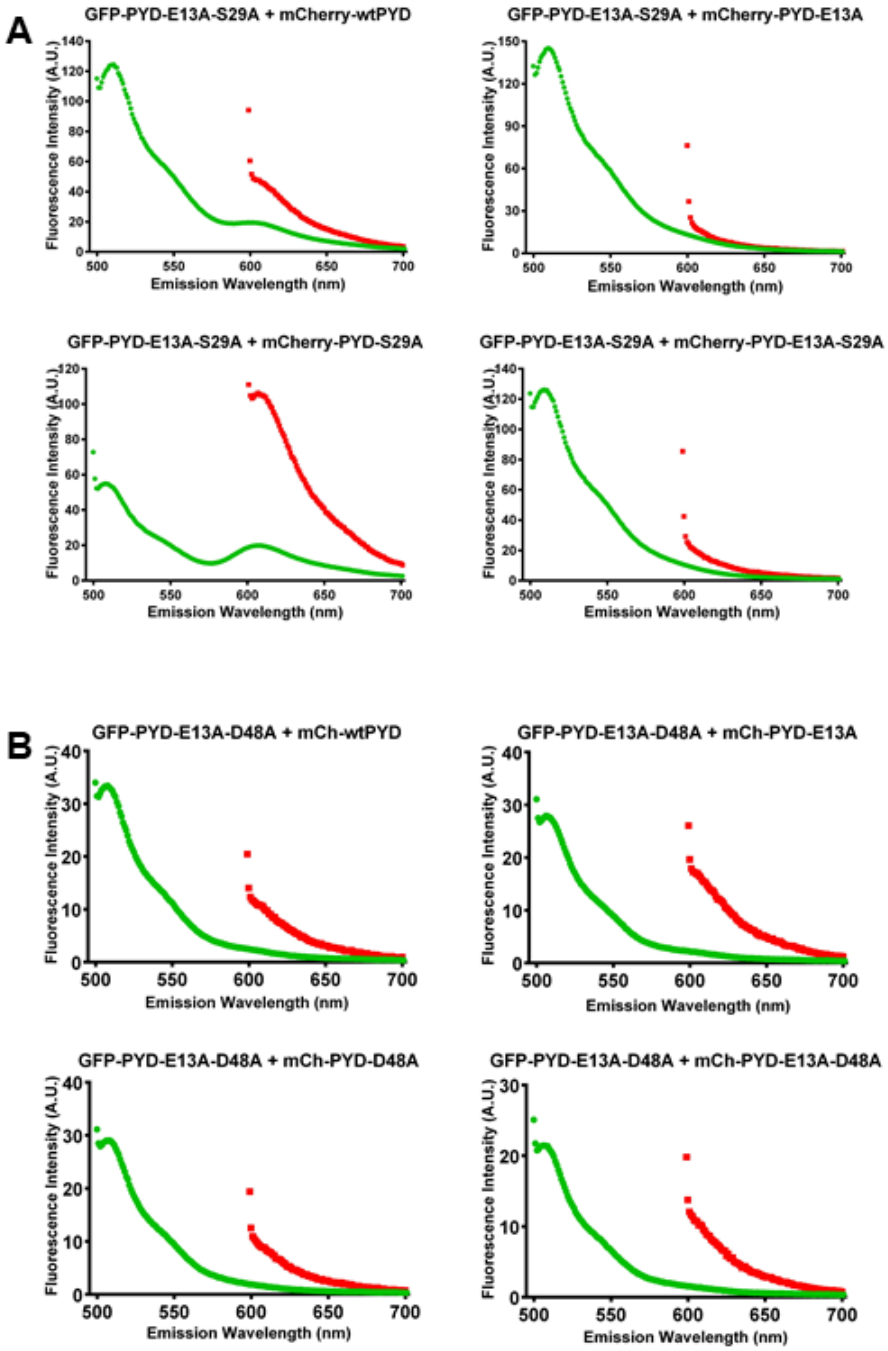

Figure A.6. Emission spectra of PYD (A) E13A-S29A and (B) E13A-D48A variants.

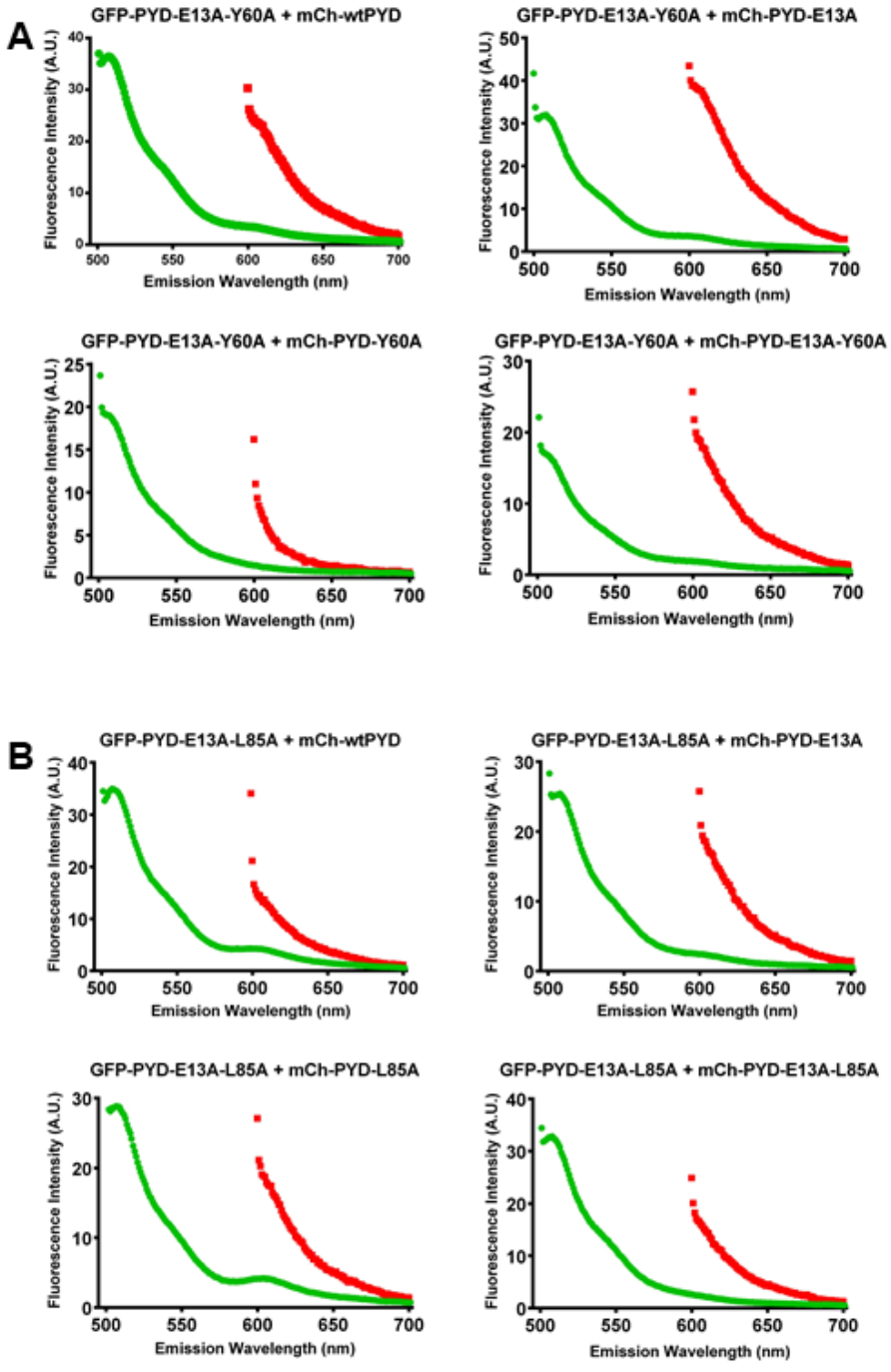

Figure A.7. Emission spectra of PYD (A) E13A-Y60A and (B) E13A-L85A variants.

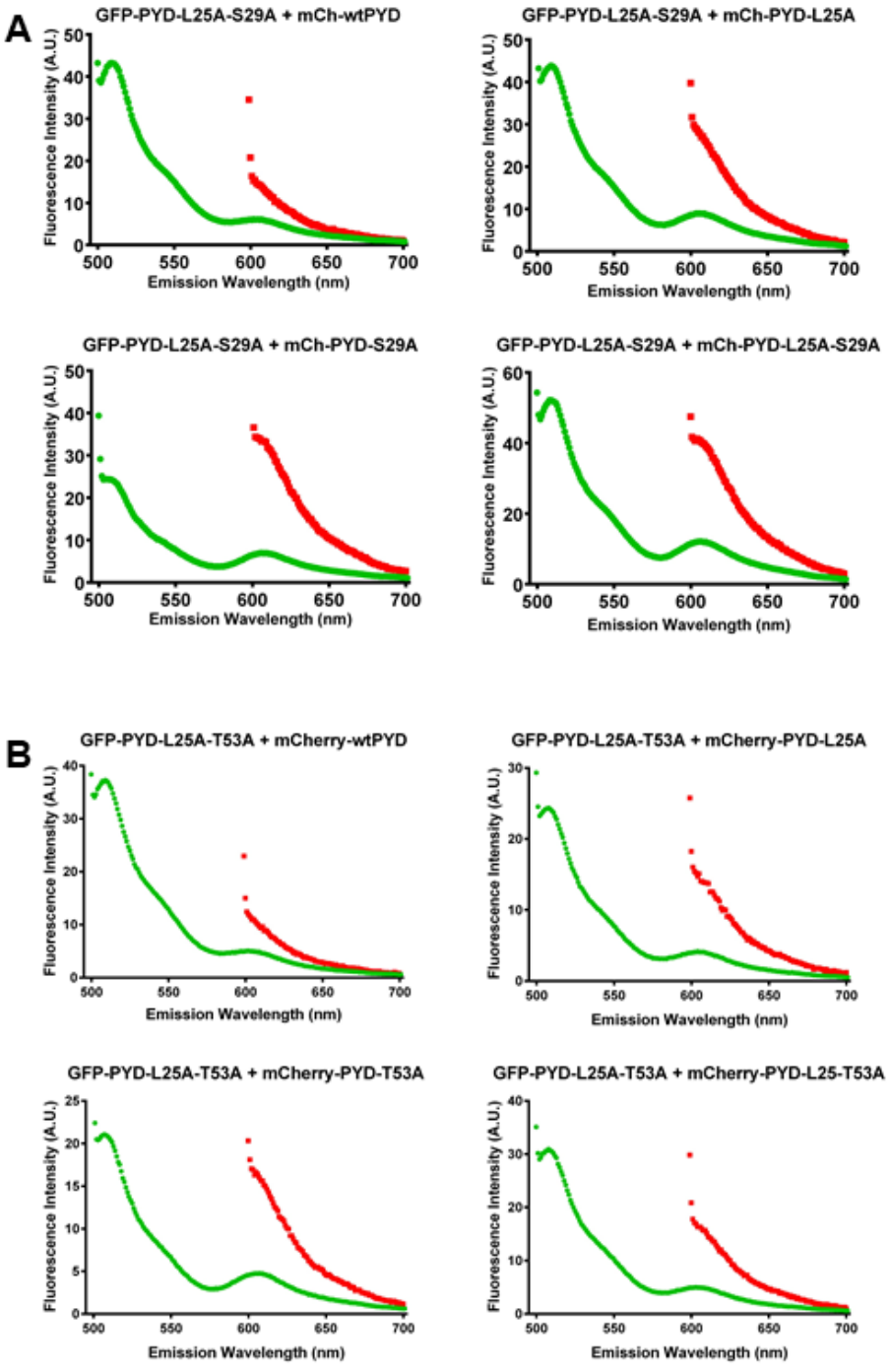

Figure A.8. Emission spectra of PYD (A) L25A-S29A and (B) L25-T53A variants.

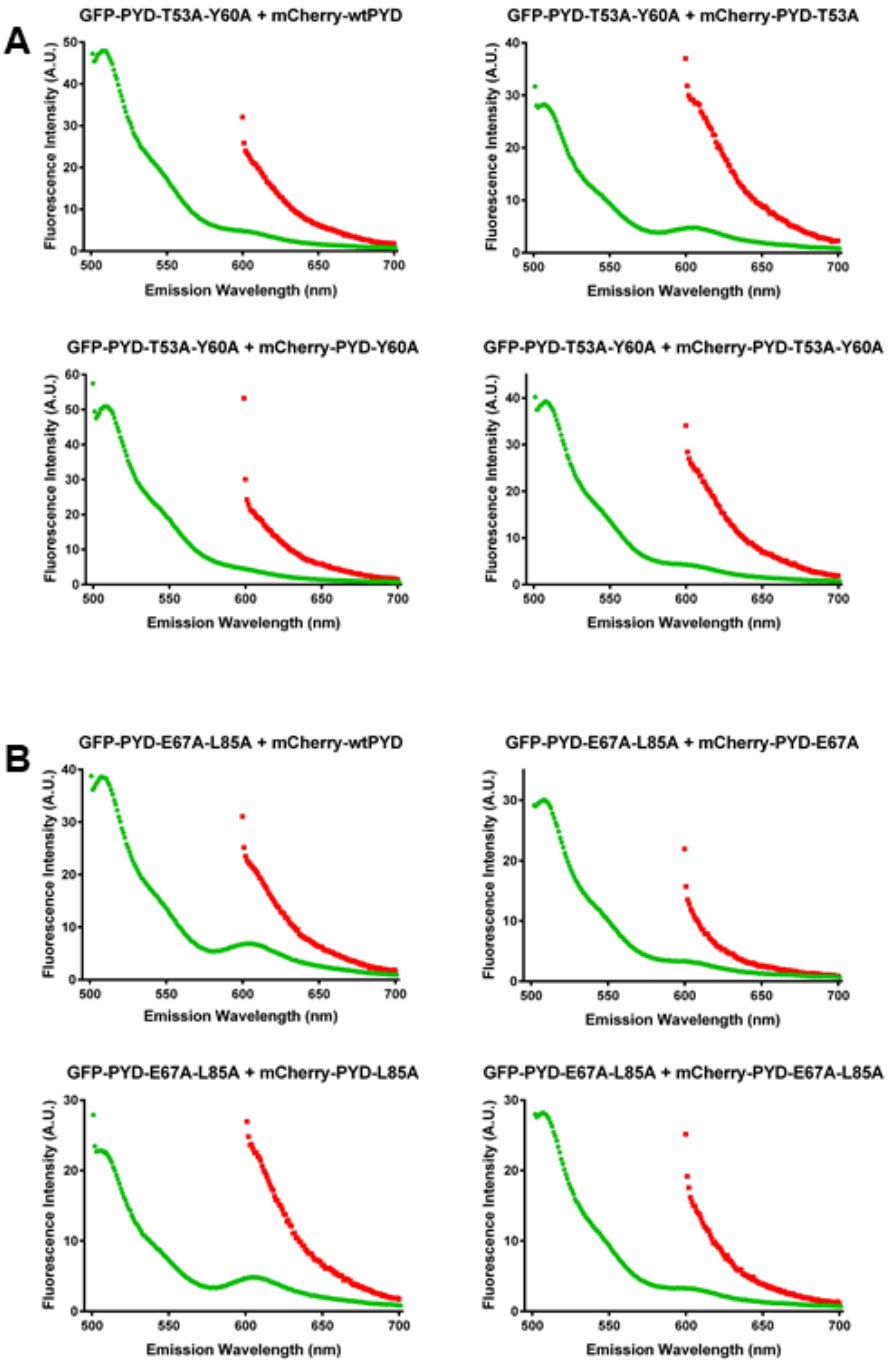

Figure A.9. Emission spectra of PYD (A) T53A-Y60A and (B) E67A-L85A variants.

A.2.2. CARD Variants

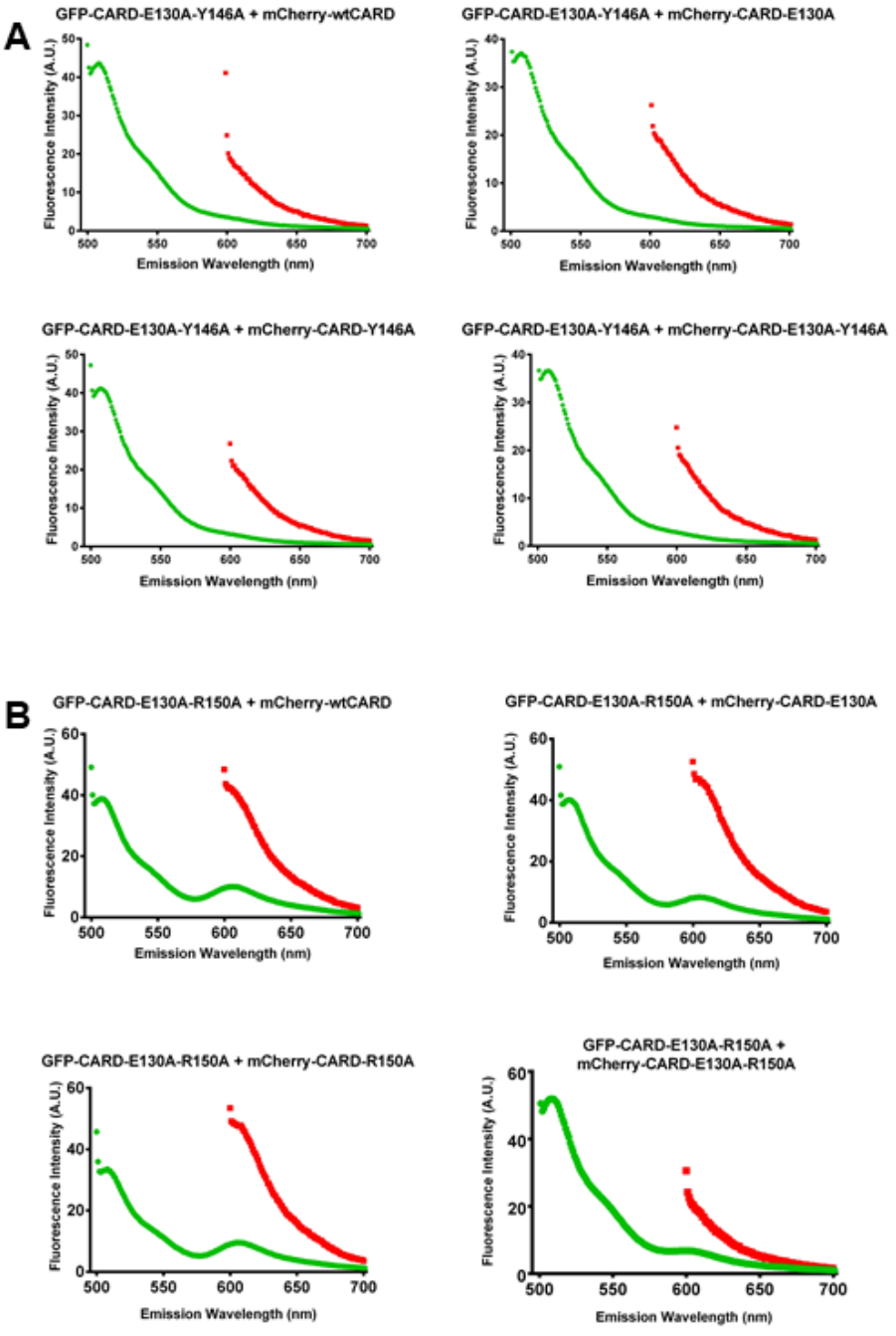

Figure A.10. Emission spectra of CARD (A) E130A-Y146A and (B) E130A-R150A variants.

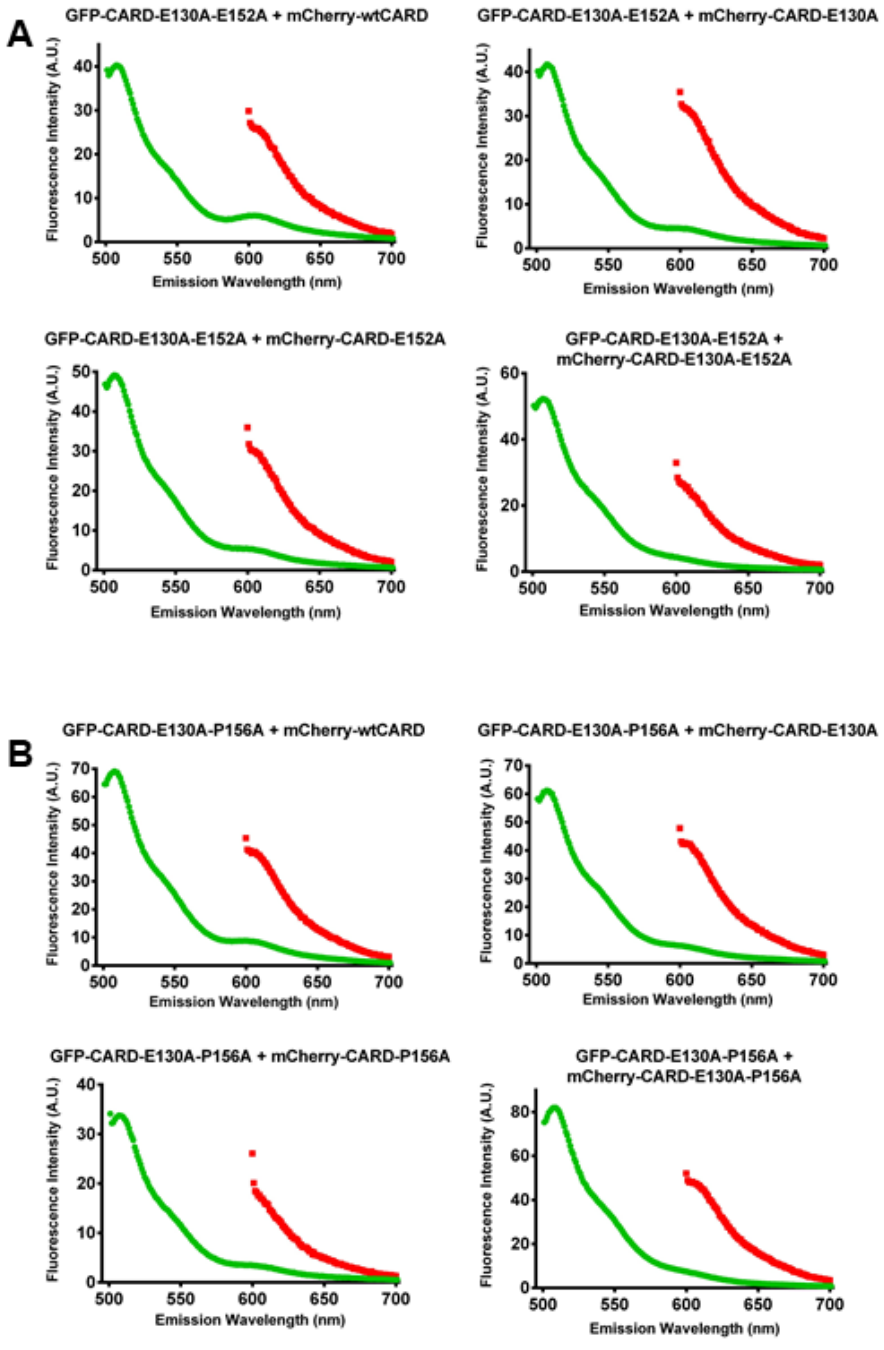

Figure A.11. Emission spectra of CARD (A) E130A-E152A and (B) E130A-P156A variants.

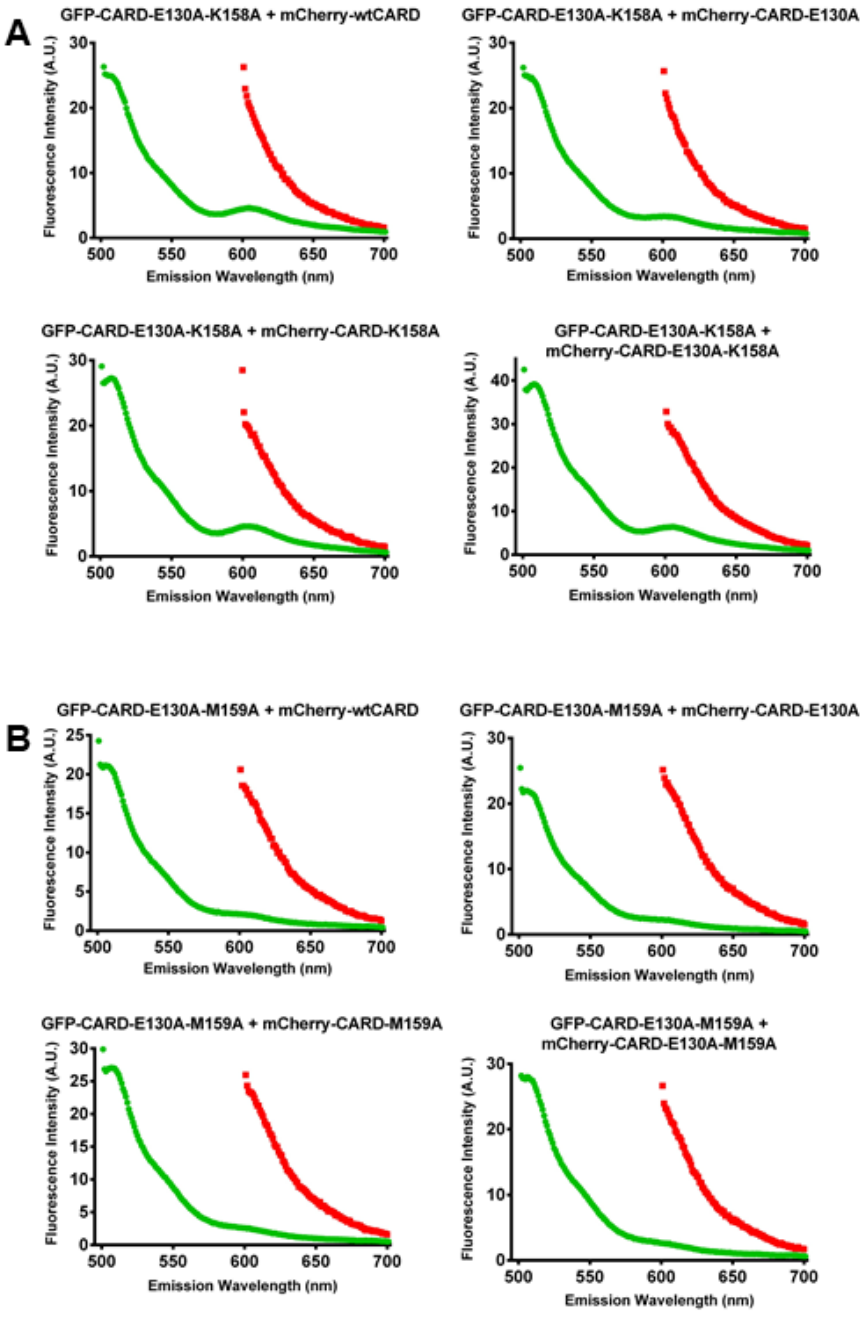

Figure A.12. Emission spectra of CARD (A) E130A-K158A and (B) E130A-M159A variants.

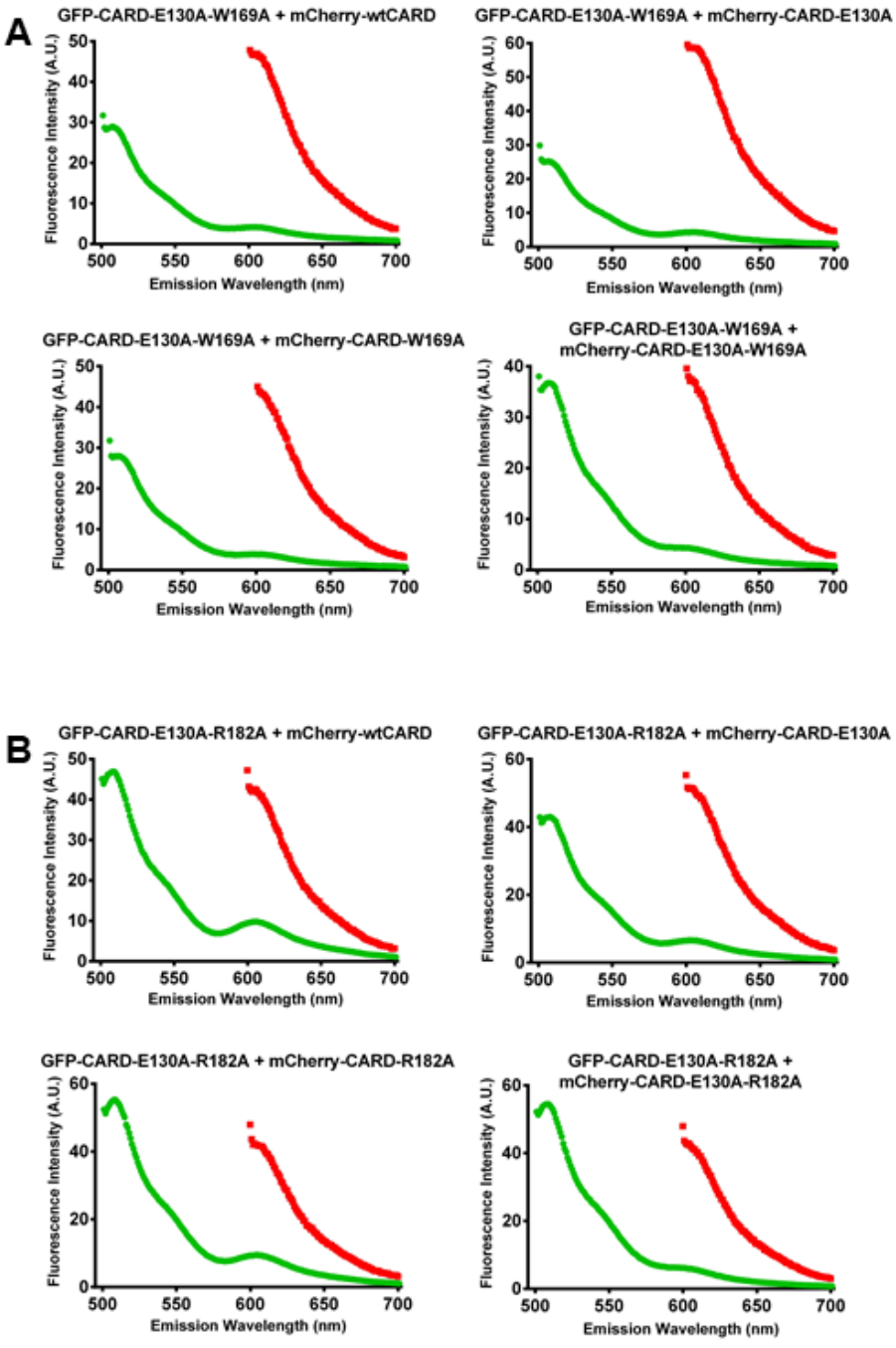

Figure A.13. Emission spectra of CARD (A) E130A-W169A and (B) E130A-R182A variants.

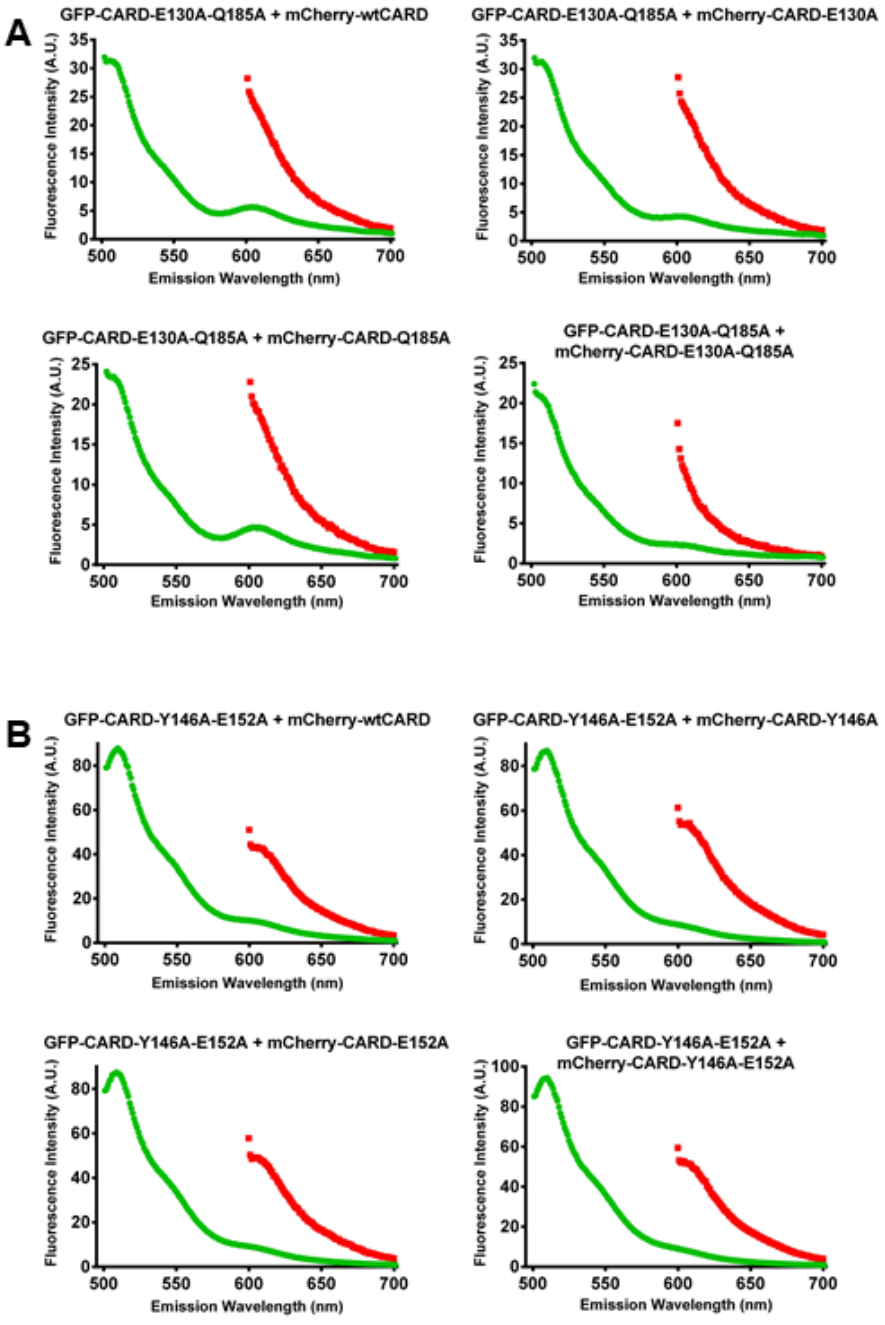

Figure A.14. Emission spectra of CARD (A) E130A-Q185A and (B) Y146A-E152A variants.

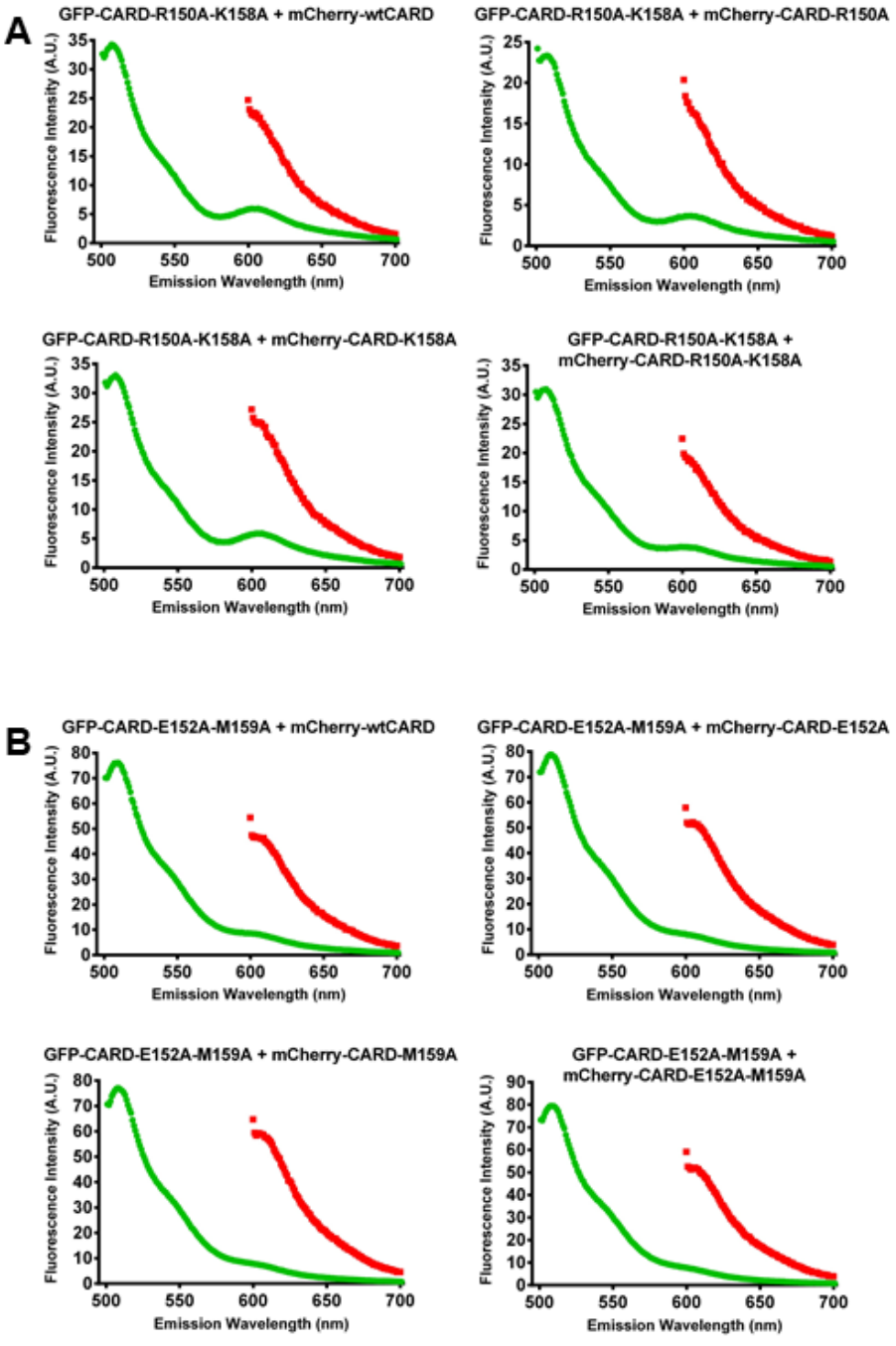

Figure A.15. Emission spectra of CARD (A) R150A-K158A and (B) E152A-M159A variants.

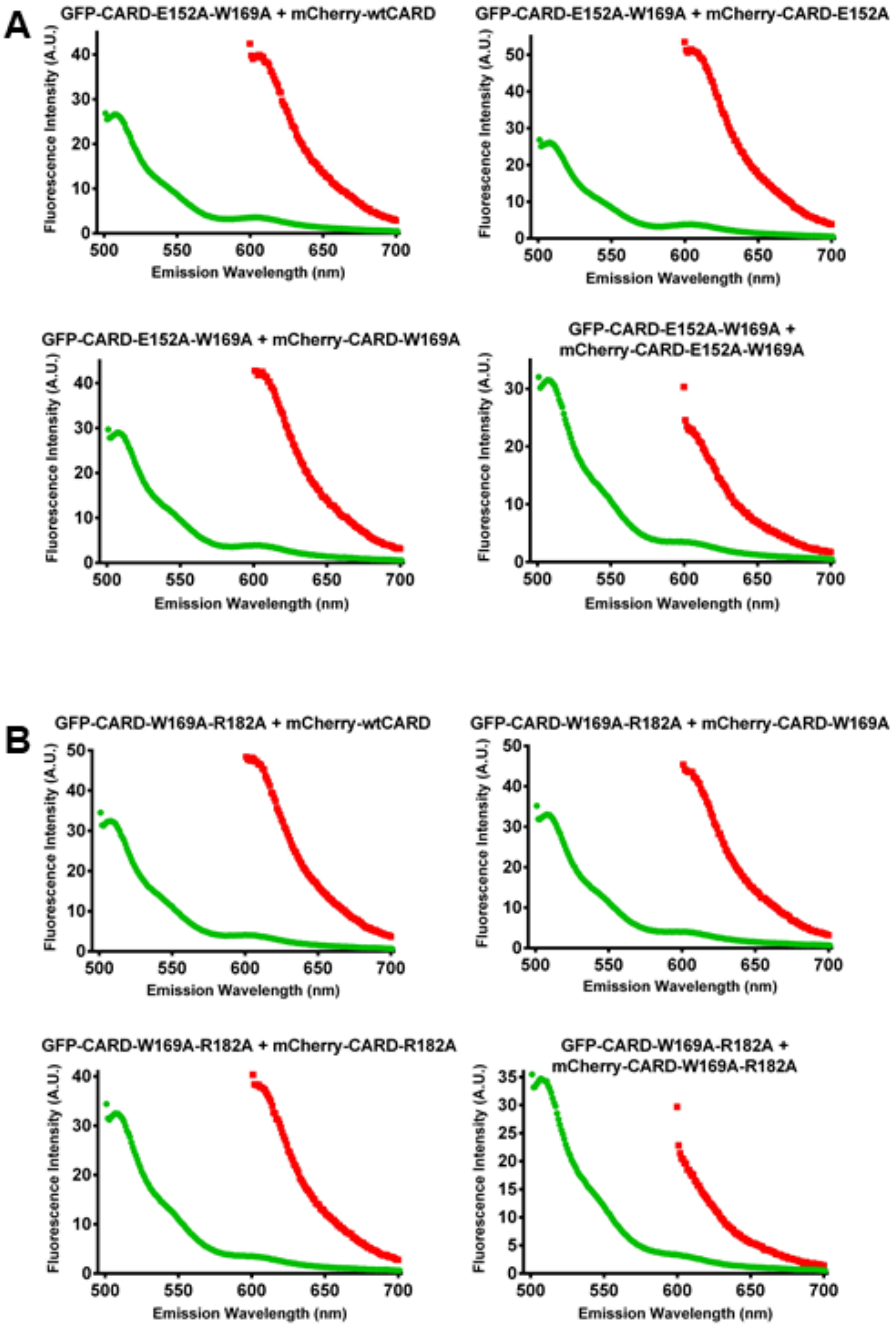

Figure A.16. Emission spectra of CARD (A) E152A-W169A and (B) W169A-R182A variants.

APPENDIX B: PLASMID MAPS

Plasmid maps which were used in this study. A stop codon is present after each PYD and CARD domains.

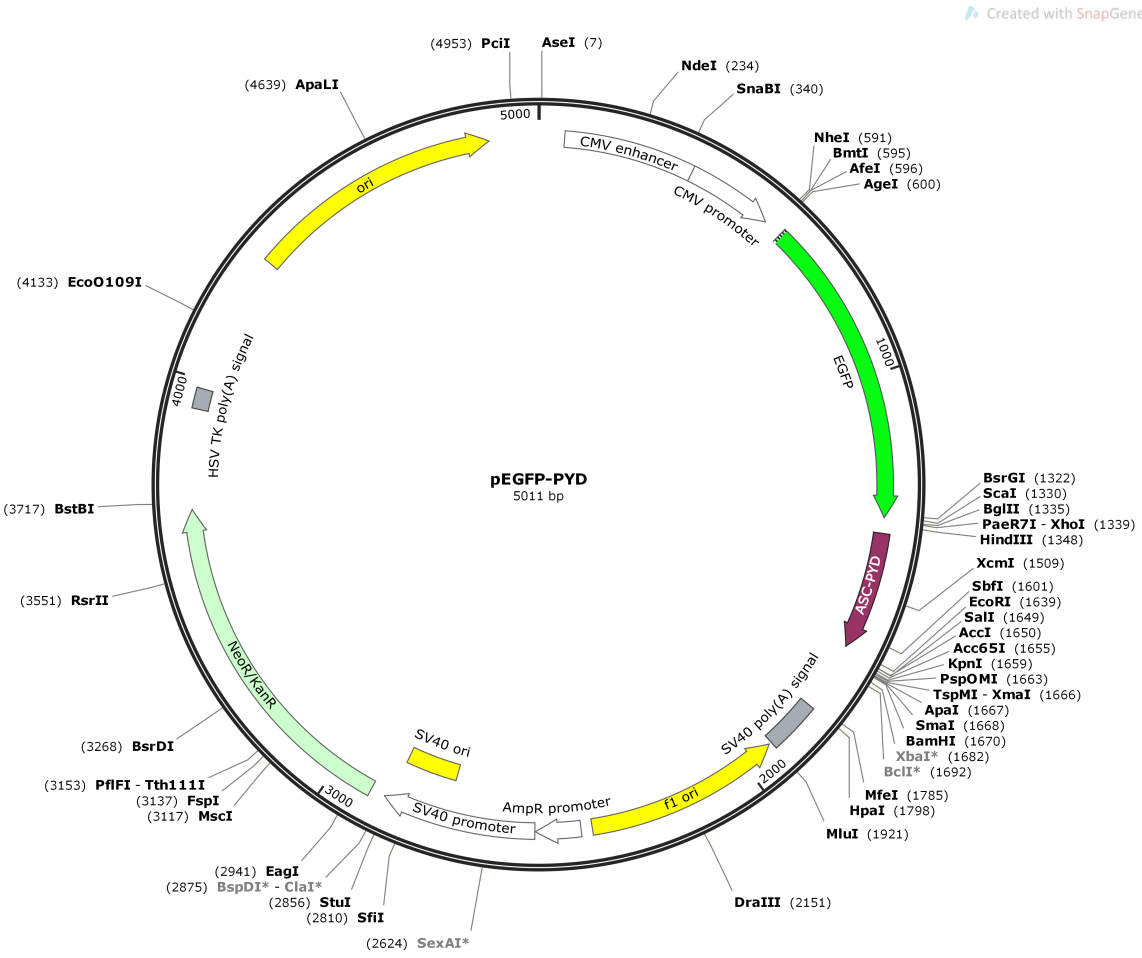

Figure B.1. Plasmid map of pEGFP-C3-PYD.

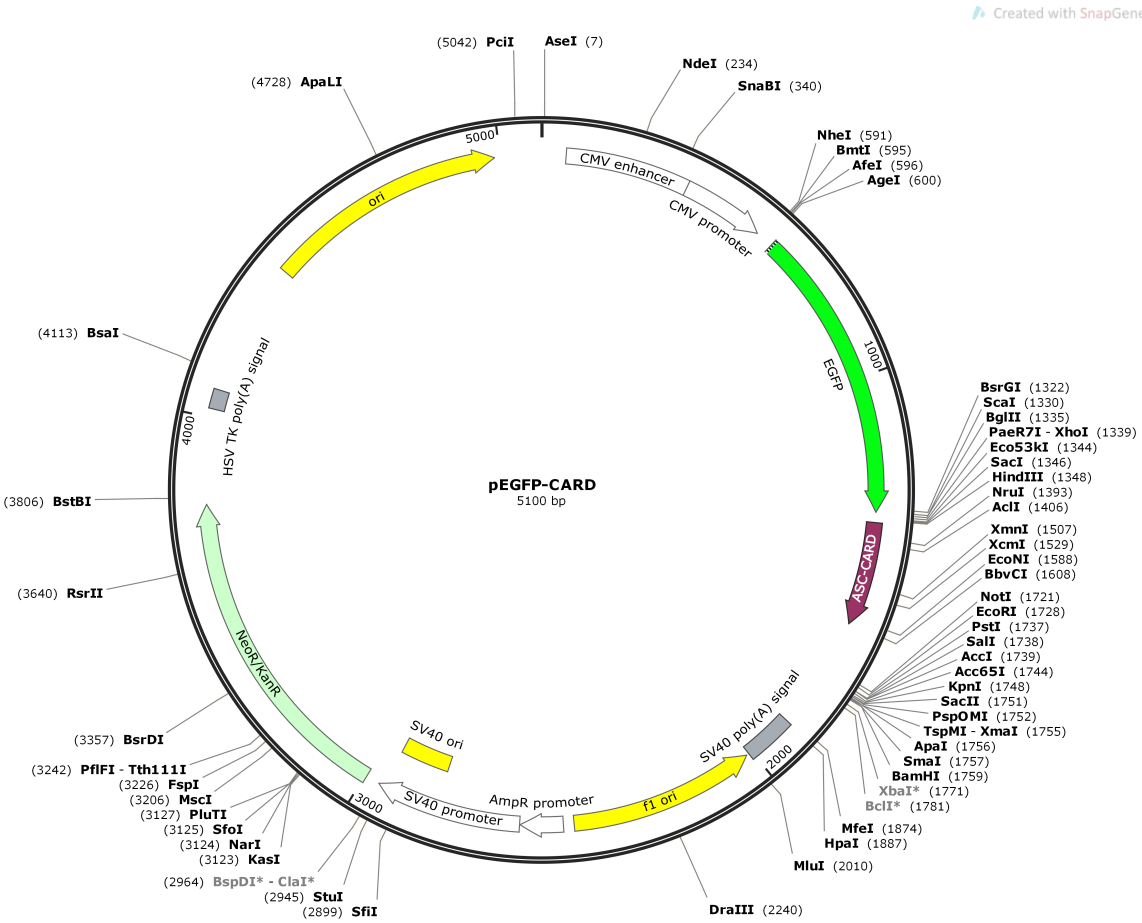

Figure B.2. Plasmid map of pEGFP-C3-CARD.

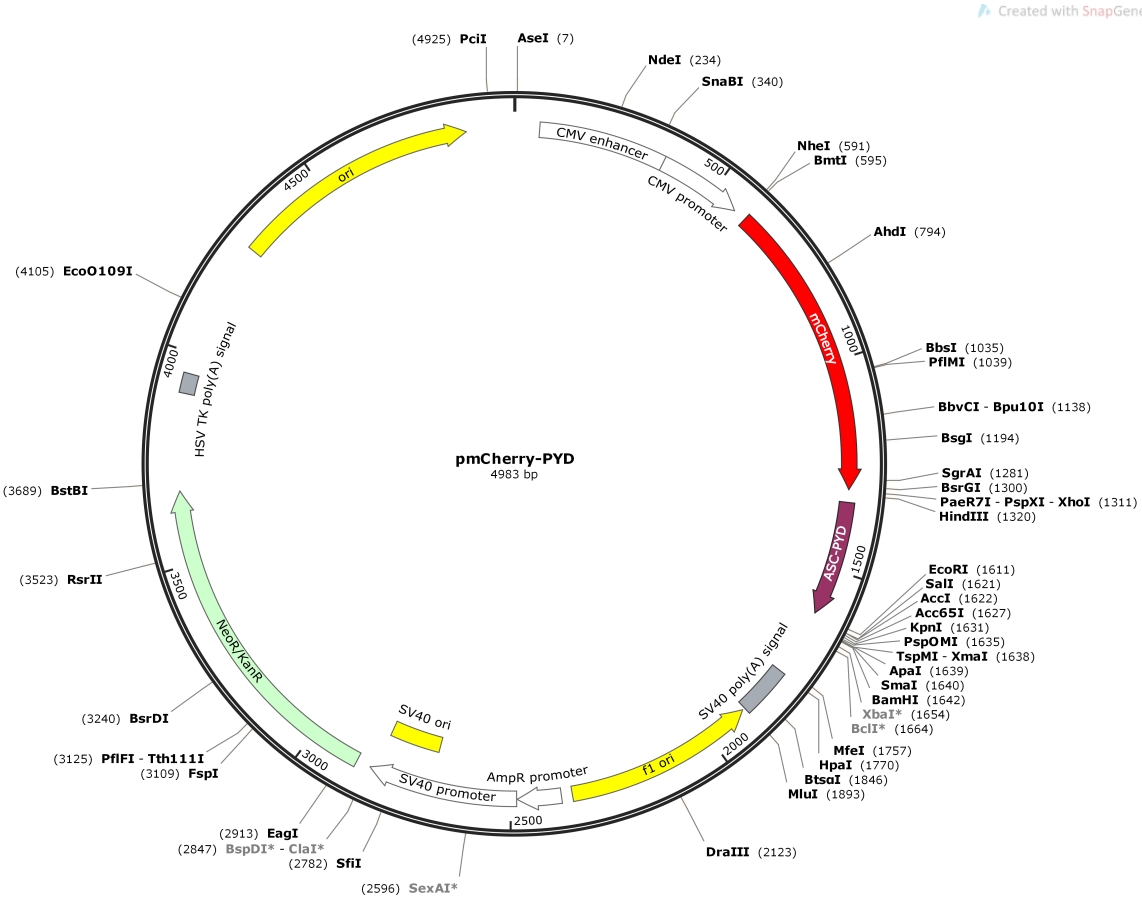

Figure B.3. Plasmid map of pmCherry-C3-PYD.

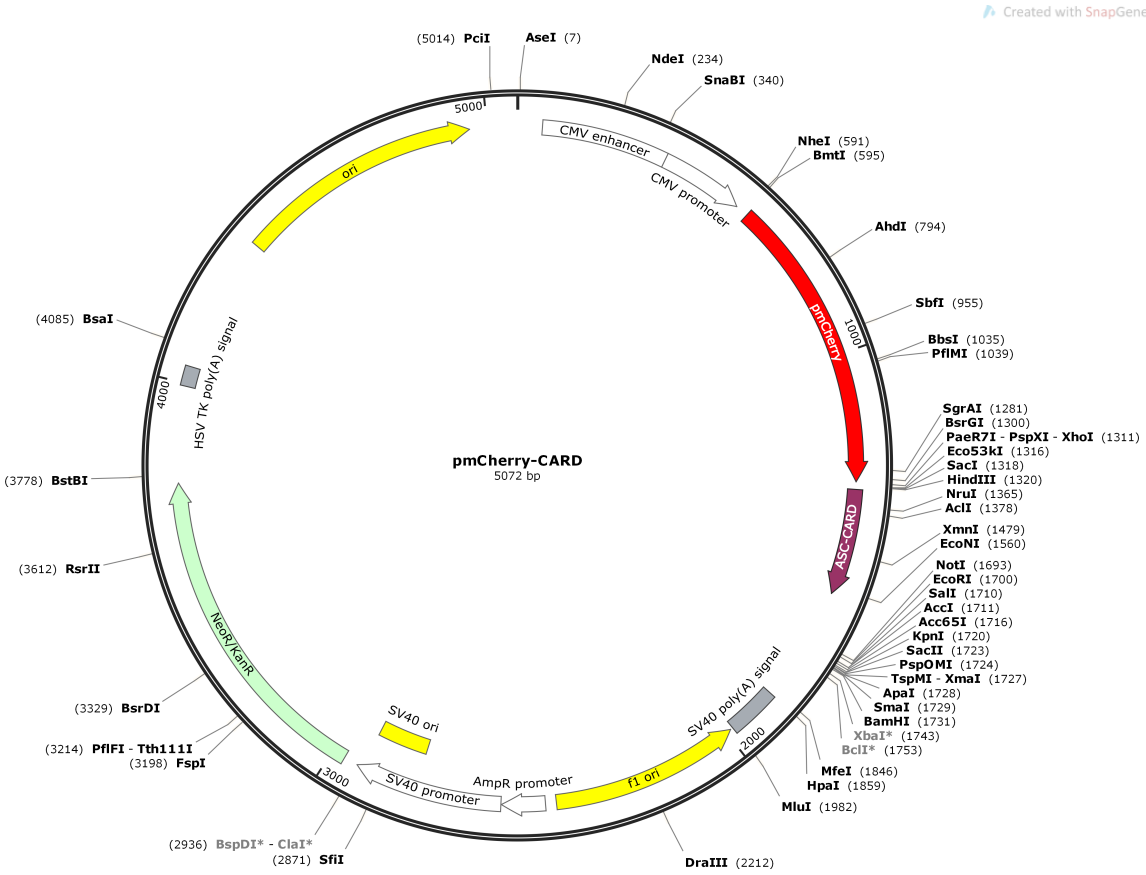

Figure B.4. Plasmid map of pmCherry-C3-CARD.